Hyperfine Effects in Ferromagnet-Semiconductor Heterostructures

A DISSERTATION

SUBMITTED TO THE FACULTY OF THE GRADUATE SCHOOL

OF THE UNIVERSITY OF MINNESOTA

BY

Mun Keat Chan

IN PARTIAL FULFILLMENT OF THE REQUIREMENTS

FOR THE DEGREE OF

Doctor Of Philosophy

April, 2010

Acknowledgements

I would like to thank Paul Crowell who, in 2005, allowed me to join his research group despite my utter lack of knowledge and experience in condensed matter physics. His patience and continued support over the past 5 years, despite a number of barren (data-less) years in the middle, is greatly appreciated. Paul has always been infinitely generous with his time and knowledge.

Joooho Park, despite only about a month of overlap between our respective residence in Paul's lab, was instrumental in getting me started. The high quality of his work and his attention to detail are things I have tried to emulate during my time here (usually without success). Rob Compton introduced me to the time resolved Kerr microscopy setup, and was eminently patient with me in the clean room.

My first project involved measurements of low temperature time resolved spin dynamics of exchange biased Co/FeMn thin films. I worked closely with Jeff Parker, who was then a post-doc, on this project. Despite the occasional casting of aspersions on my machine shop skills and his incomprehensible taste in film. I truly appreciated the great breadth of his knowledge of condensed matter physics and his willingness to share it with me. Prof. Chris Leighton was the PI on the

exchange bias project and his uncanny depth of knowledge on the subject was instrumental in its successful completion.

I was fortunate that when I moved over to working on semiconductors after my 3^{rd} year on the job, Eric Garlid and Jianjie Zhang were willing to help me get started. Eric, being the source of institutional knowledge on the Fe/GaAs systems at the time, was integral in answering the many questions I had. A lot of the credit for the work presented here is due to XiaoHua Lou. He is the one who actually got electrical measurements in Fe/GaAs devices to work. He was also a great source of company during late nights in the lab. Tsuyoshi Kondo, who was a visiting scholar when I first started to work on semiconductors, was instrumental in getting the Janis flow cryostat working for transport measurements.

The many denizens of Paul's lab have provided an intellectually vibrant and continuously entertaining environment in which to work. Particularly, are my fellow graduate students: Teyu Chen and Mike Erickson. I have also had the pleasure to work with a number of extremely talented undergrads: David Toyli, David Christle, and Teresa Brecht.

The most important people to thank here are Qi Hu and Chris Palmstrøm who are responsible for the beautifully grown heterostructures used in this thesis.

Finally, I have to thank my parents and siblings for tolerating my inattentiveness over the past years. Thank you Amy for feeding me while I was writing the thesis.

ABSTRACT

This thesis describes the effect of hyperfine interactions on non-equilibrium electron spins in Fe/GaAs heterostructures. Nuclei in bulk GaAs are dynamically polarized by a non-equilibrium electron spin population injected through an Fe/GaAs Schottky tunnel barrier. The polarized nuclei in turn exert a large hyperfine field upon the electron spins, resulting in rapid electron spin precession. Electrical measurements of the steady state electron spin polarization as a function of applied magnetic field for various injector biases and temperatures allow us to extract the electron spin lifetime, Knight shift, and nuclear field parameters in bulk GaAs. We successfully model electron spin dynamics using a coupled electron-nuclear drift diffusion equation. We confirmed the strong hyperfine coupling between electron and nuclear spins by performing nuclear magnetic resonance measurements on Fe/GaAs devices in applied fields of only a few hundred Oe. Resonant frequencies of different isotopes in the GaAs channel were detected.

In addition to exerting a hyperfine field on the electron spins, we also observe a hyperfine induced spin-dependent Hall effect measured across the spin-polarized region of a GaAs channel. Application of a transverse magnetic field results in a modulation of the Hall voltage consistent with spin de-phasing. This signal changes sign when the magnetization of the Fe contact is switched, indicating sensitivity to electron spin direction. The observed spin-dependent Hall signal is approximately two orders of magnitude larger than that expected from previous

measurements of the spin Hall effect in n-GaAs, which was attributed to spin-orbit coupling and impurity scattering. This suggests that a different mechanism is active in our system. We demonstrate full suppression of the spin-dependent Hall signal by eliminating nuclear polarization through a field cycling procedure. Additionally, while the electron spin accumulation, detected by a spin sensitive Fe contact, persists up to 200 K, the spin-dependent Hall signal is not observed above 120 K, in coincidence with the disappearance of the nuclear spin polarization due to delocalization of donor electrons. We conclude that the observed spin-dependent Hall signal is coupled to the nuclear spin polarization. This is the first observation of a hyperfine-induced spin Hall effect.

Contents

List of Tables

List of Figures

List of Abbreviations

2DEG	Two Dimensional Electron Gas
3T	Three terminal
AHE	Anomalous Hall Effect
AMR	Anisotropic Magneto-resistance
CN	Crank-Nicolson
DNP	Dynamic Nuclear Polarization
DP	D'yakonov-Perel'
EL	Electro-luminescence
ESR	Electron Spin Resonance
F	Ferromagnet
GMR	Giant Magneto-resistance
iSHE	Inverse Spin Hall Effect
N	Normal Metal
NL	Non-local
NLSV	Non-local Spin Valve
NMR	Nuclear Magnetic Resonance
SC	Semiconductor
SDH	Spin Dependent Hall
SHE	Spin Hall Effect
spin-LED	Spin Light Emitting Diode
SQUID	Super-conducting Quantum Interference Device
TMR	Tunneling Magneto-resistance

List of Symbols

$\uparrow (\downarrow)$	Up(down) spin band
α	Current spin polarization
α_0	Current spin polarization at a F/N or F/SC interface
η'	Tunneling spin polarization / Spin injection efficiency / Spin detection sensitivity
γ	Dimensionless parameter of spin-orbit coupling
γ_{sj}	Side-jump dimensionless parameter of spin-orbit coupling
γ_{ss}	Skew scattering dimensionless parameter of spin-orbit coupling
γ_e	Electron gyromagnetic ratio
γ_n	Nuclear gyromagnetic ratio
Γ	Fractional occupation time of an electron on a donor site
λ	Spin diffusion length
$\lambda_{u,d}$	Up and down stream spin diffusion lengths
Λ	Spin orbit coupling parameter
μ	Mobility or chemical potential
μ_B	Bohr magneton
Ω_c	Cell volume
Ω_L	Larmor frequency
ψ	Electron orbital wave function
σ	Charge conductivity
σ_{SH}	Spin Hall conductivity
τ_s	Electron spin lifetime
τ_p	Momentum scattering time
a_0^*	Effective Bohr radius
b_e	Knight field coefficient
b_n	Hyperfine field coefficient
$\mathbf{B}$	Applied magnetic field
$\mathbf{B}_e$	Knight field

B_l	Local field exerted on nuclei
$\mathbf{B}_n$	Hyperfine field
B_R	Re-polarization field
$B_{1(2)}$	Low(High) field sattelite peak position in oblique Hanle geometry
D	Diffusion constant
e	Electron charge
E	Electric field
E_F	Fermi energy
f	Leakage factor or frequency of applid AC field
g_0	Vacuum electron g-factor.
g^*	Effective electron g-factor
$G^{\uparrow(\downarrow)}$	Interface conduction of the up(down) spin band
$\hbar$	Plank's constant
I	Current
$\mathbf{I}$	Nuclear spin
j	Charge current density
k_B	Boltzmann constant
m^*	Effective mass
$M_{i(d)}$	Ferromagnetic injector(detector) magnetization
δn	Non-equilibrium carrier density
n	Density of carriers or doping concentration
$N(E)$	Density of states at energy E
p_i	Polarization density of spins pointing in the i direction
P	Number density spin polarization
P_0	Number density spin polarization at a F/N or F/SC interface
q_{ij}	Spin current density flowing in the i direction of spins in the j direction
$\boldsymbol{R}$	Distance of electron from nuclear center
$\boldsymbol{S}$	Spin
t	Time
T	Temperature
T_f	Non-hyperfine nuclear relaxation time
$T_{measure}$	Measurement time during nuclear elimination procedure
T_{pol}	Nuclear polarization time
T_1	Nuclear relaxation time

v_d	Drift velocity
V	Voltage
V_d	Detector bias voltage signal
V_H	Hall voltage signal
V_{int}	Voltage drop at the Fe/GaAs interface
V_{NL}	NL voltage signal
V_{3T}	3T voltage signal
ΔV_i	Spin dependent voltage in measurement configuration i

Chapter 1

Lateral Fe/GaAs spin Valves

1.1 Spintronics: A Brief History

Spintronics is the study of the spin degree of freedom in solid state devices. This consists of three main areas, namely: (1) the creation of non-equilibrium spin distribution through optical excitation or electrical injection through polarized spin filter materials, (2) the study of transport, dynamics and interactions of spin polarization in the solid state system, and (3) the detection of spin polarization either optically or electrically. A number of important spin effects are already widely implemented in technologically relevant devices, namely giant magneto resistance (GMR)[1] and tunneling magneto resistance (TMR).[2] Such devices, consisting of a thin non-magnetic metallic or insulating layer sandwiched between two ferromagnetic layers, exploit the large change in resistance as a result of differences in reflection and transmission of spin polarized carriers at the interface between magnetic and non-magnetic materials. Such devices are typically not concerned with the manipulation and control of spin polarization in the nonmagnetic layer.

There are various proposals that the ability to manipulate non-equilibrium spin polarization can serve as the basis of a new generation of spintronic devices.[3] The progress towards this end in metals and semiconductors have followed very different historical paths.

Direct band gap semiconductors like GaAs are particularly suitable for optical studies due to the ease of photo-generation of carriers and the subsequent measurement of the emitted luminescence when the carriers recombine. When a circularly polarized photon is absorbed, the angular momentum is distributed between the photo-excited electron and hole according to selection rules determined by the band structure of the semiconductor, thus resulting in a non-equilibrium spin polarization.[14] The spin polarized carriers then decay under various relaxation processes before recombining. The degree of circular polarization of the recombination luminescence is a direct measurement of the carrier spin polarization in the semiconductor. The first experimental demonstration of optical spin orientation of electrons was done by Lampel in 1968 in Si.[4] He measured Nuclear Magnetic Resonance (NMR) due to ^{69}Si nuclei that were polarized through the hyperfine interaction with optically oriented electrons. Optically detected spin orientation was first demonstrated by Parsons in 1969 in GaSb.[5] Extensive work using optical orientation and detection performed at the Ioffe Institute in St. Petersburg and at the Ècole Polytechnique in Paris in the 1970s and 80s have resulted in high precision measurements of band structure parameters, as well as a greater understanding of various spin effects in semiconductors, including electron-nuclear interactions, spin relaxation mechanisms, and spin-orbit interactions. Some of this work is summarized in Ref.[6]. In the 1990s, many of the earlier results in

semiconductors were repeated by David Awschalom's group employing spatial and time-resolved pump-probe techniques. This technique allowed for a direct measure of the spin lifetime as well as the sub-picosecond study of spin dynamics in bulk GaAs.[7, 8] The same technique has also been used to study hyperfine effects and the spin Hall effect in bulk semiconductors.[9, 10]

Normal metals are not amenable to optical orientation of electron spins. An alternative method, electrical injection of spin polarization into a normal metal via a ferromagnet, was first suggested by Aronov in 1976.[11] In 1980, Silsbee proposed electrical detection of spin polarization in metals using a ferromagnetic detector.[12] All-electrical spin injection and detection in a metallic lateral spin valve consisting of 15×40 μm^2 sized NiFe contacts on a cold-rolled Al film was first demonstrated by Johnson and Silsbee in 1985.[13] The spin signal in this experiment was exceedingly small, ~ 10 pV, at low temperatures and was measured using a SQUID pico-voltmeter. In 2001, Jedema *et al.* measured spin signals $\sim 1\mu$V in a NiFe/Co device with sub-micron sized contacts. Since then, there have been numerous experimental reports of metallic lateral spin valves of various materials elucidating the spin injection efficiency, spin relaxation, and the role of the ferromagnet/normal metal interface on the spin signal in such devices.[16–21]

There is increasing interest in performing electrical injection and detection of spin polarization in semiconductors as well. This is partly due to suggestions of technological advantages of spin based transistors in a two-dimensional electron gas (2DEG).[3] 2DEGs are of particular interest due to the ability to control the spin-orbit interaction in the 2DEG with an applied electric field through

the Rashba effect.[25] In 1999, Hammar *et al.* reported on electrical spin injection/detection in an InAs 2DEG with a NiFe contact.[26] The Rashba spin-orbit interaction couples the electron flow in the InAs channel with its spin polarization. Hammar *et al.* observed a jump in the resistance of their InAs channel when the ferromagnetic contact switched directions. They attributed this jump to a change of the direction of injected spin polarization, which results in a change in the electron flow direction through the Rashba effect. This work was met with some skepticism, however.[27] Criticism centered on the extreme sensitivity of the low carrier density 2DEG to the 'local' Hall effect caused by fringe magnetic fields near the ferromagnetic contact.[28] The change in measured resistance could be caused by the change in the fringe field direction when the magnetization of the contact is switched. Unambiguous proof of spin injection can be provided by observation of precessional spin de-phasing in a transverse magnetic field (Hanle Effect) which does not depend on switching the magnetization of the ferromagnetic contact. This was demonstrated in the optical studies in semiconductors [6] as well as in the original and subsequent electrical measurements in metals.[13, 17, 18]

Since 2001 there have been numerous demonstrations of spin injection into semiconductors, particularly GaAs based spin-light-emitting diode (spin-LED) devices. Spin injection is achieved by electrical injection through a ferromagnetic contact and spin polarization is detected by measuring the circular polarization of the recombination electro-luminescence in a quantum well.[29–33] In 2005 Crooker *et al.* successfully imaged transport and precession of spins injected into bulk *n*-GaAs through an Fe contact by using the optical Kerr effect.[37] The first all electrical demonstration of the Hanle effect in semiconductors was reported in

2006 by Lou *et al.*[38] They injected non-equilibrium spin polarization into GaAs by biasing an Fe/GaAs Schottky barrier. The accumulated spin polarization at the Fe/GaAs interface leads to a spin dependent voltage drop that is suppressed by a transverse magnetic field, thus demonstrating spin de-phasing (the Hanle effect). The same group demonstrated all electrical spin injection, transport, precession, and detection on a single device in the non-local geometry in 2007.[39] In this work, spin effects were observed up to temperatures of 70 K. Shortly after, Appelbaum *et al.* demonstrated multiple precession cycles of electrically injected and detected spins in Si.[40] Since then, a number of groups have demonstrated spin injection and detection in GaAs.[41–44] Most recently, Koo *et al.* claimed to have made a spintronic device in a 2DEG in the ballistic regime that uses a gate voltage to manipulate the Rashba coupling. They observed modulation of the detected voltage under changing gate voltage, which they attributed to precession of the spins around the Rashba field. There are however, questions as to the exact interpretation of their data.[23] Also in 2009, Dash *et al.* demonstrated spin injection and detection in both electron and hole doped Si at room temperature.[24]

1.2 Spin Transport

1.2.1 Spin Current

Two fundamental properties are associated with the electron. One is its electric charge. The other is its intrinsic magnetic moment, which is parameterized by the electron spin state. In typical transport measurements of solid state systems,

a voltage is applied to a sample, resulting in charge flow. The rate of charge flow is simply given by

$$\mathbf{j} = \sigma\mathbf{E} + eD\nabla\delta n, \tag{1.1}$$

where $\mathbf{j}$ is the current density, σ is the conductivity, $\mathbf{E}$ is the applied electric field, D is the diffusion constant, and δn is the carrier density deviation from equilibrium. The first term in Eq. 1.1 is simply Ohm's law, which describes charge carriers flowing in an applied field. The second term describes the diffusion of non-equilibrium carriers. This term is typically zero. Note, however, that the population of electrons can be segregated into two spin populations, namely spin up and down. Electric currents are due to carriers within the thermal energy of the Fermi level E_F. σ and D are therefore dependent on the density of states of charge carriers at E_F (N(E_F)). In paramagnetic materials $N^{\uparrow}(E_F) = N^{\downarrow}(E_F)$, therefore $\sigma^{\uparrow} = \sigma^{\downarrow}$ and $D^{\uparrow} = D^{\downarrow}$. In ferromagnets, on the other hand, the Stoner exchange interaction usually results in unequal spin up and down $N(E_F)$ such that $\sigma^{\uparrow} \neq \sigma^{\downarrow}$ and $D^{\uparrow} \neq D^{\downarrow}$. One can write a separate transport equation for each spin channel:[47, 48, 89]

$$\begin{aligned} \mathbf{j}^{\uparrow} &= \sigma^{\uparrow}\mathbf{E} + eD^{\uparrow}\nabla\delta n^{\uparrow}; \\ \mathbf{j}^{\downarrow} &= \sigma^{\downarrow}\mathbf{E} + eD^{\downarrow}\nabla\delta n^{\downarrow}, \end{aligned} \tag{1.2}$$

where $\mathbf{j}^{\uparrow(\downarrow)}$, $\sigma^{\uparrow(\downarrow)}$, $D^{\uparrow(\downarrow)}$, and $\delta n^{\uparrow(\downarrow)}$ are the current density, conductivity, diffusion constant, and carrier density of the up(down) spin channel. In ferromagnets, the current density is spin polarized, i.e. the current consists of a larger proportion of either spin up or down charge carriers.

The continuity equation for the the two spin channels is given by[49]

$$\frac{\partial \delta n^{\uparrow}}{\partial t} = -\frac{\delta n^{\uparrow}}{\tau_{\uparrow\downarrow}} + \frac{\delta n^{\downarrow}}{\tau_{\downarrow\uparrow}} + \frac{1}{e}\nabla \cdot \mathbf{j}^{\uparrow},$$
$$\frac{\partial \delta n^{\downarrow}}{\partial t} = -\frac{\delta n^{\downarrow}}{\tau_{\uparrow\downarrow}} + \frac{\delta n^{\uparrow}}{\tau_{\downarrow\uparrow}} + \frac{1}{e}\nabla \cdot \mathbf{j}^{\downarrow}, \tag{1.3}$$

where $(\tau_{\uparrow\downarrow})^{-1}$ is the scattering rate of up spins into the down spin channel and vice versa for $(\tau_{\downarrow\uparrow})^{-1}$. From Eqs.1.2 and 1.3 and taking the steady state condition $\partial n^{\uparrow}/\partial t = \partial n^{\downarrow}/\partial t = 0$ we obtain

$$\nabla \sigma^{\uparrow} \cdot \mathbf{E} + \sigma^{\uparrow} \nabla \cdot \mathbf{E} + eD^{\uparrow} \nabla^2 \delta n^{\uparrow} = \Big(\frac{\delta n^{\uparrow}}{\tau_{\uparrow\downarrow}} - \frac{\delta n^{\downarrow}}{\tau_{\downarrow\uparrow}}\Big)e, \tag{1.4}$$

$$\nabla \sigma^{\downarrow} \cdot \mathbf{E} + \sigma^{\downarrow} \nabla \cdot \mathbf{E} + eD^{\downarrow} \nabla^2 \delta n^{\uparrow} = \Big(\frac{\delta n^{\downarrow}}{\tau_{\downarrow\uparrow}} - \frac{\delta n^{\uparrow}}{\tau_{\uparrow\downarrow}}\Big)e. \tag{1.5}$$

$$\tag{1.6}$$

By multiplying Eq. 1.4 by $\sigma^{\uparrow}$ and Eq. 1.5 by $\sigma^{\downarrow}$, subtracting the two, and eliminating terms with $\nabla \cdot \mathbf{E}$ we have

$$\nabla^2(\delta n^{\uparrow} - \delta n^{\downarrow}) + \frac{\mu}{eD} e\mathbf{E} \cdot \nabla(\delta n^{\uparrow} - \delta n^{\downarrow}) - \frac{(\delta n^{\uparrow} - \delta n^{\downarrow})}{\lambda} = 0, \tag{1.7}$$

where we have set $\delta n^{\uparrow} + \delta n^{\downarrow} = 0$. Note that in a non-magnetic material, $\delta n^{\uparrow} - \delta n^{\downarrow} = n^{\uparrow} - n^{\downarrow}$ because the equilibrium values of the up and down carrier densities are equal. $\lambda = \sqrt{D\tau_s}$ is the spin diffusion length, with the spin lifetime $(\tau_s)^{-1} = (\tau_{\uparrow\downarrow})^{-1} + (\tau_{\downarrow\uparrow})^{-1}$. μ and D are the effective mobility (we have also used μ to represent the chemical potential, though it should be obvious from the context, which we are referring to) and spin diffusion constant:

$$\mu = \frac{\sigma^{\uparrow}\mu^{\downarrow} + \sigma^{\downarrow}\mu^{\uparrow}}{\sigma^{\uparrow} + \sigma^{\downarrow}}, \tag{1.8}$$

$$D = \frac{\sigma^{\uparrow}D^{\downarrow} + \sigma^{\downarrow}D^{\uparrow}}{\sigma^{\uparrow} + \sigma^{\downarrow}}. \tag{1.9}$$

Assuming charge transport in 1-D (x-direction), the general solution to Eq. 1.7 is

$$\delta n^{\uparrow} - \delta n^{\downarrow} = A_1 e^{-x/\lambda_u} + A_2 e^{-x/\lambda_d}, \tag{1.10}$$

where

$$\lambda_{u,d} = \Big[\pm \frac{\mu|E|}{2D} + \sqrt{\Big(\frac{\mu|E|}{2D}\Big)^2 + \frac{1}{\lambda^2}} \Big]^{-1}. \tag{1.11}$$

$\lambda_{u,d}$ are the spin diffusion lengths for spins diffusing either 'upstream' or 'downstream' with respect to the electric field. Whether or not drift effects are important can be determined by comparing the drift velocity $v_d = \mu E$ to λD, yielding a critical field of

$$E_c = \frac{D}{\lambda \mu}. \tag{1.12}$$

For n-GaAs doped at $n = 10^{16}$ cm^{-3} and a typical $\lambda = 10$ μm, $E_c \sim 1$ V/cm, which is easily achievable. The effective spin diffusion lengths for typical parameters for n-GaAs at $n \sim 10^{16}$ cm^{-3} at low temperatures are shown in Fig. 1.1. In our measurements, we routinely apply electric fields of a few hundred Volts per centimeter, yielding effective spin diffusion lengths of order 100 μm 'downstream'. In a good metal, like Cu, on the other hand, λ is 2-3 orders of magnitude smaller, resulting in $E_C \sim 10^3$ V/cm. This, in addition to the difficulty of establishing a large electric field in a metal means that the drift term can typically be ignored in metals.

1.2.2 Spin Polarization

Spin polarization in a non-magnetic material is commonly defined in two different ways in spin transport experiments. The first is based on the density difference

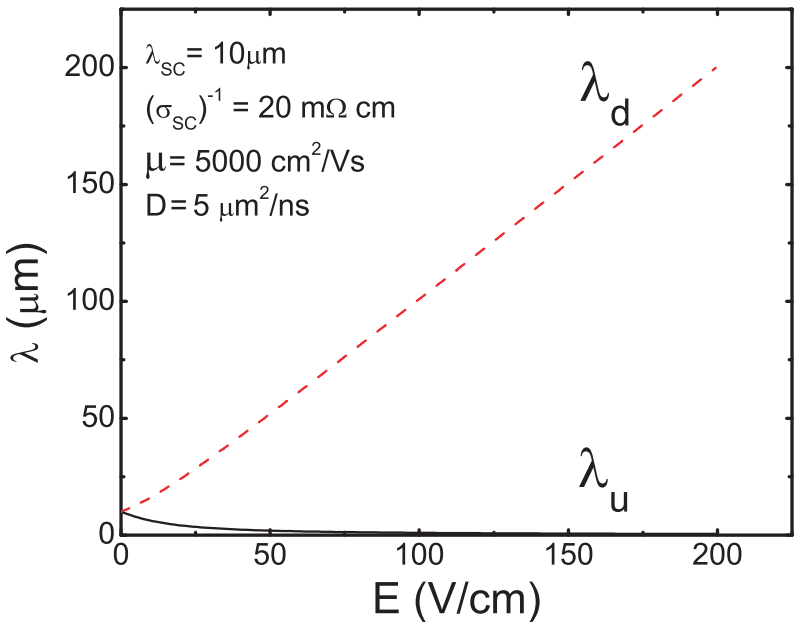

Figure 1.1: Calculated effective spin diffusion lengths for carriers diffusing with (λ_d) and against (λ_u) an applied electric field E in n-GaAs. The parameters are estimated for GaAs with n = 5×10^{16} cm^{-3} at 50 K

.

of up and down carriers:

$$P \equiv \frac{\delta n^{\uparrow} - \delta n^{\downarrow}}{\delta n^{\uparrow} + \delta n^{\downarrow}}. \tag{1.13}$$

Again, in a non-magnetic metal or semiconductor, we can simply equivalently define P in terms of the carrier density,

$$P = \frac{n^{\uparrow} - n^{\downarrow}}{n^{\uparrow} + n^{\downarrow}}. \tag{1.14}$$

The other definition is given by the difference in spin current densities:

$$\alpha \equiv \frac{j^{\uparrow} - j^{\downarrow}}{j^{\uparrow} + j^{\downarrow}}. \tag{1.15}$$

The relationship between the two is given by

$$j^{\uparrow} - j^{\downarrow} = e\left(n^{\uparrow} - n^{\downarrow}\right)\mu E + eD\frac{\partial\left(n^{\uparrow} - n^{\downarrow}\right)}{\partial x}. \tag{1.16}$$

From Eq. 1.10 and the definitions of α, P, and $j = en\mu E$, we get the following relation for electrons diffusing with or against the drift velocity in a non-magnetic material[49]:

$$\alpha = P\Big[1 \pm \frac{D}{E\mu\lambda_{u,d}}\Big]. \tag{1.17}$$

Different types of measurements will be sensitive to either P or α. α is appropriate for measurements of the spin injection or detection efficiency such as TMR or other tunneling spectroscopy experiments.[2, 67] Measurements of spin polarization density such as emission from spin-LED devices would be dependent on P.[29–33]

1.3 Spin Injection

1.3.1 Spin Injection: Ferromagnet/Normal Metal

In this section we will discuss electrical injection of non-equilibrium spin polarization into a non-magnetic material.[35, 36] This is achieved by passing a current from a ferromagnet F into a normal metal N or a semiconductor SC. We will first discuss the simpler example: that of spin injection from F into N through a transparent interface. For a metallic system we can ignore drift effects in Eq. 1.7. Assuming 1-D transport, and casting the continuity equation in terms of chemical potential of up and down spin bands $\mu^{\uparrow(\downarrow)}$ for a degenerate system, where

$$\delta n^{\uparrow(\downarrow)} = eN^{\uparrow(\downarrow)}(E_F)\mu^{\uparrow(\downarrow)}, \tag{1.18}$$

and $N^{\uparrow(\downarrow)}(E_F)$ is the density of states at the Fermi energy of the up(down) spin bands, we have the following equation:

$$\frac{\partial^2(\mu^{\uparrow}-\mu^{\downarrow})}{\partial x^2}=\frac{\mu^{\uparrow}-\mu^{\downarrow}}{\lambda^2}. \tag{1.19}$$

The interface between F and N is located at $x=0$. The general solutions for up and down spin bands in the ferromagnet are

$$\mu_F^{\uparrow}=A-\frac{je}{\sigma_F}x+\frac{B}{\sigma_F^{\uparrow}}e^{(x/\lambda_F)}; \tag{1.20}$$

$$\mu_F^{\downarrow}=A-\frac{je}{\sigma_F}x-\frac{B}{\sigma_F^{\downarrow}}e^{(x/\lambda_F)}, \tag{1.21}$$

where $\sigma_F=\sigma_F^{\uparrow}+\sigma_F^{\downarrow}$ is the electrical conductivity in F and λ_F is the spin diffusion length in F. We have also introduced the current polarization

$$\alpha_F\equiv\frac{\left(\sigma_F^{\uparrow}-\sigma_F^{\downarrow}\right)}{\left(\sigma_F^{\uparrow}+\sigma_F^{\downarrow}\right)}. \tag{1.22}$$

Likewise in the N region:

$$\mu_N^{\uparrow}=-\frac{jex}{\sigma_N}+\frac{2C}{\sigma_N}e^{-x/\lambda_N}; \tag{1.23}$$

$$\mu_N^{\downarrow}=-\frac{jex}{\sigma_N}-\frac{2C}{\sigma_N}e^{-x/\lambda_N}, \tag{1.24}$$

where λ_N is the spin diffusion length in N. The current density of each spin channel is determined from the chemical potentials by

$$j^{\uparrow(\downarrow)}=-\frac{\sigma^{\uparrow(\downarrow)}}{e}\frac{\partial\mu^{\uparrow(\downarrow)}}{\partial x}. \tag{1.25}$$

By implementing Eqs.1.20-1.25, with the interface at ($x = 0$), and boundary conditions

$$\mu_F^{\uparrow} = \mu_N^{\uparrow} \mid_{x=0}, \tag{1.26}$$

$$\mu_F^{\downarrow} = \mu_N^{\downarrow} \mid_{x=0}, \tag{1.27}$$

$$j_F^{\uparrow} = j_N^{\uparrow} \mid_{x=0}, \tag{1.28}$$

we obtain $\mu^{\uparrow}$ and $\mu^{\downarrow}$ for a F/N system shown in Fig. 1.2(a). At the F/N interface, $\mu^{\uparrow}$ and $\mu^{\downarrow}$ are split. The splitting decreases further away from the interface. Far away from the F/N interface, $\mu^{\uparrow} = \mu^{\downarrow}$ and their slopes are determined by $je/\sigma_{F,N}$ for F and N respectively. The non-equilibrium spin polarization P is therefore large at $x = 0$ and decays exponentially with characteristic length scale $\lambda_{F,N}$. Likewise, the current polarization is equal to α_F in F and $\alpha_N = 0$ in N far from the interface and the transition between these two values occurs on the length scale of the spin diffusion lengths $\lambda_{F,N}$.

We obtain the following expression for the injected non-equilibrium current polarization at the interface:

$$\alpha_0 = \frac{1}{1 + (1 - \alpha_F^2)\frac{\sigma_F \lambda_N}{\sigma_N \lambda_F}} \alpha_F. \tag{1.29}$$

If we define the spin resistivity (which has units of a resistance area product: Ωm^2) as the product of electric resistivity and spin diffusion length, $R_i^S = \lambda_i/\sigma_i$, where $i = F, N$, we have

$$\alpha_0 = \frac{1}{1 + (1 - \alpha_F^2)\frac{R_N^S}{R_F^S}} \alpha_F. \tag{1.30}$$

We can now clearly see that the efficiency of spin injection for a transparent F/N interface is governed by α_F and the ratio of N to F spin resistivities. α_0 is suppressed if $R_N^S \gg R_F^S$. This phenomena is known as the 'resistivity mismatch', and

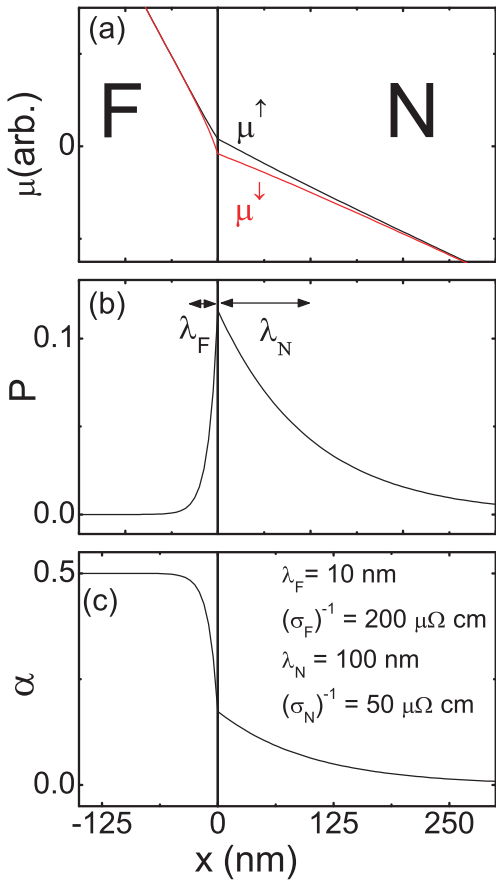

Figure 1.2: Spin injection from a ferromagnet F into a normal metal N for the case $\alpha_F = 0.5$. The calculated chemical potential μ (a) non-equilibrium spin polarization P (b) and current polarization α (c) as a function of position x, where the F/N interface is located at $x = 0$.

was originally presented by Johnson and Silsbee.[63] This is actually a misnomer in a sense, since the important figure of merit is not the resistivity, but the *spin* resistance. Spins that are injected into N by a current can either diffuse into N or back into F. If $R_F \gg R_N$, carriers will be prevented from back diffusing, thus increasing spin injection efficiency. On the other hand, if λ_F is small, R_F^S is small, and F can be viewed as an effective spin sink, thus reducing spin injection efficiency. This problem is compounded in ferromagnet/semiconductor (F/SC) systems where the resistivity of a semiconductor can be 2 to 3 orders of magnitude larger ($\sim$ 10 mΩcm for n-GaAs, $n \sim 10^{16}$cm^{-3}) than for a typical normal metal. The SC spin diffusion length can also be an order of magnitude larger ($\sim$ 10 μm for n-GaAs) than for N. The combination leads to a SC spin resistivity R_{SC}^S that is 3-4 orders of magnitude larger than R_F^S of a typical F, and an exceedingly small spin injection efficiency. It is generally believed that electrical spin injection into SCs through a transparent interface is not possible.[53, 63]

The 'resistivity mismatch' problem can be overcome by increasing the interface resistance (by introducing a tunnel barrier, for example) to prevent spins from diffusing back into F. The increase in spin injection efficiency through this means has been achieved in numerous metallic devices.[16–18]

1.3.2 Spin Injection: Ferromagnet/Semiconductor

In order to calculate spin injection from F into a semiconductor SC, we have to include the drift terms in Eq. 1.7. Additionally, we will not assume a transparent interface, but instead introduce interfacial conductances for the spin up and down channels $G^{\uparrow}$ and $G^{\downarrow}$. Using a similar method to that described in Sec.1.3.1 with

new boundary conditions at the F/SC interface

$$\begin{aligned} j_{SC}^{\uparrow} &= G^{\uparrow}(\mu_F^{\uparrow} - \mu_{SC}^{\uparrow}) \mid_{x=0}, \\ j_{SC}^{\downarrow} &= G^{\downarrow}(\mu_F^{\downarrow} - \mu_{SC}^{\downarrow}) \mid_{x=0}, \\ j_F^{\uparrow} - j_F^{\downarrow} &= j_{SC}^{\uparrow} - j_{SC}^{\downarrow} \mid_{x=0}, \end{aligned} \tag{1.31}$$

Yu and Flatté [49] calculated the spin polarization in the limit of small deviation from equilibrium, $\delta n^{\uparrow,\downarrow} \ll n$;

$$\alpha_0 = \frac{R_F + R_-}{R_F + R_{SC} + R_+}, \tag{1.32}$$

where

$$\begin{aligned} R_F &\equiv \frac{\alpha_F \lambda_F}{(1-\alpha_F^2)\sigma_F}; \\ R_{SC} &\equiv \frac{\lambda_{SC,u(d)}}{\sigma_{SC}}; \\ R_+ &\equiv \frac{1}{G^{\uparrow}} + \frac{1}{G^{\downarrow}}; \\ R_- &\equiv \frac{1}{G^{\uparrow}} - \frac{1}{G^{\downarrow}}, \end{aligned} \tag{1.33}$$

σ_{SC} is the conductivity in the SC, and $\lambda_{SC,u(d)}$ is the upstream or downstream spin diffusion length in the SC. For carriers flowing from F into SC, the interface is located upstream from the SC, so one should use $\lambda_{SC,u}$. Likewise for carriers flowing from SC to F and $\lambda_{SC,d}$.

A Schottky tunnel barrier forms naturally at the interface between a ferromagnetic metal and a semiconductor. The width of the Schottky tunnel barrier in our devices is tuned, to enhance spin injection efficiency. The possibility of using an interfacial barrier with $G^{\uparrow} \neq G^{\downarrow}$ to enhance spin injection was discussed

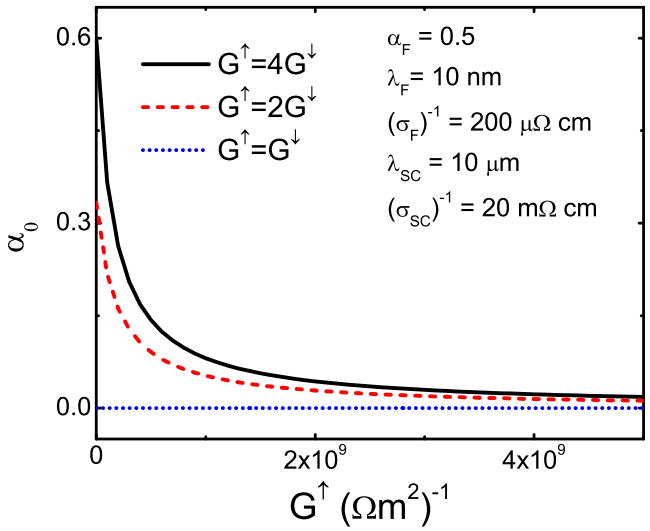

Figure 1.3: Current polarization of injected spin at a ferromagnet-semiconductor F/SC interface as a function of interfacial conductance G for different degrees of interfacial spin selectivity

in Refs. [54–56]. Fig. 1.3 shows that increasing the ratio between $G^{\uparrow}$ and $G^{\downarrow}$ increases α_0. Additionally when the total interfacial conductance is increased, α_0 is suppressed due the 'conductance mismatch' problem.

The spin injection coefficient, Eq. 1.32, is also indirectly dependent on the electric field in the SC. Fig. 1.4 shows the calculated α_0 as a function of E. For positive E, α_0 is enhanced. This is because under reverse bias, the electron drift sweeps spins away from the F/SC interface, thus decreasing the spin resistance in the SC. When the direction of charge flow is reversed spin are pushed against the F/SC interface, thus preventing effective spin injection and α_0 is suppressed. Note that these drift effects on the spin injection efficiency become irrelevant if the interfacial resistance area product R_+ is much larger than the spin resistance

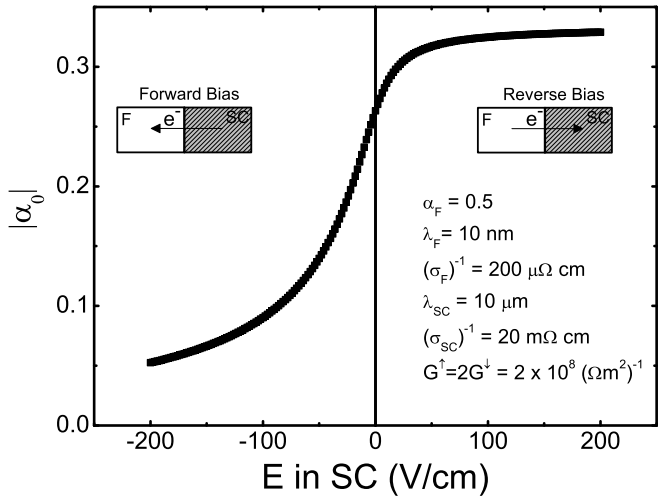

Figure 1.4: Calculated current polarization of injected spins α at the ferromagnet-semiconductor F/SC interface as a function of applied electric field in SC. $E < 0$ corresponds to carriers flowing from SC into F, and $E > 0$ when carriers flow from F into SC.

in SC R_{SC}.

In determining the electric field dependence of α_0 in Fig. 1.4 we have assumed that $G^{\uparrow}$ and $G^{\downarrow}$ are independent of the interface voltage. Transport through real Schottky tunnel barriers typically involve three different processes: diffusion, thermionic emission and tunneling. Diffusion and thermionic emission are characterized by $j \propto \left(e^{eV/k_BT} - 1\right)$. The presence of these effects results in rectifying behavior, as shown by the interface IV curve for a Fe/GaAs device in Fig. 1.5(a). The expected α_0 for this device is shown in Fig. 1.5(c) based on the interface conductance values in Fig. 1.5(b). Note that the applied electric fields in our devices are much less than the maximum values shown in Fig. 1.4. As a result the E dependence of α_0 is rather weak, $\approx 15\%$ suppression under reverse bias.

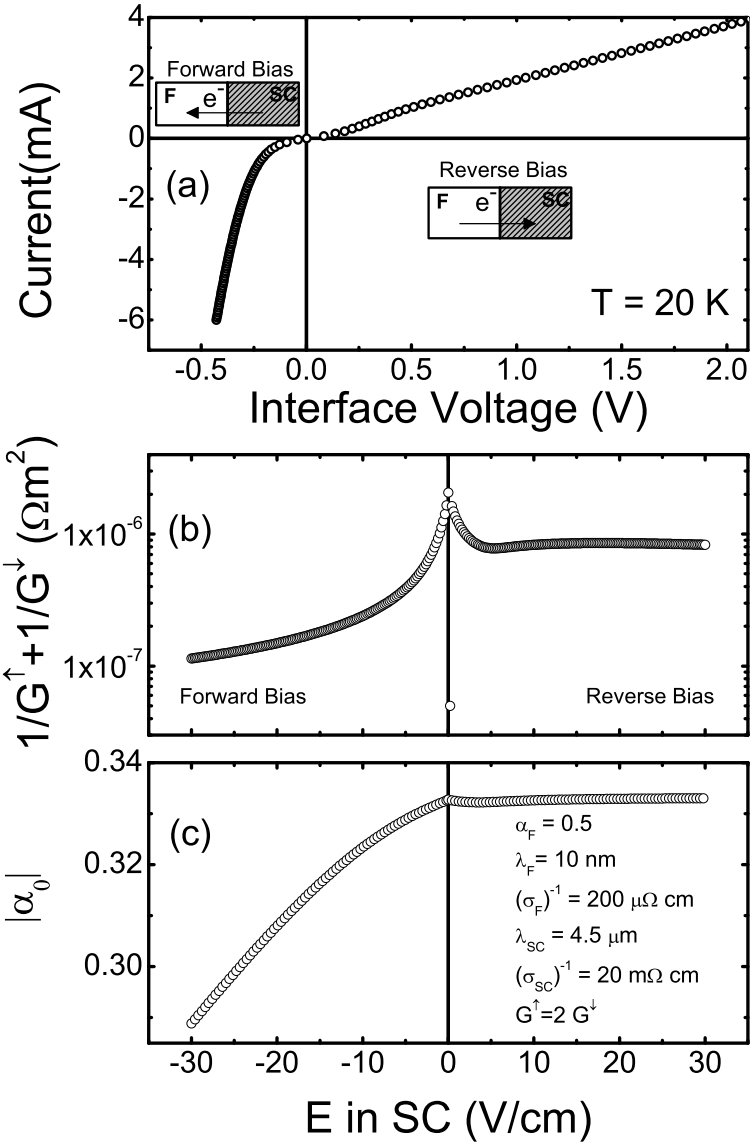

Figure 1.5: (Sample Q62)(a) Measured interface IV curve for an Fe/GaAs device with contact area 5×50 μm^2. (b) Interface resistivity as a function of the electric field in the bulk GaAs channel. (c) Polarization at the Fe/GaAs interface determined from the measured interface conductance using Eq. 1.32 by assuming $G^{\uparrow} = 2G^{\downarrow}$.

We have assumed that the relative values of $G^{\uparrow}$ and $G^{\downarrow}$ are constant as a function of interface bias. The tunneling current density depends on the density of states on either side of the barrier[57, 58]:

$$j^{\uparrow,\downarrow} = \frac{4\pi e}{\hbar} \sum_{k_x} \int_{\infty}^{\infty} dE \Big[N_i^{\uparrow,\downarrow}(E) f(E) \Big] P^{\uparrow,\downarrow}(E) \Big[N_j^{\uparrow,\downarrow}(E - eV) \Big(1 - f(E - eV) \Big) \Big], \tag{1.34}$$

where carriers are tunneling from i to j. $N(E)$ is the density of states, $f(E)$ is the Fermi-Dirac distribution, and $P(E)$ is the barrier dependent tunneling probability. The sum is taken over all the transverse momentum k_x states. The polarization of the injected current density is explicitly dependent on the relative up and down Fe densities of states available to tunneling, which can change with the applied voltage.

Since 2001, there have been numerous experimental demonstrations of spin injection into GaAs based spin-LED devices, where the degree of injected spin polarization is determined by the circular polarization of the electro-luminescence (EL) emitted from recombination of carriers in a quantum well.[29–33] The injected spin polarization is typically $\sim 20\%$ at low temperatures. Most of these devices used a native Schottky barrier between the ferromagnet and semiconductor as the tunnel barrier. The depletion depth of a Schottky tunnel barrier d is given by

$$d = \sqrt{\frac{\varepsilon \phi_B}{2\pi n e}} \tag{1.35}$$

where ϕ_B is the barrier height and n is the doping level of the semiconductor at the interface. In order to achieve high spin injection efficiency, it was found that $n \sim 10^{18} - 10^{19}$ cm^{-3} in n-GaAs to ensure a sufficiently thin Schottky barrier. On the other hand, as shown in Fig. 1.6, the spin lifetime in n-GaAs is known

to be large in a small doping window around 10^{16} cm^{-3}, falling off precipitously for higher doping. High injection efficiency has to be balanced by the competing interest of having a large spin lifetime. This is resolved by injecting spins into bulk $n \sim 10^{16}$ cm^{-3} n-GaAs through a thin highly doped layer $n \sim 10^{18}$ cm^{-3} at the interface with the ferromagnet. We can therefore ensure a thin Schottky barrier, while maintaining large spin lifetimes in the bulk.

1.3.3 Relating α_0 to P_0

We have thus far discussed the current spin polarization at a F/SC interface α_0. Its relationship to the spin polarization density P_0 is not trivial. From Eq. 1.17 and the effective spin diffusion lengths under the influence of an electric field given by Eq. 1.11, we can relate the interfacial current and density spin polarizations by

$$\alpha_0 = P_0 \frac{D}{E\mu\lambda_u} \text{ Spin Injection (Reverse Bias),} \tag{1.36}$$

$$\alpha_0 = -P_0 \frac{D}{E\mu\lambda_d} \text{ Spin Extraction (Forward Bias).} \tag{1.37}$$

Fig. 1.7 shows P_0 as a function of the electric field in SC for a fixed α_0.[49, 64, 65] At $E = 0$, $P_0 = 0$ due to the absence of flowing current. When an electric field is applied, non-equilibrium spin polarization accumulates near the interface. The accumulation layer is either expanded or shrunk, depending on the direction of E. Under reverse bias, electrons tunnel into GaAs from the Fe contact, and the accumulation layer is extended as drift and diffusion transport electrons into the bulk of the GaAs channel. As E is increased P_0 increases as more polarized electrons are injected. However, the accumulation layer is expanded when E

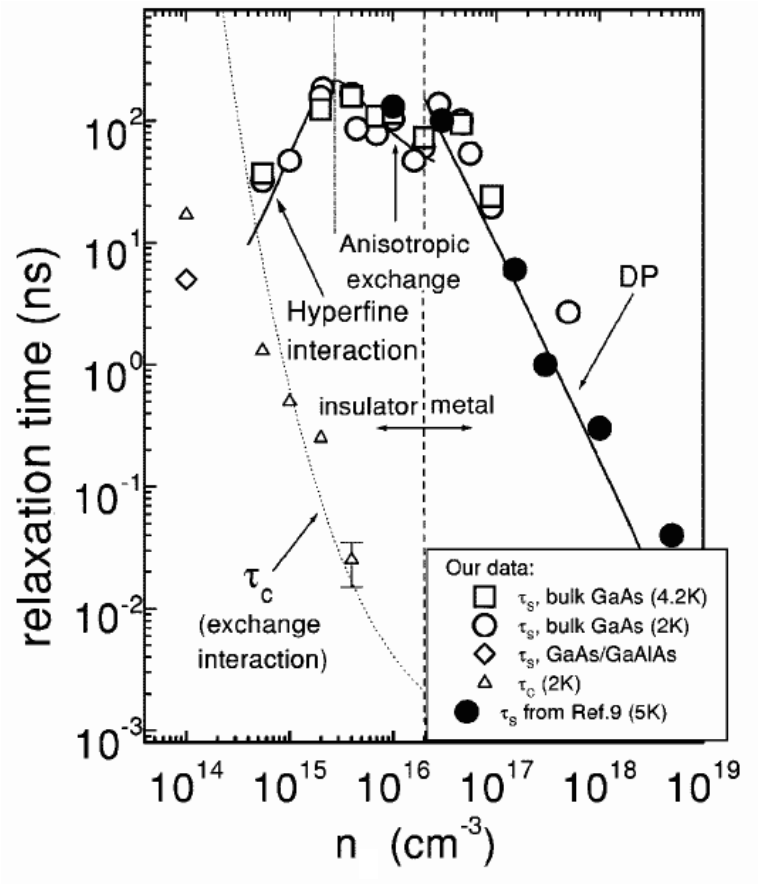

Figure 1.6: Spin relaxation time τ_s as a function of donor concentration n in n-GaAs.[59]

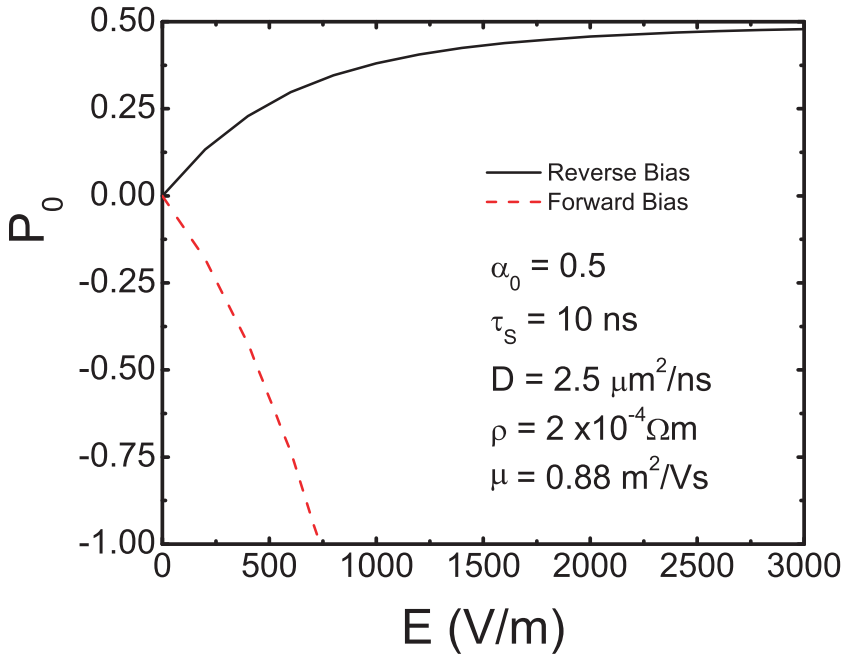

Figure 1.7: Calculated P_0 under forward and reverse biased F/SC interface using Eq. 1.37 with $\alpha_0 = 0.5$.

increases, thus balancing the rise in the total number of injected spins. The actual density of spin polarized electrons P_0 therefore saturates to α_0 for large E under reverse bias.

Under forward bias, on the other hand, electrons are pushed towards the Fe/GaAs interface, counter to the direction of spin diffusion. If α_0 is positive, as it is in Fig. 1.7, spin up electrons are preferentially extracted, resulting in an accumulation of spin down electrons at the F/SC interface. P_0 is therefore negative. Unlike the case of reverse bias, under forward bias, the shrinking of the spin accumulation layer with increasing electric field means that the thickness of the accumulation layer of polarized electrons decreases with increasing E. The magnitude of density spin polarization at the Fe/GaAs interface P_0, for a fixed

current spin polarization α_0 will therefore increase without bound, as shown in Fig. 1.7. In the case of a real tunnel barrier however, $\alpha_0 = (j^{\uparrow} - j^{\downarrow})/(j^{\uparrow} + j^{\downarrow})$ is not expected to remain constant as P_0 increases. The spin up and down current density flowing from Fe into GaAs $j^{\uparrow,\downarrow}$ as shown in Eq. 1.34, is dependent on the number of available electrons $n^{\uparrow,\downarrow}$ in the GaAs to tunnel from. As P_0 approaches -1, $n^{\uparrow}$ drops, thus decreasing extraction current polarization α_0, and tending to saturate P_0. Osipov *et al.*[64] calculated, for a Fe/GaAs interface with degenerate n-GaAs and assuming a thin triangular Schottky barrier that for the limit of large current densities, $P_0 = \alpha_0$ under reverse bias (in agreement with Fig. 1.7), while under forward bias, P_0 is limited to $P_0 = -0.6P_F$.

1.4 Experimental Details

1.4.1 Sample Growth and Fabrication

Details of a typical Fe/GaAs structure can be found in Fig. 1.8. The structure is grown using molecular beam epitaxy on semi-insulating GaAs (100) wafers. It consists of 2.5 μm of n-doped GaAs (Si donor concentration $n \sim 5 \times 10^{16}$ cm^{-3}), followed by a 15 nm transition region where n is increased to 5×10^{18} cm^{-3} and then kept at $n = 5 \times 10^{18}$ cm^{-3} for another 15 nm. An epitaxial Fe layer is then deposited, which is capped by Al and Au. The epitaxial Fe layer has crystalline anisotropy such that it has easy [110] and hard [1$\bar{1}$0] ($\sim$ 1.5 kOe saturation field) in plane axes. The out of plane axis [100] has a saturation field of about 2.1 T.

A particular heterostructure is typically grown on a $\approx 5 \times 10$ cm^2 piece of substrate, after which it is cleaved into 4×4 mm^2 chips. Each chip is fabricated

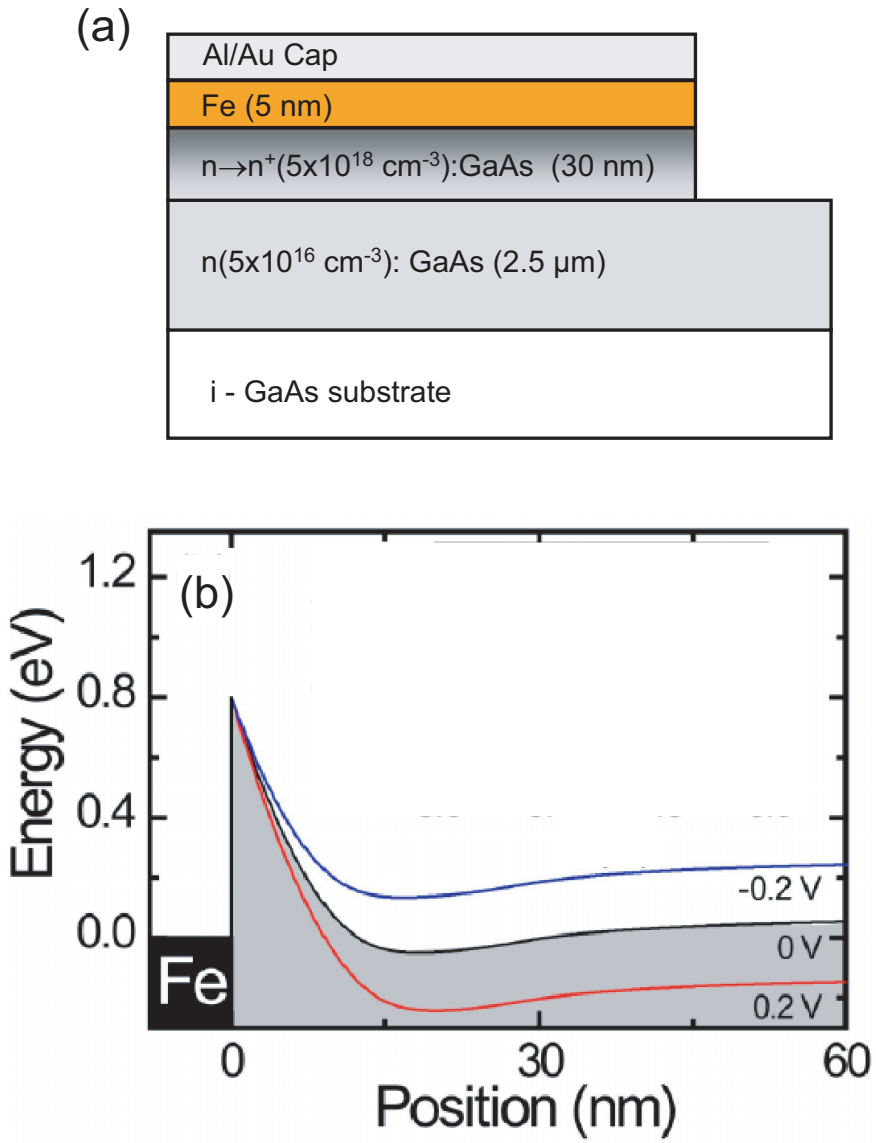

Figure 1.8: (a) Fe/GaAs heterostructures used in our experiments. (b) Conduction band structure near the Fe/GaAs interface under zero bias, forward bias (-0.2 V) and reverse bias (+0.2 V). Figure is from Ref. [38].

individually. The samples used in this thesis are labeled as: grower initial, series number - sample number. For example, Q62-1 is the 62^{nd} heterostructure grown by Qi Hu, and the first device made from that particular growth. Therefore, all samples labeled Q62 are derived from the same heterostructure.

The fabrication of samples consists of multiple steps. Each step involves photolithography to define relevant features followed by either etching or deposition to subtract from or add to the sample. The fabrication procedure is schematically shown in Fig. 1.10 and proceeds through the following general steps:

I. Define Fe contacts: Ion mill to etch away the cap, Fe, and highly doped layers everywhere except where the Fe contacts will be. We remove the highly doped layer in order to ensure that spin transport occurs in the bulk of the sample. Fe injector and detector contacts are typically $\sim 5 \times 50$ μm^2.

II. Define channel and other GaAs features: The GaAs channel is typically 50 μm wide and hundreds of μm long. The channel is wet etched using a dilute hydrogen peroxide:ammonium hydroxide:water mixture. Wet etching etches laterally as well as vertically, so any defined features will end up smaller due to lateral etching. This has to be accounted for when fabricating features of lateral size comparable to the thickness of the GaAs layer (2.5μm).

III. Define SiN insulator: The Fe contacts are typically too small to be contacted to directly. Au leads are therefore used to connect them to large contact pads. A SiN insulating layer is deposited in order

to prevent the Au leads from shorting to the GaAs channel or other features. This is deposited using Plasma Enhanced Chemical Vapor Deposition (PECVD).

IV. Define leads and pads: Ti/Au leads and pads are deposited in order to provide electrical access to the Fe contacts. Ti acts as a wetting layer and prevents the Au leads from peeling off.

We typically fabricate 4 devices on a single chip. The finished samples are mounted on a Quantum Design rotator board and the pads are wire bonded.

1.4.2 Measurements

Measurements were performed in a Janis ^{4}He low temperature flow cryostat. The transport measurements we perform are extremely sensitive to fluctuations of temperature. We therefore need temperature stability of < 5 mK for time frames of at least several hours (especially for the steady state measurements of hyperfine effects, which require a few hours for a single field sweep). To this end, we have added a sample stage that is thermally weakly linked to the cold-finger. Both the sample stage and cold-finger are fitted with heaters and Cernox thermometers. The temperature at the cold-finger and sample stage are separately controlled. Measurements are performed between 10 K and 300 K. Above 150 K the temperature stability is only ~ 10 mK; however, we find that the measurements are also less sensitive to fluctuations at high temperatures.

Magnetic field is applied using a small electro-magnet with a bipolar amplifier power supply. The maximum DC field obtained is approximately 2 kOe. The

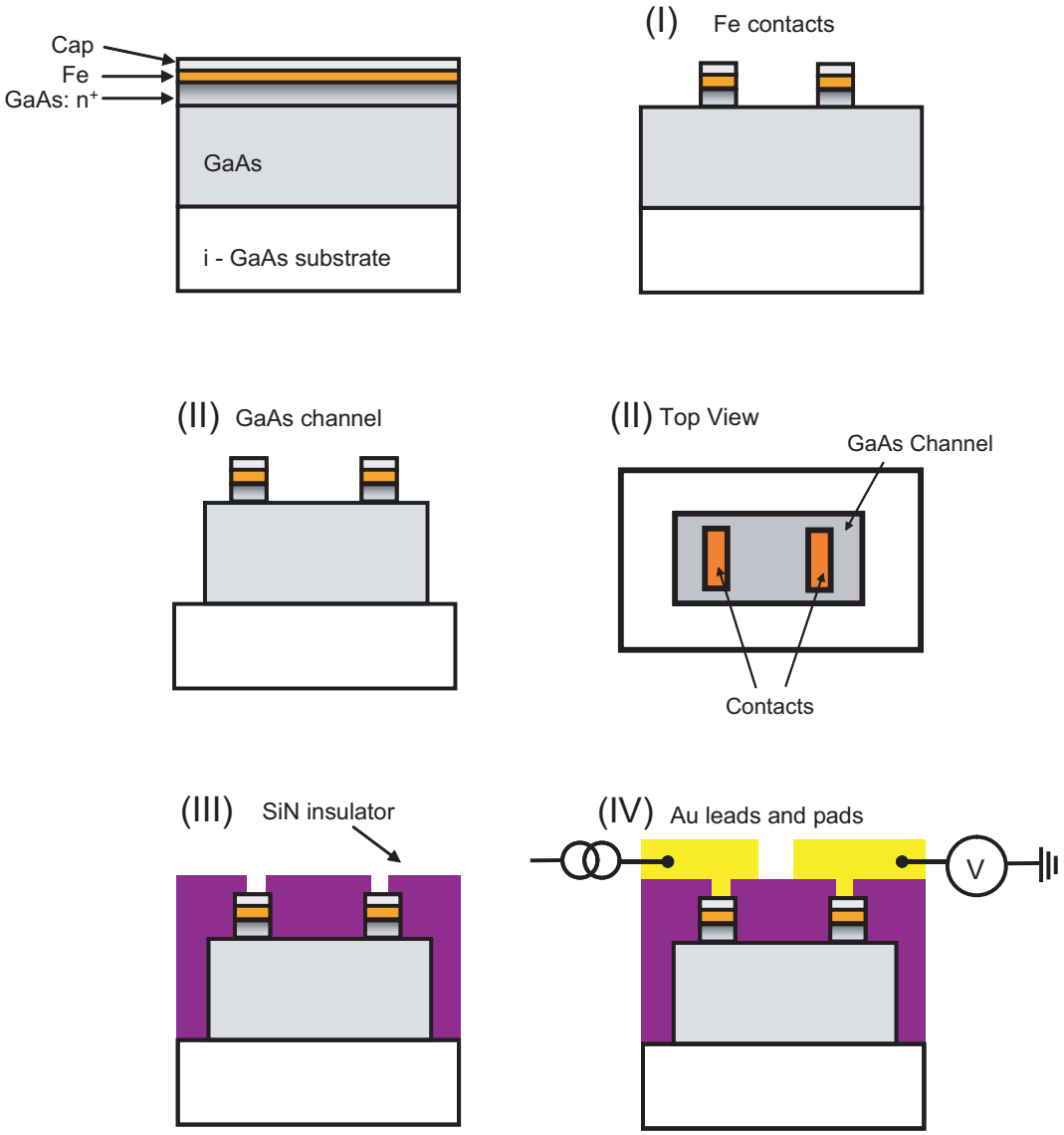

Figure 1.9: Sample fabrication steps. Labels correspond to steps described in the text. Two Fe contacts are shown here. A non-local device would require at least four contacts: the injector and detector as well as two reference contacts.

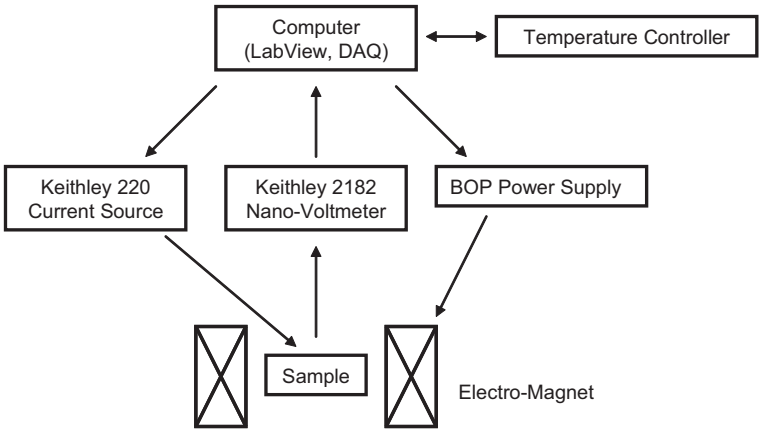

Figure 1.10: Block diagram of experimental electronics.

small electromagnet can be rotated by hand, which allows us to easily change the direction of applied field relative to the sample. The sample is positioned at the center of the magnet rotation axes, ensuring that the field calibration is unchanged when the magnet is rotated. Electrical nuclear magnetic resonance NMR measurements, described in Chapter 2, were typically performed at T = 60 K at the beginning of each measurement block (when the cryostat is cooled down) in order to ensure the field calibration was accurate.

The simplicity of the experimental setup allows us extreme flexibility. For example, we can easily add additional magnetic fields by incorporating Helmholtz coils. Additionally small coils can be mounted inside the cryostat in order to apply an AC field as was done for NMR measurements. High frequency rf coax cables can also be incorporated into the cryostat for future high frequency measurements.

1.5 Spin Detection

1.5.1 Non-Local Spin Detection

As shown in Fig. 1.2, once spins are injected, they are transported in N or SC through diffusion for length scales determined by the spin diffusion length. For GaAs, the electron spin polarization a distance x from the injection point is given by $P = P_0 e^{-x/\lambda}$, where P_0 is the injected spin polarization and λ is the spin diffusion length in the GaAs channel. Silsbee predicted that the inverse of spin injection (applied voltage at an F/N interface generates spin accumulation in N) can apply for spin detection, i.e. the presence of spin accumulation in N can generate an electric voltage at a separate F/N interface.

A schematic diagram of one of our devices is shown in Fig. 1.11(a).[37–39] The heterostructure consists of a 2.5 μm thick Si-doped n-GaAs ($n = 5 \times 10^{16}$ cm^{-3}) channel and 5 nm thick Fe electrodes that are deposited epitaxially on the GaAs (100) surface. x, y, and z correspond to the $[110], [1\bar{1}0]$, and [100] GaAs crystal axes respectively. A Schottky tunnel barrier is formed by a $n \rightarrow n^+$ ($\sim 5 \times 10^{18}$cm^{-3}) GaAs transition layer between the Fe and the n-type channel. The Fe injection and detection contacts are 5×50 μm^2 and 5×80 μm^2 respectively, with a center to center gap of 8 μm. Under forward bias, electrons tunnel from GaAs into the Fe injector (contact b). Spins aligned in the x direction accumulate at the injector interface [38] and diffuse to the non-local detector (contact c). Contact d, located $\sim$ 300 μm$\gg \lambda$ away, serves as a voltage reference. In this configuration the spin detection contact is located nominally outside of the electric current path. By minimizing the electric field at the detector, we reduce

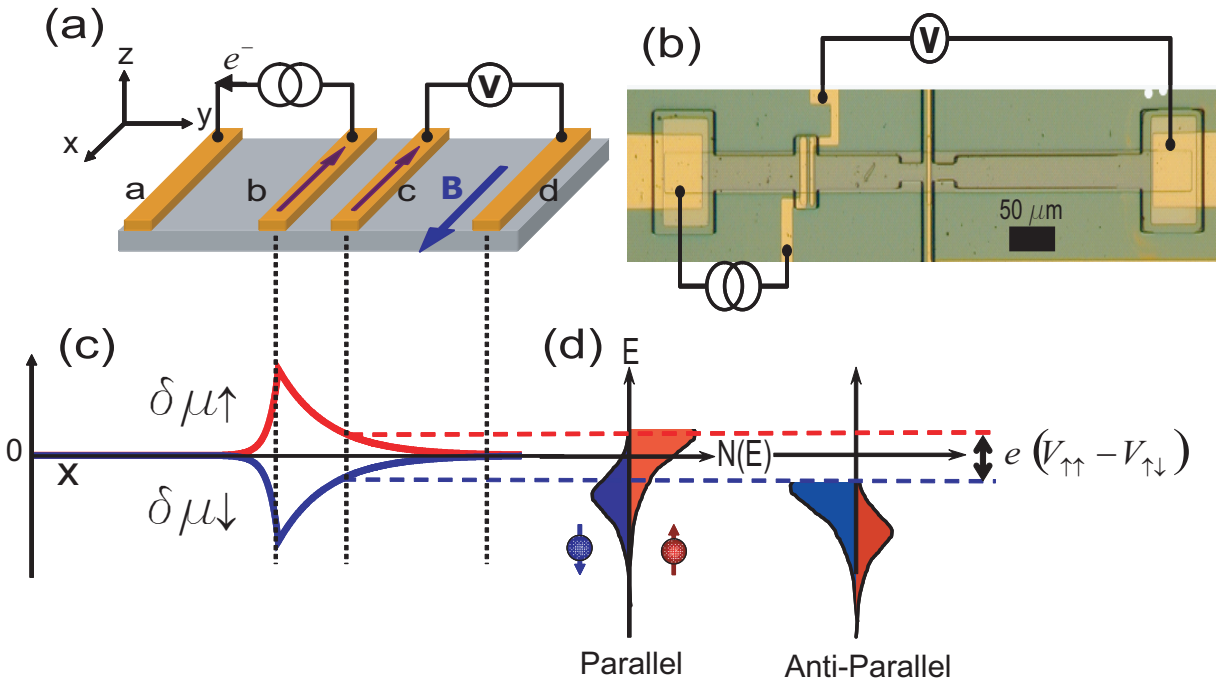

Figure 1.11: (a) Schematic diagram of a typical Fe/GaAs lateral spin valve device. Spin polarization is injected into the *n*-GaAs channel through contact *b*. In this example, a forward bias is applied, although reverse biased contacts can also result in spin injection. The Fe detector *c*, located less than a spin diffusion length away from the injector, is nominally not in the charge current path. This is known as the non-local geometry.[13] The spin polarization in the GaAs channel is monitored by measuring the voltage at *c* relative to a reference contact, *d*, located many spin diffusion lengths away. (b) Optical micrograph of a finished device Q124-3. (c) The spatial dependence of the steady state non-equilibrium chemical potential of up and down spins in the GaAs channel for a forward biased injector. Dotted vertical lines indicate the position of the injector, detector and reference contacts. (d) Configuration of idealized half metallic spin bands of the detector when its magnetization is parallel and antiparallel to the injector magnetization.

the influence of the 'local' Hall voltage that might complicate the interpretation of the measured spin voltage.[28] Additionally, since no current flows into the detector contact, anisotropic magneto-resistance (AMR) does not play a role in the measurement. Fig. 1.11(b) shows the spatial dependence of the non-equilibrium chemical potential of up and down spin channels $\delta\mu^{\uparrow(\downarrow)}$ in the GaAs. $\delta\mu^{\uparrow(\downarrow)}$ decays exponentially once it has been injected into the GaAs. The spin diffusion length to the left of the injector contact is shorter then on the right of the detector because spins are diffusing upstream from the electron flow on the left and downstream on the right. The detector contact is located at a distance $l \sim \lambda$ such that $\delta\mu^{\uparrow(\downarrow)}$ has not fully decayed before reaching the detector. The reference contact (d) is located many diffusion lengths away, so $\delta\mu^{\uparrow(\downarrow)} \approx 0$ there. We assume, for the purpose of illustration, that the detector is a half-metal (only one spin band has non-zero density of states at the Fermi level). When the magnetization of the detector M_d is parallel to that of the injector M_i, as shown in Fig. 1.11, its up spin band lines up with $\mu^{\uparrow}$, resulting in a positive voltage relative to the reference contact. Likewise, we measure a negative voltage when M_d is anti-parallel to M_i. The measured signal between these two configurations, $V_{\uparrow\uparrow} - V_{\downarrow\downarrow}$, is known as the non-local spin valve (NLSV) signal. In our experiment, Fe, which is not a half metal, is used as the detector contact. As a result, the conversion between chemical potential in the GaAs and the measured voltage is

$$\eta'\left(\delta\mu^{\uparrow} - \delta\mu^{\downarrow}\right) = e\Big[V_{\uparrow\uparrow} - V_{\downarrow\downarrow}\Big], \tag{1.38}$$

where

$$\eta' = \frac{G^{\uparrow} - G^{\downarrow}}{G^{\uparrow} + G^{\downarrow}} \tag{1.39}$$

is the spin detection efficiency (it is also called the tunneling spin polarization

TSP in some cases[24]) and depends on the electronic structure of the Fe/GaAs interface, tunneling matrix elements, energy, density of states, and temperature. η' is between 0 and 1. In previous works, we have defined $\eta' = P_{Fe}\eta \approx 0.2$, where P_{Fe} is the Fe spin polarization. In NLSV measurements, a longitudinal magnetic field B_x is swept along the Fe easy axis ([110] direction, labeled x in Fig. 1.11(a)). The measured NL signal as a function of B_x swept from positive(negative) to negative(positive) field is shown in red(black) in Fig. 1.12(a). A clear jump in V_{NL} is observed when M_d and M_i switch from parallel to anti-parallel states. Note that there is a voltage offset of $\sim 150\mu$V, which is attributable to the spread in electric field in the GaAs channel despite the NL configuration of the detector(careful experiments in metallic systems measured in the NL configuration show no offset due to the small electric fields in metals[17, 18]). Fig. 1.12(c) shows the NL spin valve signal with the offset subtracted.

In a degenerate system, we can use Eq. 1.18 to convert between chemical potential and non-equilibrium number density. Assuming the $N^{\uparrow} \approx N^{\downarrow}$ we can write Eq. 1.38 as

$$N(E_F) = \eta' \frac{\delta n^{\uparrow} - \delta n^{\downarrow}}{e\Big[V_{\uparrow\uparrow} - V_{\downarrow\downarrow}\Big]}. \tag{1.40}$$

From the definition of spin density polarization $P = \left(\delta n^{\uparrow} - \delta n^{\downarrow}\right) / \left(\delta n^{\uparrow} + \delta n^{\downarrow}\right)$ and assuming a degenerate 3D density of states

$$P = \frac{e}{\eta'} \frac{3m^*}{\hbar^2 (3\pi^2 n)^{2/3}} \Big[V_{\uparrow\uparrow} - V_{\downarrow\downarrow}\Big], \tag{1.41}$$

where m^* is the effective electron mass ($m^* = .067m_e$ for GaAs). Applying this to the results shown in Fig. 1.12(a) and (c), and assuming $\eta' = 0.2$ which is the estimated zero bias value [62], yields $P = 4.8\%$ at the detector (contact c).

As previously mentioned, the definitive signature of spin polarization is the observation of spin de-phasing in a transverse magnetic field, which is known as the Hanle effect. To observe the Hanle effect, we implement the same measurement configuration shown in Fig. 1.11(a) but with magnetic field applied in the transverse z direction. Note that the saturation magnetization of the Fe contacts for B_z along the [100] direction is approximately 2.1 T.[62] The maximum field applied in the Hanle configuration is $\sim$ 1.5 kOe, and we can safely assume that the magnetization of the Fe contacts are not perturbed. Fig. 1.12(b) shows the NL voltage as a function of transverse field B_z for M_i and M_d in the parallel and antiparallel configurations. Besides the background offset, which was also observed in the NL spin-valve measurements shown in Fig. 1.12(a), there is also a parabolic background. Without any spin signal, one would expect the curves for parallel and antiparallel injector and detector contacts to coincide. We therefore fit the two curves to a second order polynomial outside of -700 to $+700$ Oe, where they are observed to coincide. The resultant *spin-independent* curve, shown as the solid line in Fig. 1.12(b), is then subtracted from the raw NL Hanle curves. The *spin-dependent* curves shown in Fig. 1.12(d) clearly demonstrate spin precession in the GaAs channel.

The Fe detector is only sensitive to spin polarization in the x-direction, i.e. along M_d. Therefore, at $B = 0$ Oe, we observe a maximum in ΔV. As the transverse field B_z is increased, the spin polarization will rotate away from the x-direction resulting in a suppression of ΔV_{NL}. When B_z is sufficiently large, the spin population would have, on average, gone through a $\pi/2$ rotation as it traverses the injector detector gap, resulting in a change in sign of the signal,

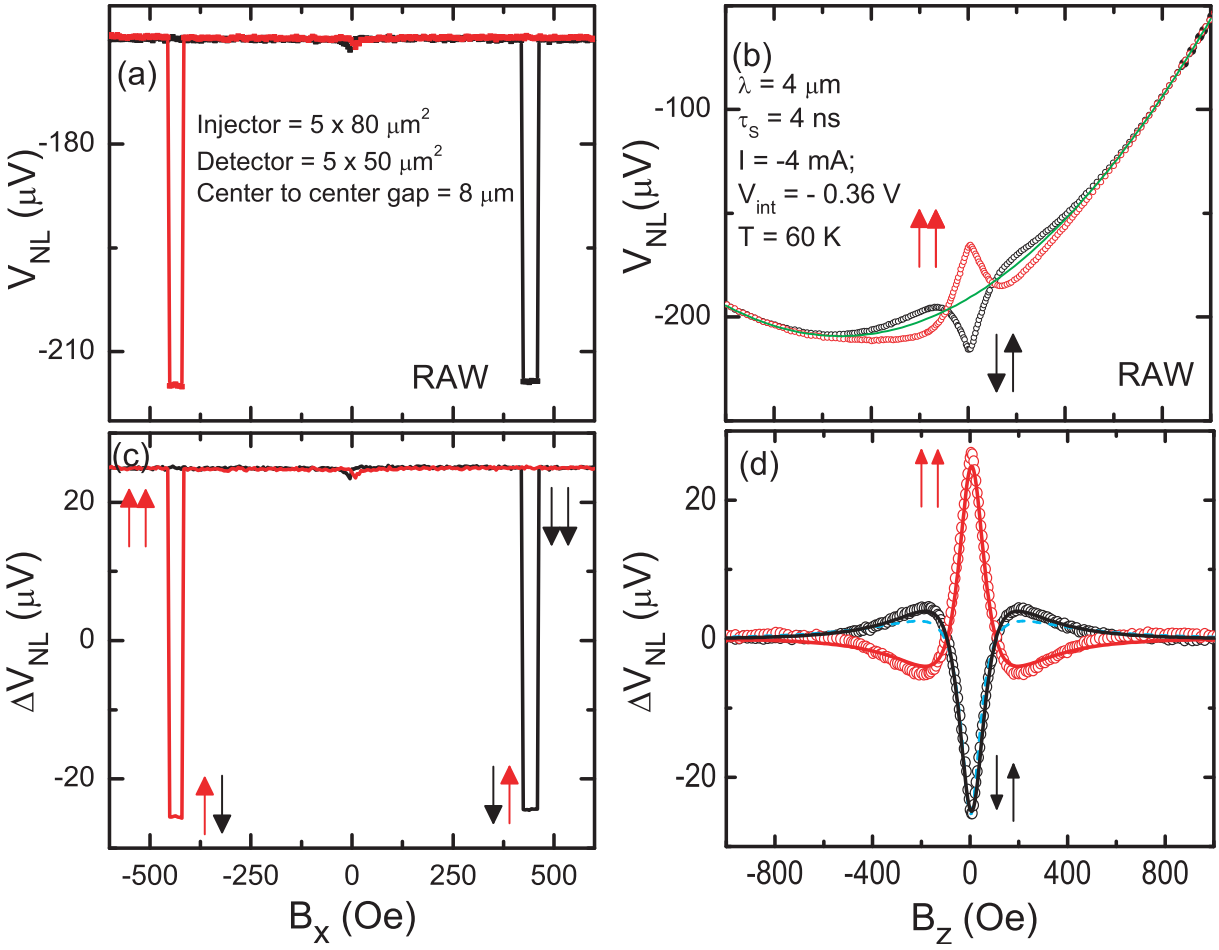

Figure 1.12: (Q62-1) (a) Non-local voltage as a function of longitudinal magnetic field B_x swept from large positive field (red) or large negative field (black). (b) Non-local Hanle voltage as a function of transverse magnetic field B_z for injector and detector magnetization in parallel(red) or anti-parallel(black). The green line is a second order polynomial fitted to NL Hanle curves outside of $\pm$700 Oe. The spin diffusion length λ and spin lifetime τ_s were determined from modeling as described in the text.(c) Non-local spin valve data from (a) with offset subtracted. (d) NL Hanle data (black and red circles) with the green line subtracted from the raw Hanle curves in (c). The solid lines are modeling results as described in the text.

as seen in Fig. 1.12(d) when $B_z \approx 200$ Oe . In addition, we also observe that the spin signal is fully suppressed at large fields. Since the transport of spins from the injector to detector is a diffusive process, the measured spin consists of a population of spins with different arrival times. This means that the measured signal is due to spins with a distribution of phases. At sufficiently large B_z, the phase of the spins within the population is fully randomized, resulting in a null average spin signal. The NL Hanle curves for parallel and anti-parallel injector and detectors, are exactly the same except for a switch in sign, as expected from Fig. 1.11(b)-(d). Note also that the peak-to-peak amplitude of the two Hanle curves at 0 Oe is the same as the NL spin-valve signal within the measurement error limits, showing conclusively that the measured jump in the spin valve signal $V_{\uparrow\uparrow} - V_{\uparrow\downarrow}$ is due to spin, and not Hall, effects.

1.5.2 Three Terminal Spin Detection

An alternative method of detecting non-equilibrium spin polarization in our device is to monitor the voltage drop at the Fe/GaAs injector contact interface. This measurement is achieved by using three terminals: two reference contacts, and a third contact that acts both as the injector and detector. A schematic of the three terminal (3T) measurement is shown in Fig. 1.13(a). A forward bias is applied to the injector contact, thus accumulating spin polarization at the interface. We then monitor the voltage drop at the same contact relative to a reference contact located many spin diffusion lengths away. The injector contact size, in this case, is 5×80 μm^2 (this is the same injector contact used for the NL measurements in Fig. 1.12). An external magnetic field is applied in the transverse z direction in

order to de-phase the spins. The measured voltage as a function of B_z at $T = 60$ K is shown in Fig. 1.13(b). The total voltage drop at the interface is about 322 mV. The most striking feature is the 0.5 mV (or .015% of the total signal) peak centered at $B_z = 0$ Oe. This modulation of V_{3T} with applied magnetic field is a signature of spin accumulation. We can subtract a smooth 2^{nd} order polynomial background, as was done in the NL Hanle measurements, to extract the spin dependent part of the signal, as shown in Fig. 1.13. Just as in the NL measurement, at $B_z = 0$ Oe, the accumulated spin polarization is at a maximum at $B_z = 0$ Oe. However an applied transverse field randomizes the spin polarization of the ensemble of electrons at the contact, resulting in a drop of the signal.

The spin dependent interface signal in the 3T configuration is given by[24, 41]

$$V_{3T} = \eta' \frac{\left(\mu^{\uparrow} - \mu^{\downarrow}\right)}{2e} = \eta' \frac{n}{2eN(E_F)} P_0, \tag{1.42}$$

where the factor of 2 in the denominator accounts for the measurement of average splitting of $\mu^{\uparrow,\downarrow}$. $\eta' = \eta'(V_{int})$ is the bias dependent tunneling spin polarization of the Fe/GaAs Schottky barrier and P_0 is the spin polarization density at the Fe/GaAs interface. In order to convert between the 3T signal and spin polarization in the GaAs, one needs to know the bias dependent $\eta'(V_{int})$. Sec. 1.6.3 will discuss how to determine $\eta'(V_{int})$.

1.6 Modeling Spin Transport and Dynamics

Spin transport and dynamics in the GaAs channel can be understood by a 1D drift-diffusion model which incorporates spin precession given by the following

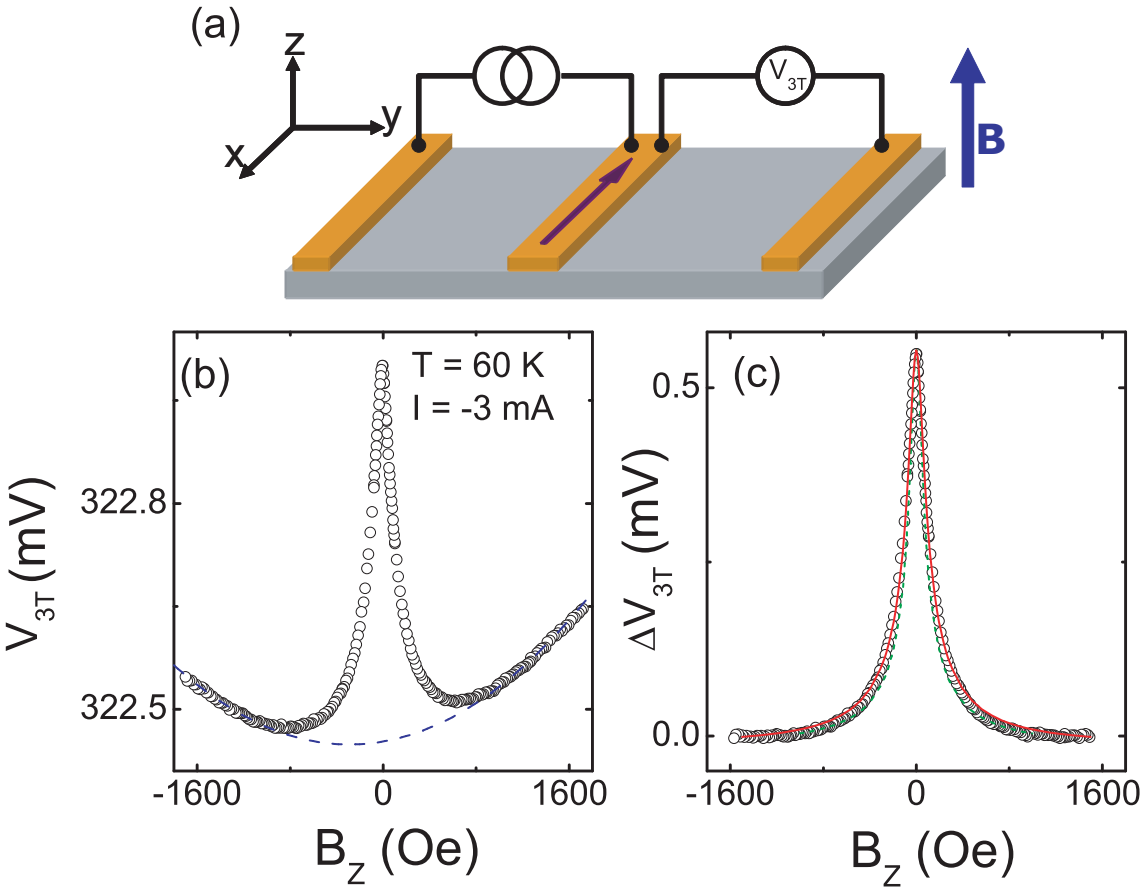

Figure 1.13: (Q62-1) (a) Schematic of the tree terminal (3T) measurement configuration. (b) Raw data of the measured 3T signal as a function of transverse field. (c) Spin dependent 3T signal obtained by subtracting a quadratic background from (b).

differential equation,

$$\frac{\partial \mathbf{S}}{\partial t} = -v_d \frac{\partial \mathbf{S}}{\partial y} + D\frac{\partial^2 \mathbf{S}}{\partial y^2} - \frac{\mathbf{S}}{\tau_s} - \Omega_L \times \mathbf{S}, \tag{1.43}$$

where τ_s is the spin lifetime in the GaAs channel, $\Omega_L = g^*\mu_B B/\hbar$ is the Larmor frequency, $g^* = -0.44$ is the effective electron g-factor in GaAs, and μ_B is the Bohr magneton. $\mathbf{S}$ is the average spin polarization in the GaAs channel, such that $|S| = 1/2$ is equivalent to $P = 100\%$. An approximate solution to Eq. 1.43 for initial spin S_0 transported from y_1 to y_2 is given by

$$S_x(y_2, y_1, B, t) = \frac{S_0}{\sqrt{4\pi Dt}} e^{-(y_2 - y_1 + v_d t)^2/4Dt} e^{-t/\tau_s} \cos(\Omega_l t). \tag{1.44}$$

In order to obtain the steady state spin polarization of injected spins measured at a detector, we have to integrate over all arrival times and the areas of the injector and detector contacts:

$$S_x(B) = \int_{i_1}^{i_2} dy_1 \int_{d_1}^{d_2} dy_2 \int_0^\infty dt \frac{S_0}{\sqrt{4\pi Dt}} e^{-(y_2 - y_1 + v_d t)^2/4Dt} e^{-t/\tau_s} \cos(\Omega_l t), \tag{1.45}$$

where i_1, i_2 and d_1, d_2 are the injector and detector edges respectively.

Using injector and detector widths determined from optical micrographs of finished devices, we can calculate $S_x(B)$ from Eq. 1.45 with S_0 determined from the size of the NLSV signal and setting $v_d = 0$ in the non-local configuration. τ_s and D are as free parameters. The results are shown as the solid lines in Fig. 1.12 (d). The successful fit allows us to determine that $\tau_s = 4$ ns and $D = 4$ μm^2/ns, thus yielding $\lambda = \sqrt{D\tau_s} = 4$ μm.

1.6.1 Numerical Modeling of Spin Transport

The analytical solution of the drift diffusion equation given in Eq. 1.45 assumes that the transport coefficients are spatially constant. However, in the non-local

configuration, $E = 0$ between the injector and detector but not underneath the injector contact. A numerical solution can account for the spatial inhomogeneity of the electric field. Additionally, as will be discussed in Chapter 2, the electron spin dynamics is coupled to the nuclear spin polarization in the GaAs channel. The self consistent numerical approach introduced in this section is essential to understanding the coupled electron-nuclear spin system in our devices. Here we will describe the Crank-Nicolson method of solving partial differential equations.[68] In order to perform a numerical calculation we define a rectangular grid representing the spatial and temporal extent of the simulation. Each are divided into discrete cells, which are parameterized by $t = 0, 1, \cdots T$ and $y = 0, 1, \cdots Y$ for the temporal and spatial cells respectively. We concentrate first on one component of spin, such that $S_{y,t}$ represents the spin value at cell y and time t. We rewrite Eq. 1.43, ignoring the precession term for now, and replacing $-v_d$, D, and $-1/\tau_s$ by a, b, and c respectively,

$$-\frac{\partial S}{\partial t} + a\frac{\partial S}{\partial y} + b\frac{\partial^2 S}{\partial y^2} + c\frac{S}{\tau_s} = 0, \tag{1.46}$$

which, in the Crank-Nicolson (CN) method, is approximated by replacing S and its partial derivatives by

$$\begin{aligned}
S &= \frac{1}{2}\Big(S_{y,t} + S_{y,t+1}\Big), && (1.47)\\
\frac{\partial S}{\partial y} &= \frac{1}{4\delta y}\Big(S_{y+1,t} - S_{y-1,t} + S_{x+1,t+1} - S_{x-1,t+1}\Big), && (1.48)\\
\frac{\partial^2 S}{\partial y^2} &= \frac{1}{2\delta y^2}\Big(S_{y+1,t+1} - 2S_{y,t+1} + S_{x-1,t+1} + S_{x+1,t} - 2S_{y,t} + S_{x-1,t}\Big), && (1.49)\\
\frac{\partial S}{\partial t} &= \frac{1}{4\delta t}\Big(S_{y,t+1} - S_{y,t}\Big), && (1.50)\\
& && (1.51)
\end{aligned}$$

where δt and δx are the size of the time and space cells respectively. Eq. 1.47 can then be written as

$$AS_{y+1,t+1} + BS_{y,t+1} + CS_{y-1,t+1} = -AS_{y+1,t} - B_2 S_{y,t} - CS_{y-1,t}, \tag{1.52}$$

where

$$\begin{aligned} A &= 2\delta t a + \delta x \delta t b, \\ B &= -4\delta t a + \delta x^2 \delta t c - 4\delta x^2, \\ C &= 2\delta t a - \delta x \delta t b, \\ B_2 &= -4\delta t a + 2\delta x^2 \delta t c + 4\delta x^2. \end{aligned} \tag{1.53}$$

We can then cast Eq. 1.52 in matrix form as

$$\begin{pmatrix} 1 & 0 & 0 & 0 & 0 & \dots & 0 \\ A & B & C & 0 & 0 & \dots & 0 \\ 0 & A & B & C & 0 & \dots & 0 \\ \vdots & & \ddots & \ddots & \ddots & & C \\ 0 & \dots & & & & 0 & 1 \end{pmatrix} \begin{pmatrix} S_{1,t+1} \\ S_{2,t+1} \\ S_{3,t+1} \\ \vdots \\ S_{Y,t+1} \end{pmatrix} = \begin{pmatrix} D_{1,t} \\ D_{2,t} \\ D_{3,t} \\ \vdots \\ D_{Y,t} \end{pmatrix}, \tag{1.54}$$

where $D_{y,t}$ represents the right hand side of Eq. 1.52. The tri-diagonal matrix can be solved very efficiently by Gaussian elimination, which scales linearly with the matrix size (i.e. number of spatial cells). S_y is set to zero at the spatial boundaries. Given the initial condition $S_{y,1}$, we can then solve Eq. 1.54 to determine $S_{y,2}$, which then allows us to determine $S_{y,3}$ and so on.

In order to include all three spin directions and precession into the simulation, we triple the spatial grid, from Y to $3Y$ cells, such that the x, y, and z spin directions are represented by $S_{1,t}$ to $S_{Y,t}$, $S_{Y+1,t}$ to $S_{2Y,t}$, and $S_{2Y+1,t}$ to $S_{3Y,t}$

respectively. The precession of spins is given by (we use superscripts instead of subscripts to indicate the x, y, and z directions to avoid confusion with subscripts indexing spatial cells)

$$\gamma\Big(\mathbf{S}\times\mathbf{B}\Big)^{x} = \gamma\Big(S^{y}B^{z} - S^{z}B^{y}\Big), \tag{1.55}$$

$$\gamma\Big(\mathbf{S}\times\mathbf{B}\Big)^{y} = \gamma\Big(S^{z}B^{x} - S^{x}B^{z}\Big), \tag{1.56}$$

$$\gamma\Big(\mathbf{S}\times\mathbf{B}\Big)^{z} = \gamma\Big(S^{x}B^{y} - S^{y}B^{x}\Big). \tag{1.57}$$

By implementing Eq. 1.47, we can rewrite Eq. 1.52 as

$$\begin{aligned} AS_{y+1,t+1} + BS_{y,t+1} + CS_{y-1,t+1} + \Big(E_2S_{y+2Y,t+1} - E_3S_{y+Y,t+1}\Big) + \\ \Big(E_3S_{y,t+1} - E_1S_{y+2Y,t+1}\Big) + \Big(E1S_{y+Y,t+1} - E_2S_{y,t+1}\Big) \\ = -AS_{y+1,t} - B_2S_{y,t} - CS_{y-1,t} + \Big(-E_2S_{y+2Y,t} + E_3S_{y+Y,t}\Big) \\ +\Big(-E_3S_{y,t} + E_1S_{y+2Y,t}\Big) + \Big(-E_1S_{y+Y,t} + E_2S_{y,t}\Big), \end{aligned} \tag{1.58}$$

where

$$\begin{aligned} E_1 &= 2\delta x^2\delta t B^x, \\ E_2 &= 2\delta x^2\delta t B^y, \\ E_3 &= 2\delta x^2\delta t B^z. \end{aligned} \tag{1.59}$$

Eq. 1.54 is then appropriately modified. The resultant matrix is no longer tri-diagonal. Fig. 1.14 shows S^x calculated as a function of position and time. At $t = 0$, S_0^x is injected at cells $y = 15$ and 16. S_y^x is then evolved over time according to Eq. 1.58. The spin packet drifts upwards, while diffusing and decaying in time. Oscillation of S_y^x over time is due to precession in an applied magnetic field. The steady state spin polarization at the detector for a particular magnetic field is

determined by

$$S^x(B) = \frac{1}{T}\frac{\delta y}{d}\sum_{t=1}^{T}\sum_{y=d1}^{d2} S^x_{y,t}, \tag{1.60}$$

where d is the size of the detector, and the sums are over all time cells and detector cells.

An alternative way to determine the steady state spin polarization is to continually inject spins by increasing the spin polarization at the injector cells by an amount determined by the spin injection rate. When the calculation reaches a steady state, the simulation is terminated and $S_{y,T}$ is the steady state spin. Fig. 1.14(b) shows the spatial and temporal evolution of this calculation. Note that in this example, the system is not yet fully in steady state. More iterations would be executed when modeling data to ensure steady state solutions. The detected steady state spin polarization is given by

$$S^x(B) = \frac{\delta y}{d}\sum_{y=d1}^{d2} S^x_{y,T}. \tag{1.61}$$

Note the sum over all times is no longer needed. Fig. 1.14(c) compares the steady state S^x as a function of position calculated using the two methods. They agree very well, as expected. The continuous injection method typically involves a longer simulation time to reach a steady state, but is required when including hyperfine effects, as will be discussed in Chapter 2.

In actual measurements $v_d = 0$ between the injector and the non-local detector. The drift term is therefore spatially dependent. A second boundary condition is set at the edge of the injector to separate the regions with and without drift velocity. Fig. 1.15 shows the effect of nonuniform drift on the calculated steady state spin distribution. The injector and detector cells are bounded by the dashed

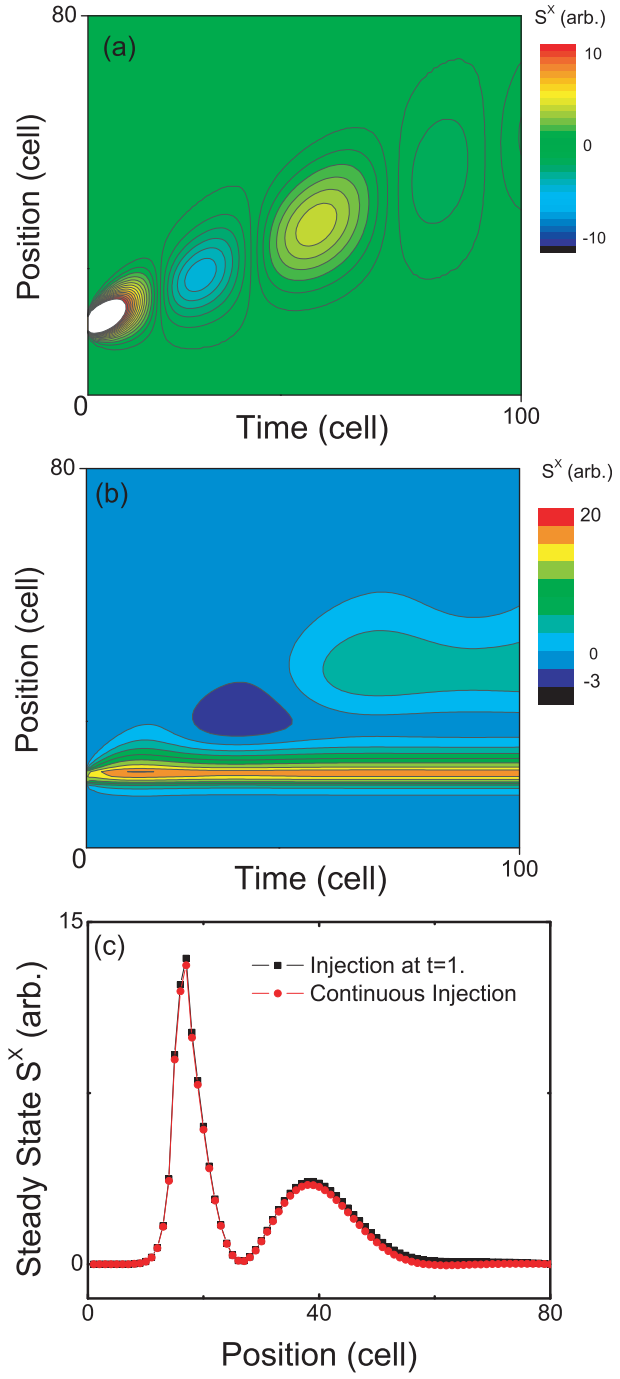

Figure 1.14: (a) Calculated S^x as a function of position and time. At $t = 0$, S_0^x is injected at $x = 15$ and 16. S^x is then evolved over time under the influence of drift, diffusion, decay, and precession around a magnetic field. (b) Calculation of S^x with continuous spin injection. (c) Steady state S^x for initial and continuous spin injection calculated as described in the text.

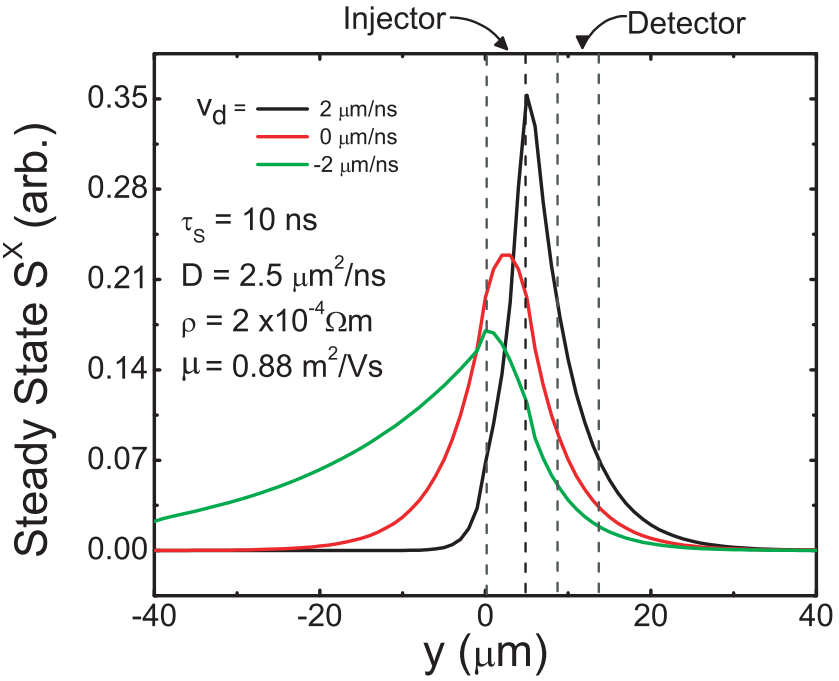

Figure 1.15: Spatial distribution of steady state S^x calculated using the CN method as described in the text. Injector ($y = 0$ to 5) and detector ($y = 8$ to 13) cells are bounded by the dashed lines. $v_d > 0$ corresponds to spins drifting toward positive y (forward biased injector), and *vice versa*.

lines as indicated. Under reverse bias ($v_d < 0$) spins are dragged away from the injector interface, while under forward bias ($v_d > 0$), spins pile up on the right edge of the injector contact. The drift term therefore can effect the measured spin polarization at the NL detector, despite the fact that $v_d = 0$ there.

In order to model the observed Hanle curves, Eq. 1.58 is solved for each magnetic field. We can restrict the number of free parameters in our calculation by fixing D and v_d from transport measurements (as will be discussed in Sec. 1.6.2). The only free parameters are τ_s and the spin injection rate $\dot{S}$. The result is shown (only for the antiparallel case) as the dashed line in Fig. 1.12(d). The fit is reasonably good, except that it underestimates the height of the $\pi/2$ rotation

features. The measured D was 7.5 μm^2/ns and we extracted $\tau_s = 5.2$ ns. The 3T signal is determined by spatially averaging the steady state spin over the injector cells instead of the detector cells. The solid line in Fig. 1.13 is calculated from the CN method using the same modeling parameters used to fit the NL Hanle in Fig. 1.12(d) (dashed blue line). The consistency between the NL and 3T measurements is reassuring. The fitting presented in this thesis will primarily be performed by implementing the CN calculation described in this section.

1.6.2 Transport Properties

There are four unknown parameters in Eq. 1.45: D, τ_s, S_0, and v_d. The drift velocity can be determined using the following relation

$$j = nev_d, \tag{1.62}$$

where j is the current density and n is the carrier density. n is determined from Hall measurements using

$$n = \frac{IB}{deV_{Hall}}, \tag{1.63}$$

where d is the thickness of the current channel and V_{Hall} is the Hall voltage.

The diffusion constant D is determined by the generalized Einstein relation given by[49]

$$D = \frac{2\mu_B k_B T}{e} \frac{F_{1/2}[E_F/k_B T]}{F_{-1/2}[E_F/k_B T]} \tag{1.64}$$

where E_F is the Fermi energy and $F_n[\xi] = \int_0^\infty x^n [\exp(x-\xi)+1]^{-1} dx$. We can determine the mobility using $\mu = 1/(ne\rho)$, where the resistivity ρ is measured in a 4-point configuration. Fig. 1.16(a) shows the measured IV curves for a n-GaAs sample with $n = 5 \times 10^{16}$ cm^{-3} at various temperatures. The IV characteristic

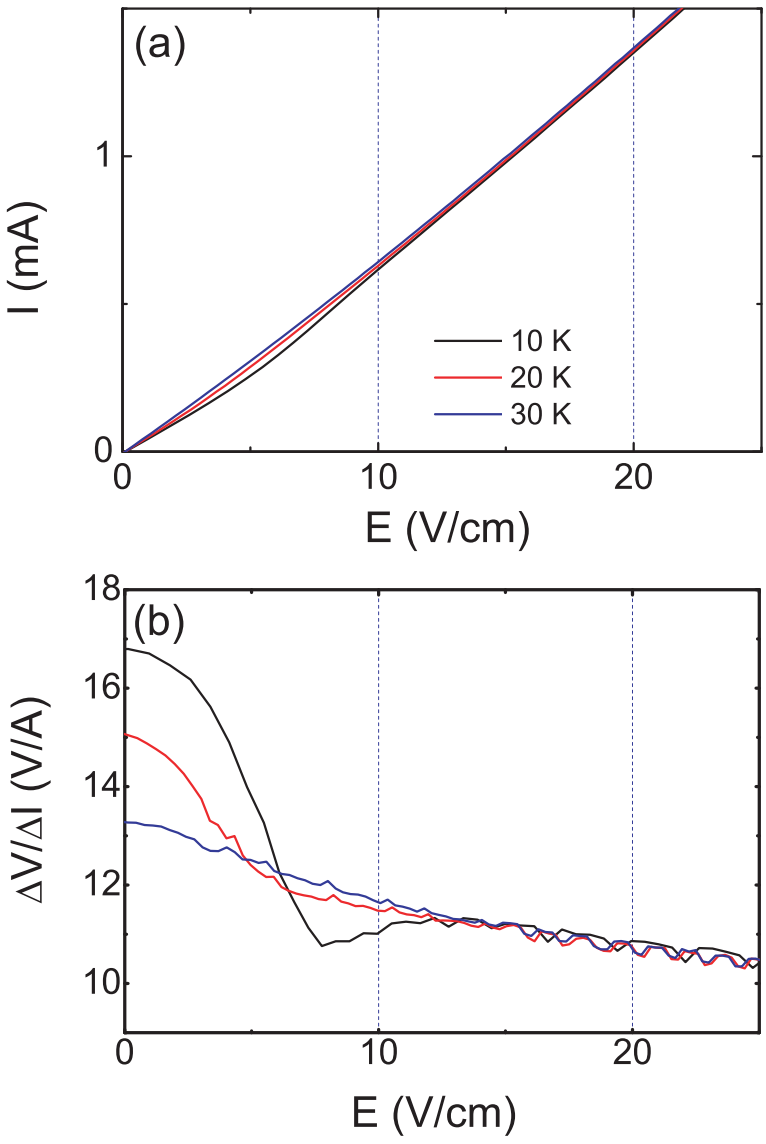

Figure 1.16: (Q62-1) (a) Channel IV curves measured in a 4-terminal configuration for various temperatures. The channel is $\approx$ 80 μm wide and 2.5 μm thick with center to center gap between voltage contacts of 8 μm. (b)$\Delta V/\Delta I$ taken from (a) for various temperatures.

is ohmic at high temperatures. The non-ohmic behavior at low temperatures is indicative of donor impact ionization, which, in n-GaAs, has a threshold of ~ 10 V/cm.[50, 51] This threshold corresponds to the small 'kink' in the IV curves shown in Fig. 1.16(a). We can see this more clearly by looking at the $\Delta V/\Delta I$ curve in Fig. 1.16. Fig. 1.17(a) shows the measured resistivity as a function of temperature for low and high bias. Donor impact ionization at high bias results in a reduction of the resistivity as the large electric fields excite carriers into the conduction band. The high and low bias ρ coincide above ~ 130 K, indicating that donor impact ionization is no longer active. This suggests that electrons are no longer localized on donor sites above 130 K. Above 130 K, the linear relationship between ρ and T indicates the dominance of phonon scattering to the increase in resistivity.

Fig. 1.17(c) shows the temperature dependence of the carrier density for various bias currents. For $I = 0.1$ mA, n has an anomalous minimum at 70 K. As I is increased, n eventually approaches a saturation value (see the 3 mA and 5 mA curves). The mobility determined from the resistivity and Hall measurements is shown in Fig. 1.17(c). The deviation of ρ due to donor impact ionization at low temperatures is reflected in μ. The diffusion constant determined from Eq. 1.64 is shown in Fig. 1.17(d).

1.6.3 Spin Valve: Bias Dependence.

We can change the injected spin polarization in the GaAs channel by changing the bias applied on the injector contact. Fig. 1.18(a) and (b) show the NLSV

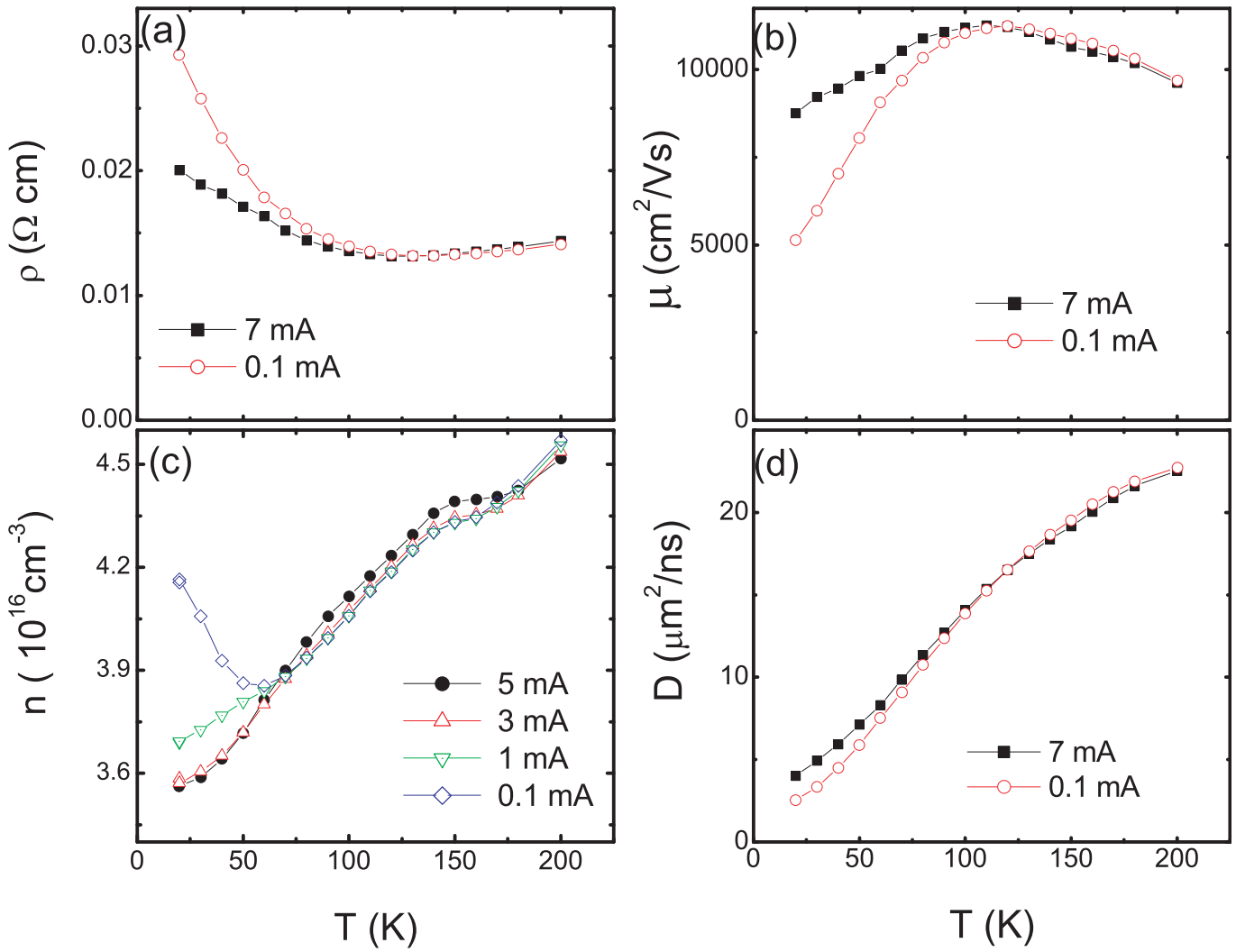

Figure 1.17: (Q59-9) Temperature dependence of resistivity ρ (a), mobility μ (b), carrier density n (c), and diffusion constant D (d) for high and low applied channel bias. The GaAs channel is ≈ 80 μm wide and 2.5 μm thick.

measurement configuration and the bias dependence of the spin signal as a function of injector bias. The NLSV signal increases with increasing forward bias while it is significantly smaller under reverse bias, and includes a change in sign between $0.1\ V > V_{int} > 0.3\ V$. Kerr effect measurements show that Fe majority spin polarization is accumulated at the Fe/GaAs interface under large forward and reverse biases, while minority spin polarization accumulates in the small bias window where the NLSV signal changes sign.[39] In linear response, one expects majority spin accumulation for a reverse biased contact and minority spin accumulation for a forward biased contact. The marked deviation from linear response of the NLSV signal reflects a complicated bias dependence of the spin injection efficiency.

The open circles in Fig. 1.18(d) are the current spin polarization α_0 at the injector calculated from the NLSV measurement shown in Fig. 1.18(a). To obtain α_0, we first calculated P_{NL} using Eq. 1.41 with $\eta' = 0.1$ (for self consistency) and the NLSV signal shown in Fig. 1.18(b). The spin polarization at the injector P_0, is then determined by backtracking from P_{NL} in the CN simulation. Finally α_0 was calculated from Eq. 1.17 for a forward biased contact. Note that Eq. 1.17 states that $\alpha_0 \propto P_0/(j\lambda_d)$, where λ_d depends on the electric field at the injector, and accounts for the drift effects on the spin polarization density. For moderate bias voltages, the qualitative bias dependence of α_0 agrees with that of the NLSV signal. For large forward bias, however, the NLSV signal continues to increase, while α_0 decreases, with increasing bias. The reason is that for large forward bias, the shrinking of the accumulation region due to the electric field at the Fe/GaAs interface, as described by Eq. 1.17, results in a continued increase in P_0, despite

the decrease of spin injection efficiency α_0.

The variation of α_0 with injector bias shown in Fig. 1.18(d) suggests that the spin injection efficiency of the Fe/GaAs Schottky barrier is strongly dependent on the interface voltage. From reciprocity considerations, we expect that the spin injection efficiency and spin detection sensitivity of an Fe/GaAs barrier are the same. The two should have the same interfacial bias dependence. We can therefore access the bias dependence of spin injection efficiency by studying the detection sensitivity of a biased detector. To this end, we employ the measurement configuration shown in Fig. 1.18(c). An AC unipolar voltage of -0.2 V_{pp} is applied to the injector contact (contact b) to inject a spin polarization packet δP_0. The spin packet, then diffuses to the detector where a spin dependent voltage is measured using a lock-in amplifier, which is only sensitive to the AC spin polarization injected at contact b. A magnetic field is swept along the x direction, while the lock-in amplifier voltage is monitored, resulting in spin valve data shown in Fig. 1.19. The detector contact (contact c) is biased by a DC current source in order to ascertain the dependence of the detection sensitivity on applied bias. A summary of the spin valve signal ΔV_d as a function of detector bias is shown in Fig. 1.18(d). We see that under modest forward bias the detection sensitivity is amplified. At higher forward bias, however, the amplification saturates and eventually decreases, and drops below the zero bias value at the highest detector bias applied. Under reverse bias, ΔV_d is suppressed and then changes sign within a small bias window between approximately 0.05 V and 0.25 V, in accordance with the sign change observed in the traditional NLSV signal shown in Fig. 1.18(b). Strikingly, the bias dependence of ΔV_d agrees very well with α_0 determined from

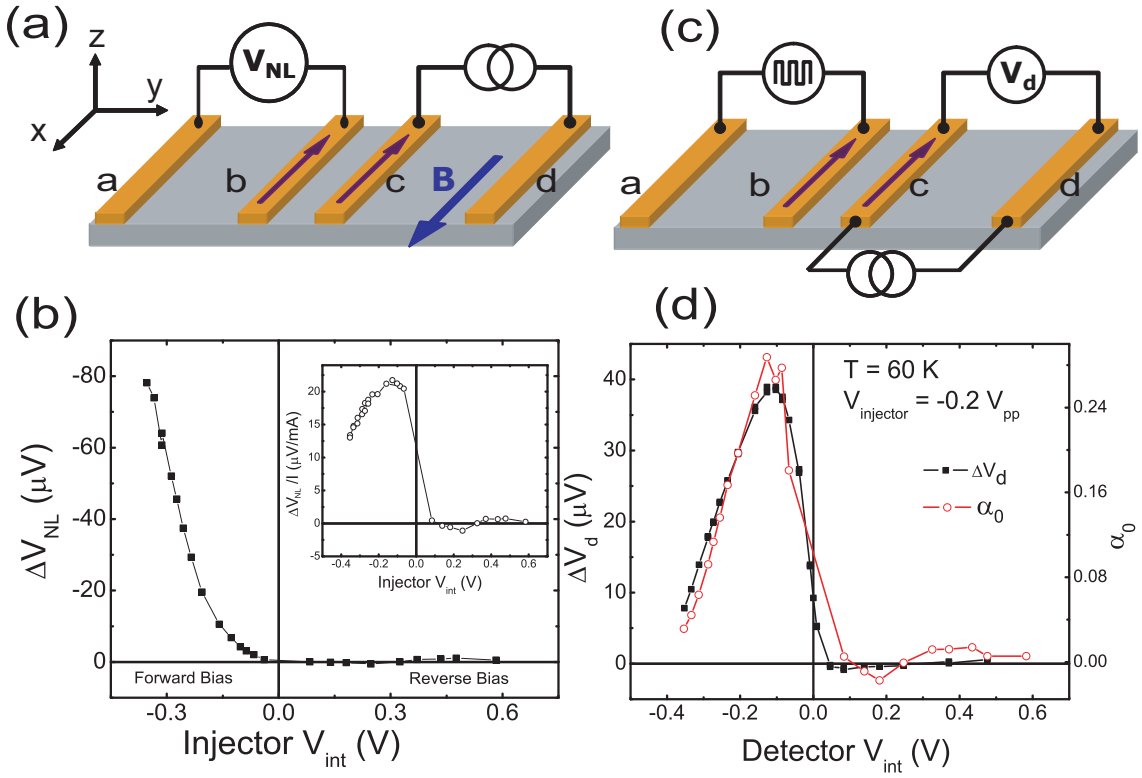

Figure 1.18: (Q59-6) (a) Schematic of the NLSV measurement configuration. Contacts c and b act as the injector and detector contacts respectively. Contact c is 8 μm^2 and contact b is 5 μm^2. The edge to edge separation is 3 μm. (b) NLSV signal as a function of applied injector bias V_{int}. Inset: NLSV normalized by the injection current as a function of injector bias. (c) Schematic of the detector bias configuration. The same device was used for the NLSV measurement shown in (a). Contact b is now the injector and c the detector. The detector is biased by a DC current source. (d) Detection sensitivity ΔV_d as a function of detector bias.(solid squares) Also shown is the current polarization at the injector of the NLSV measurement α_0 calculated from the NLSV signal as described in the text.(open circles)

NLSV measurements.

In work by Crooker and co-workers [67], the bias dependence of ΔV_d was compared directly to $\Delta V_{NL}/I$, which is shown in the inset of Fig. 1.18(b). They observed the amplification of ΔV_d relative to $\Delta V_{NL}/I$ for the forward bias range they measured (< 200 mV). They attributed this amplification to drift which pushes spins injected at the remote NL injector towards the detector contact, thus increasing the spin polarization density with increasing bias.[72]. As seen in Fig. 1.18(d) and the inset of Fig. 1.18(b), we observe a similar amplification of ΔV_d relative to $\Delta V_{NL}/I$ under modest forward bias as well. However, we also observe a suppression of ΔV_d relative to $\Delta V_{NL}/I$ at large forward biases ($V_{int} > 200$ mV). This supression is not explained by the model in Refs. [67] and [72].

In our analysis, we compare ΔV_d not to $\Delta V_{NL}/I$, but to $\alpha_0 \propto P_0/(j\lambda_d)$, where $P_0 \propto \Delta V_{NL}$, as discussed above. The additional factor of λ_d, which increases with increasing bias, in the denominator of the expression for α_0 accounts for the additional enhancement and suppression of ΔV_d relative to $\Delta V_{NL}/I$ under small and large biases respectively. We therefore do not need to invoke drift effects on the spin packet injected from the remote *non-local* injector in the detector bias experiments.

The reason that α_0 tracks the bias trend of ΔV_d closely can be explained by looking at Eq. 1.32: $\alpha_0 = (R_F + R_-) / (R_F + R_{SC} + R_+)$. R_F and R_{SC} can be ignored since $R_F \equiv [\alpha_F \lambda_F \rho_F] / [1 - \alpha_F^2] \sim 10^{-14}$ Ωm^2 and $R_{SC} \equiv \lambda_{SC}\rho_{SC} \sim 10^{-10}$ Ωm^2 are much smaller than $R_+ \sim 10^{-7}$ Ωm^2 and R_- for appreciable spin dependent tunneling. We therefore expect that the interface voltage dependence

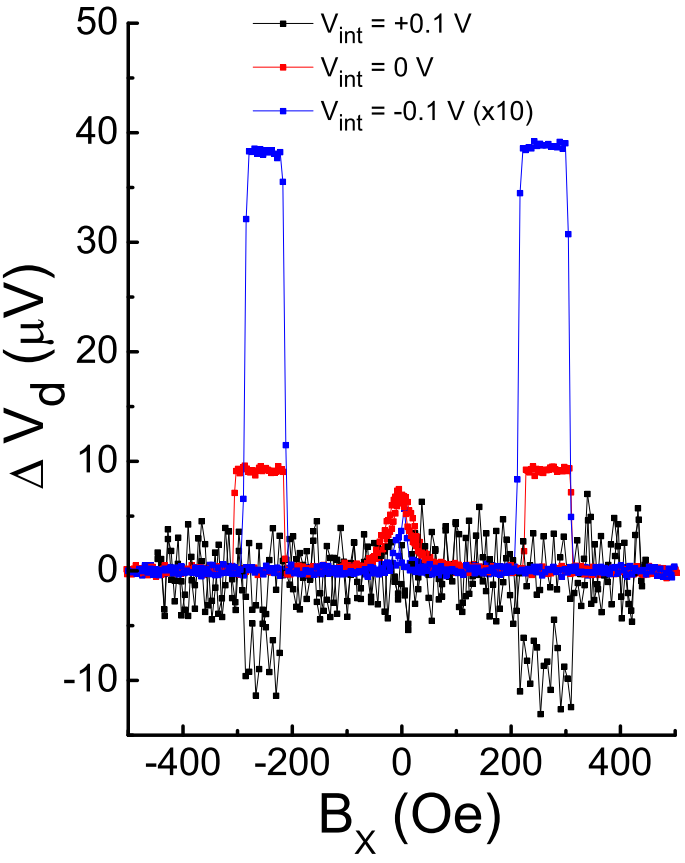

Figure 1.19: (Q59-6) Spin valve data in the detector bias configuration for detector bias of 0.1 V (signal multiplied x10), 0 V and −0.1 V. A spin independent linear background was subtracted from the data.

of α_0 is approximately equal to that of η':

$$\alpha_0(V_{int}) \approx \frac{R_-}{R_+}(V_{int}) = \eta'(V_{int}). \tag{1.65}$$

In the detector bias experiment, the detected spin signal is written analogously to Eq. 1.41 as

$$\Delta V_d = \eta'(V_{int}) \frac{n}{eN(E_F)} \delta P, \tag{1.66}$$

where δP is the spin polarization at the detector due to spins injected at the remote injector, and $\eta'(V_{int})$ is the detector bias dependent tunneling spin polarization. It is clear that ΔV_d is a direct measure of the bias dependence of η', as demonstrated from the data in Fig. 1.18(b). η' therefore increases with small forward bias, but then decreases at large forward bias. Under reverse bias, η' is significantly smaller. A sign change is also observed under small reverse bias.

The analysis in this section provides a simple method of studying the spin injection efficiency in these devices. Particularly important, is that it allows us to determine the zero bias detection efficiency $\eta'(0)$ which is essential for converting between a measured NLSV signal and the actual spin polarizations in the GaAs channel.

The marked deviation of α_0 from linear response is a result of the complicated dependence of the up and down spin density of states at both sides of the Fe/GaAs interface. There are a number of theoretical works addressing the bias dependence of spin injection/extraction at an Fe/GaAs interface. Most of them concentrate on the change between majority and minority spin injection at low biases. η' is dependent on many properties of the Fe/GaAs interface. Smith and Ruden assumed s type Fe bands with an spin up and down exchange splitting. They calculated the tunneling current from the simplified Fe band structure into GaAs

across a simplified triangular Schottky tunnel barrier and found that sign changes can occur under both forward and reverse bias.[70] Other authors have found that the Fe/GaAs interfacial electronic structure can significantly impact spin injection.[71] Dery and Sham noted the possible contribution of localized states at the shallow quantum well formed at the GaAs side of the interface to spin dependent tunneling.[69]

1.6.4 Three Terminal: Bias Dependence.

With the knowledge of $\eta'(V_{int})$, we can now turn to the interpretation of the 3T signal. Fig 1.20 shows the measured magnitude of the 3T signal as a function of bias for the same device and injector contact used in Fig. 1.18. ΔV_{3T} increases monotonically as a function of forward bias. A 3T spin signal is only observed under forward bias. When the injector is reverse biased, electrons tunnel from Fe into empty GaAs states which are at an energy $\gg k_B T$ above the GaAs quasi Fermi energy. The low occupancy of these states result in tunneling that is independent of the spin polarization in the GaAs channel.[39]

The dependence of the NL signal on η' is given by $V_{NL} \propto \eta'(V_{int})\eta'(0)$ where $\eta'(V_{int})$ accounts for the spin injection efficiency at the biased injector and $\eta'(0)$ is the spin detection efficiency of the non-local detector, which is not biased. In the 3T configuration on the other hand, the same contact acts as both the injector and the detector. Therefore $V_{3T} \propto \eta'(V_{int})^2$.

Fig. 1.21(a) shows P_0 determined from both the 3T and NL measurements. P_0 is extracted from the 3T signal using Eqs. 1.42 and 1.17, where the effective spin diffusion length is also bias dependent and shown in Fig. 1.21(b). P_0 from

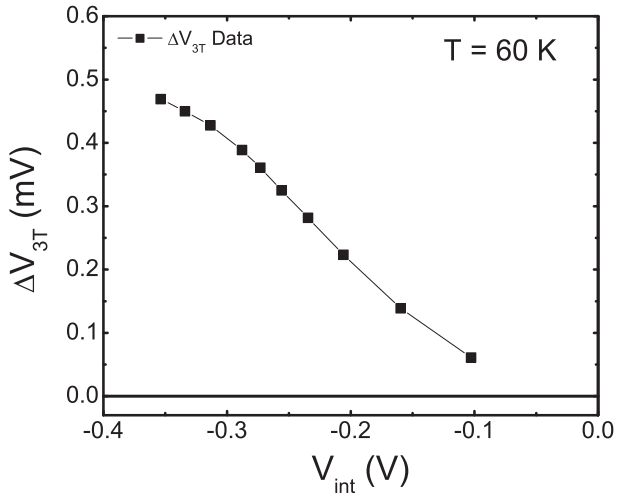

Figure 1.20: (Q59-6) Injector bias dependence of the three terminal signal magnitude at T = 60 K.

the NLSV signal is determined by calculating P at the NL detector using Eq. 1.41 then determining what P_0 would have to be in the CN calculation. We see that P_0 determined from the 3T and NL measurements agree quite well with each other up to $V_{int} \approx -250$ mV. At large forward bias however, the 3T signal continues to increase with increasing bias, resulting in a large increase in P_0. P_0, as determined from the NL measurements, however, saturates at high biases.

The 3T signal is between 6 to 9 times larger than the NL signal of the same bias. If we account for the diffusion of spins from the injector to detector contacts, we find that the spin polarization at the injector contact is only about 1.5 to 2 times larger than at the NL detector. The amplification of the 3T signal can be attributed to the increase in spin detection sensitivity of the Fe/GaAs Schottky tunnel barrier, as discussed in Sec. 1.6.3 and Fig. 1.18(d), under modest bias. At high bias however, the $\eta'(V_{int})$ starts to decrease, and the amplification factor decreases correspondingly, thus resulting in the saturation of P_0 at high bias as

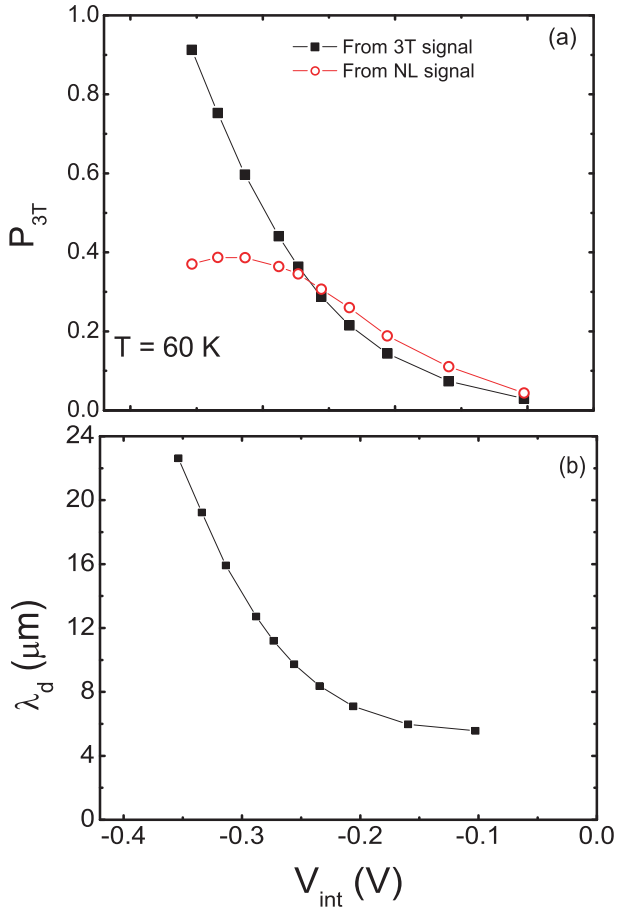

Figure 1.21: (Q59-6) (a) Spin polarization density at the Fe/GaAs interface (P_0) as a function of interface voltage (V_{int}) determined from the NLSV(open circles) and 3T(closed squares) signal magnitudes as described in the text. (b) Effective spin diffusion length λ_d for a forward biased contact as a function of V_{int}.

determined from the NLSV signal. The 3T signal however, continues to increase at high bias, despite the drop in η' shown in Fig. 1.18(d). A possible reason for the deviation at high bias is that the polarization at the injector P_0 as determined from the 1D CN method might not accurately represent the accumulated spin polarization in a real device. As discussed previously, our CN calculation only accounts for the lateral drift effects. It is quite possible that the real P_0 is much higher in a our device due to the large electric fields pushing spins towards the interface under forward bias. Nevertheless, the consistency between the measured spin dependent voltage size between the detector bias, non-local and 3T measurements at modest biases is reassuring.

1.7 Temperature Dependence

Fig. 1.22 shows the temperature dependence of Hanle curves measured in both the three terminal and non-local configurations. The nuclear field elimination procedure as will be described in Sec. 2.6 was implemented to avoid hyperfine effects. Fitting was performed using the CN method. D and v_d for each temperature were determined from Fig. 1.17. τ_s is a free parameter. 3T and NL curves were fit with the same D and τ_s while the magnitude of the peak was fit to the data. The calculated curves are shown as solid lines in Fig. 1.22. The successful fits allow us to extract the spin lifetime over a wide temperature range, as shown in Fig. 1.23. The fact that both NL and 3T curves were successfully fit to the same parameters gives us confidence in our extracted spin lifetimes. As the spin lifetime becomes smaller at higher temperatures, the width of the Hanle curves increases. The measured NLSV and 3T signals also decreases at higher temperatures. The spin

signal is not resolvable above 200 K. The injected spin polarization $P_0 \propto \lambda/D$. As the temperature increases, λ decreases, and D increases, thus partially explaining the drop in the measured spin signals with increasing temperature. We expect that the spin injection efficiency is temperature dependent as well. If we account for the temperature dependence of λ and D, we can determine the temperature dependence of α_0 from Eq. 1.17 as shown in Fig. 1.24. As discussed in Sec. 1.6.3: $\alpha_0 \approx \eta'$. Therefore, we can equate the temperature dependence of α_0 shown in Fig. 1.24 to the temperature dependence of the spin injection efficiency η'. It is clear that for $T < 60$ K, the drop in spin signal with increasing temperature is accounted for by the drop in the spin injection efficiency. However, above 60 K, the NLSV signal drops more sharply than α_0. This is due to the decrease in accumulated spin polarization P_0 we have just discussed and the drop in λ, which means a larger proportion of P_0 would decay before reaching the NL detector. Although the NLSV signal is not observed above 200 K, the spin injection efficiency only drops by a factor of 5 between 20 K and 180 K, and remains appreciable at high temperatures. This is roughly consistent with spin-LED measurements.[62] We therefore expect to be able to inject and detect spin polarization in Fe/GaAs heterostructures at temperatures exceeding 200 K if we fabricate devices with smaller injector/detector contacts and smaller injector-detector gaps.

The D'yakonov-Perel (DP) mechanism[75] is typically thought to be responsible for spin relaxation in III-IV semiconductors at the doping range studied here.[59] The lack of bulk inversion symmetry induces spin splitting, which can be described by an intrinsic $\mathbf{k}$-dependent magnetic field $\mathbf{B_i}(\mathbf{k})$. The Larmor frequency of spin precession associated with this intrinsic field is $\mathbf{\Omega}(\mathbf{k}) = (e/m)\mathbf{B_i}(\mathbf{k})$. In

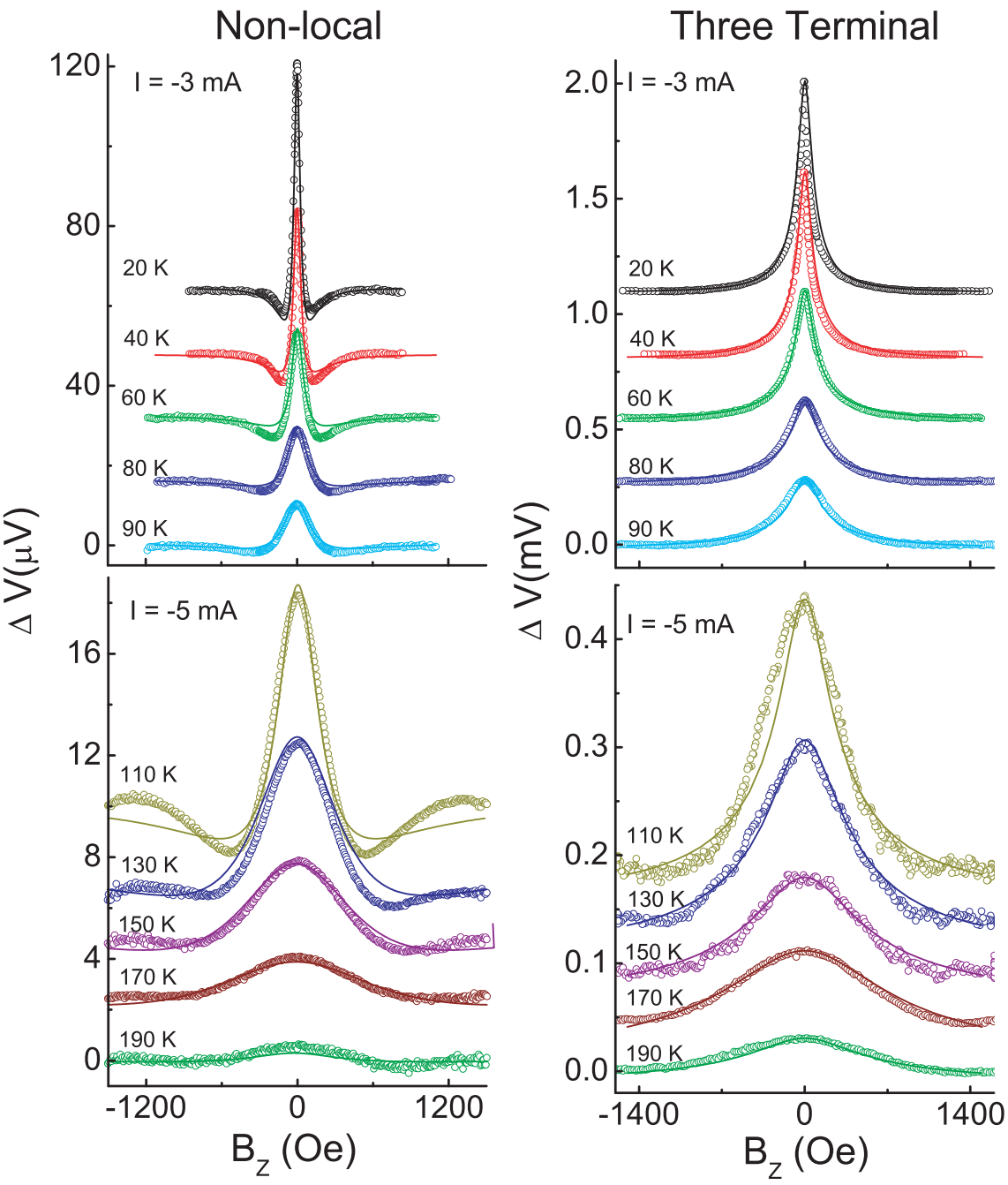

Figure 1.22: (Q62-1) Non-local (left panel) and three terminal (right panel) Hanle curves for different temperatures. Data are open circles. Solid lines are calculated curves as described in the text. Both are vertically offset for clarity. The injector and NL detector are 5×80 μm^2 and 5×50 μm^2 with a 8 μm center-to-center gap.

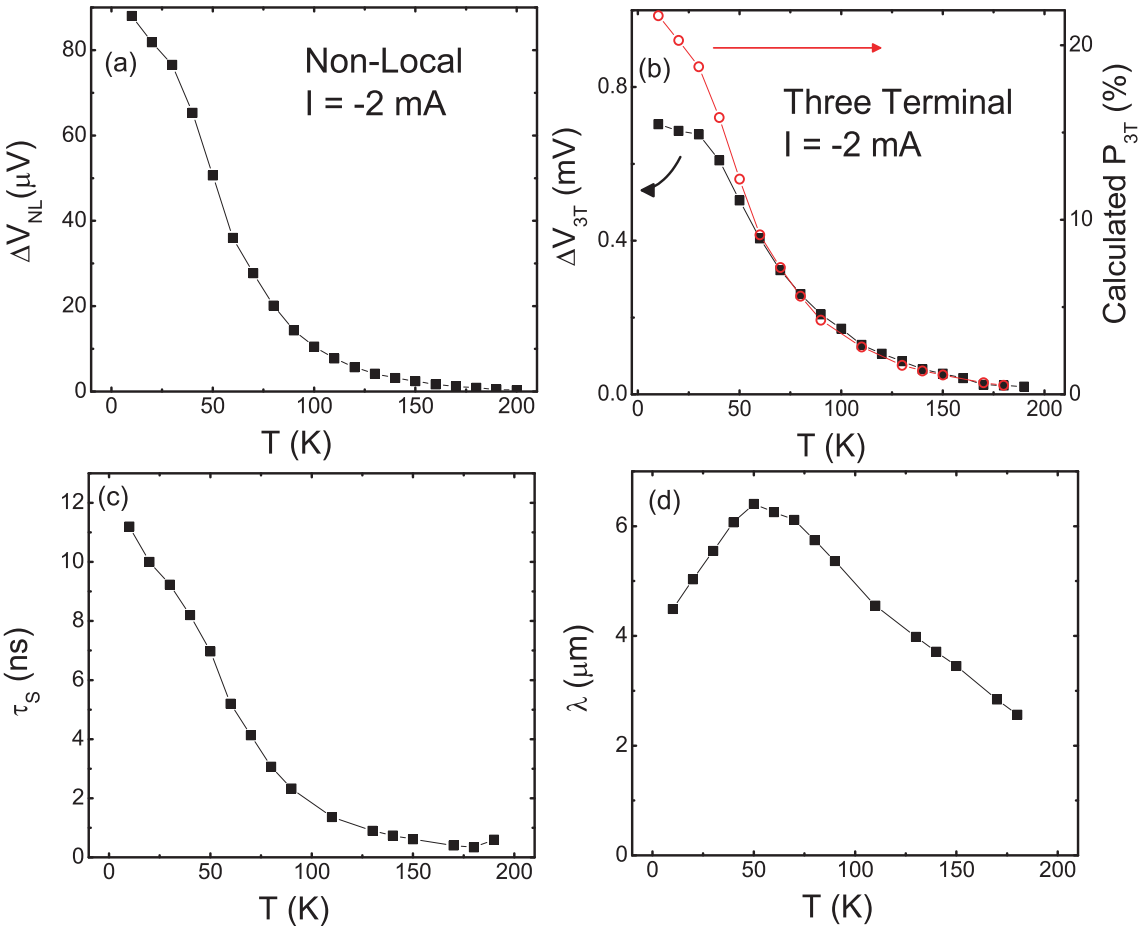

Figure 1.23: (Q62-1) (a) NLSV signal as a function of temperature. (b) 3T signal (closed squares) and calculated density polarization P at the injector contact (open circles) calculated from the NLSV signal. (c) Spin lifetime τ_s extracted from fitting Hanle curves. (d) Spin diffusion length $\lambda = \sqrt{D\tau_s}$.

the regime $\tau_p \Omega_{av} \lesssim 1$, where Ω_{av} is the intrinsic Larmor frequency averaged over the actual momentum distribution. Spins precess about the intrinsic field. In between scattering events, the electron spin picks up a phase angle $\delta\phi = \Omega_{av}\tau_p$. At each scattering event, the electron momentum changes. So, the magnitude and direction of Ω_{av} changes randomly with time step τ_p. If clockwise and anti-clockwise precession are equally likely, the average spin phase does not change, but the root mean square phase increases in time as $\langle \Delta^2 \phi \rangle^{1/2} \approx \Omega_{av}\tau_p (t/\tau_p)^{1/2}$. The spin relaxation time τ_s is defined as the time over which $\langle \Delta^2 \phi \rangle = 1$ such that

$$\frac{1}{\tau_s} = \Omega_{av}^2 \tau_p. \tag{1.67}$$

For GaAs, the spin splitting is proportional to the cube of the lattice momentum.[74] A calculation of Ω_{av} for the Dresselhaus splitting performed by Pikus and Titkov results in the following expression for the spin lifetime of degenerate electrons[73]:

$$\frac{1}{\tau_s} = \frac{32}{105}\gamma_3^{-1}\beta^2 \frac{E_{\mathbf{k}}^3}{\hbar^2 E_g}\tau_p. \tag{1.68}$$

where β is dimensionless and parameterizes the strength of the spin-orbit coupling. $\beta \approx 0.07$ in GaAs, [76] and $\gamma_3 = 1$ or 6 for acoustic phonon or impurity scattering respectively. $E_{\mathbf{k}}$ is replaced by the Fermi energy E_F for the degenerate case. E_F is calculated for a bulk material using carrier density n determined from Hall measurements. Fig. 1.25 shows the calculated τ_s from Eq. 1.68 for the case of impurity and acoustic phonon scattering. τ_p was determined from the measured resistivity shown in Fig. 1.17 and the Drude formula. The general temperature dependence of τ_s reproduces that seen in our data. Specifically, it is large at low temperatures, decreases as temperature increases, and eventually reaches a low plateau above approximately 110 K. The temperature dependence of the resistivity shown in Fig. 1.17 indicates that impurity scattering is dominant at low

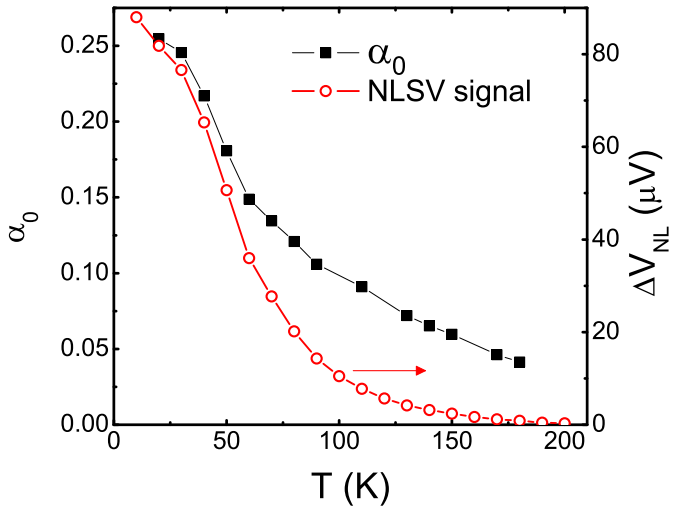

Figure 1.24: (Q62-1) Temperature dependence of the current spin polarization at the injector (black squares). Also shown is the temperature dependence of the NLSV signal (open circles).

temperatures, while phonon scattering takes over at higher temperatures. We expect a crossover between the large τ_s due to impurity scattering to the low τ_s from phonon scattering as the temperature is raised past 120 K. This would explain the much larger drop in the observed τ_s in Fig. 1.23(c) at high temperatures than that calculated assuming a single scattering mechanism at all temperatures.

Quantitatively there is a large discrepancy between the measured and calculated spin lifetimes. Optical measurements of the spin lifetime in similarly doped n-GaAs also produced significantly larger spin lifetimes than that we have measured. The extracted τ_s at 10 K, as shown in Fig. 1.23(c), is 11 ns. This is an order of magnitude lower than $\tau_s \sim 100$ ns found in Refs. [7, 59]. These optical orientation measurements employed modulation of the polarization to minimize

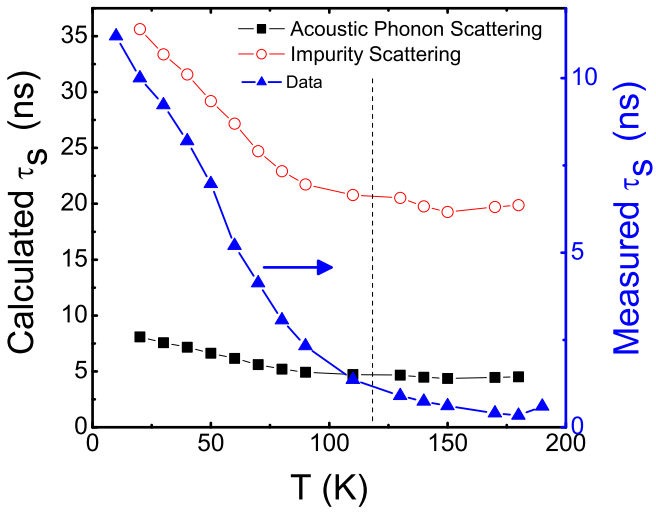

Figure 1.25: Spin lifetime τ_s. Calculated values for Dyakonov-Perel (DP) relaxation due to impurity and phonon scattering are shown as open circles and solid squares respectively. τ_s obtained from fitting measured Hanle curves.

hyperfine effects.[50, 59] Previous electrical measurements of Hanle curves in the 3T configuration produced $\tau_s \approx 45$ ns.[38] The authors pointed out, however, that hyperfine effects were present in their experiment and not accounted for in the determination of τ_s. The extracted τ_s were therefore not the intrinsic value. Furis *et al.* measured similarly high $\tau_s \approx 80$ ns at 10 K in 5×10^{16} cm^{-3} n-GaAs, but observed a sharp decrease to $\tau_s \approx 20$ ns when an electric field is applied above the donor impact ionization threshold of $E_c \approx 10$ V/cm.[50] Below E_c, at low temperatures, electrons are largely bound to their donor sites. The relaxation times of these donor bound electrons are not effected by the D'yakonov-Perel'(DP) mechanism of spin relaxation, and τ_s is therefore a few hundred nanoseconds.[59] Above E_c, free electrons have sufficient energy to excite electrons into the conduction

band by impact ionization of donors. These free electrons are then subject to DP relaxation, resulting in the observed 'collapse' in τ_s. Note however, that the spin exchange rate as calculated in Sec. 2.1.2 is sufficiently fast to equilibrate the localized and conduction electron spin configurations.[88] The measured τ_s is therefore the mean lifetime of both populations.

Fig. 1.26 shows the 3T and NL Hanle curves measured at 10 K. All the solid lines were calculated with $\tau_s = 11$ ns and $D = 1.8$ μm^2/ns. The electric field in the GaAs channel is $\approx$ 1V/cm for $I = -0.1$ mA and 20V/cm for $I = -2$ mA. We do not observe a significant change in τ_s as the electric field varies from below to above the impact ionization threshold. Additionally, τ_s determined in the NL configuration should be unaffected by the electric field, which is nominally zero between the injector and detector.

The discrepancy between τ_s measured electrically in a Fe/GaAs heterostructure and that measured optically is not well understood. In general, electrical measurements of the spin lifetime in *n*-GaAs devices have been significantly smaller than the the spin lifetimes obtained through optical measurements.[39, 42–44] A noteworthy distinction between the two measurements is the presence of the highly doped layer between the bulk GaAs channel and Fe contacts, which forms a shallow quantum well at the interface, as shown in Fig 1.8(b). As we discussed previously Tran *et al.*[41] had found that localized states at the interface can appreciably change the measured spin lifetime. The effective lifetime they measured is determined by a combination of the bulk GaAs spin lifetime, the localized state spin lifetime, and the escape time from the localized states into the GaAs channel.

Fig. 1.23(d) shows the spin diffusion length λ as a function of temperature. A

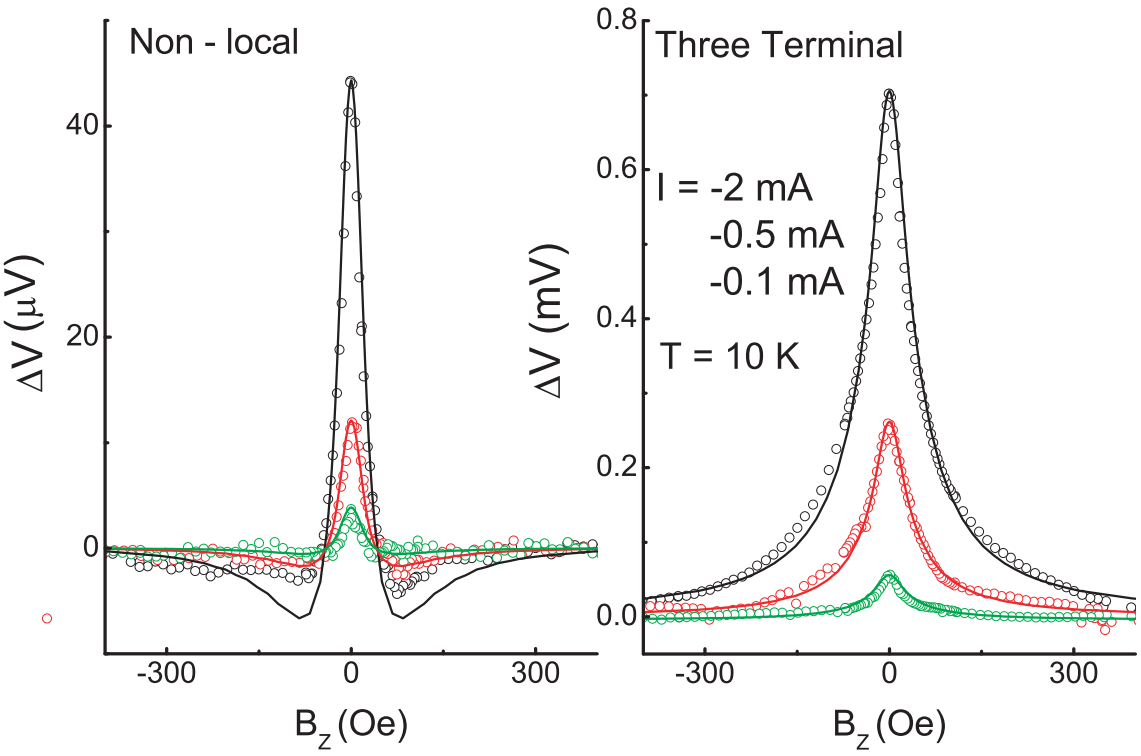

Figure 1.26: (Q62-1) Non-local (right panel) and three terminal (left panel) Hanle curves at various biases. Data are open circles. Solid lines are calculated curves as described in the text. The injector and NL detector are 5×80 μm^2 and 5×50 μm^2 with a 8 μm center-to-center gap.

distinct peak in λ is observed at approximately 60 K. This is due to the competition between τ_s and D, which have opposite temperature dependencies.

Another interesting aspect of the temperature dependent data is the roll over in the 3T signal at low temperatures. Fig. 1.23(b) compares the measured 3T signal to the calculated P_{3T} estimated from the NL measurements. Unlike the the NL signal which continues to increase with decreasing temperature, the 3T signal saturates at low temperatures. This is seen more clearly in Fig. 1.27 where the temperature dependence of the 3T signal is plotted for various injector current bias densities. In these measurements, the bias current is applied on either side of the injector to prevent spin diffusion away from the contact. As a result, the spin signal is extremely large ($>$ 2 mV). The saturation of the signal at low temperatures is clearly observed for the two lowest bias currents, setting in at approximately 40 K. For the case of $j = 1.3$ kA/cm^2, the 3T signal saturates only at the lowest temperature ($\approx$ 10 K), while for the highest applied bias the signal continues to increase at low temperatures.

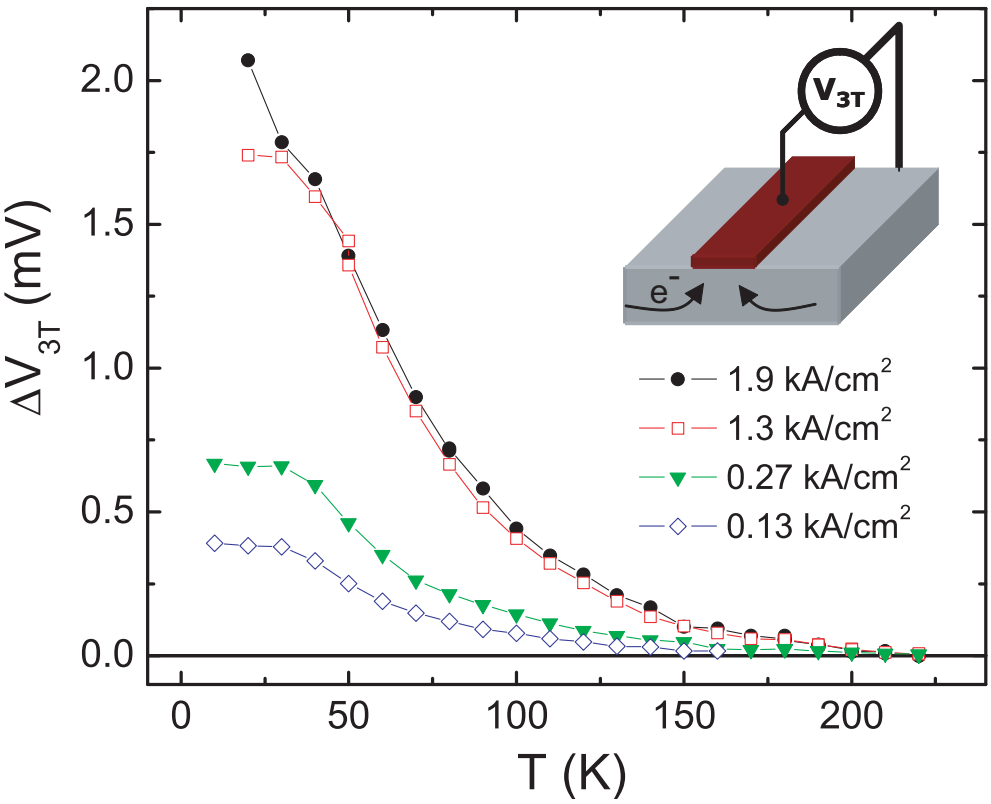

Figure 1.27: (Q62-1) Temperature dependence of the 3T signal for various injector bias current densities. The injector is 5×80 μm^2.

1.8 Conclusion

In this chapter we have introduced a basic theoretical framework to understand spin injection, transport, and detection in ferromagnet/semiconductor devices. We have demonstrated successful spin injection, transport, and detection in Fe/GaAs heterostructures. Measurements in three different configurations: non-local, three terminal, and detector bias, were performed. Hanle measurements in the 3T and non-local configuration, in combination with numerical simulations, allowed us

to determine the spin lifetime τ_s in the GaAs channel. Analysis of detector bias measurements, together with non-local measurements, resulted in a direct determination of the tunneling spin polarization η' for the Fe/GaAs Schottky tunnel barrier as a function of applied bias. Successful fitting of measured Hanle curves indicates a strong understanding of the spin transport in our devices. There are, nevertheless, a number of open questions. A microscopic theory of the bias dependence of η' particularly in the large forward bias regime where we have observed a stark variation is not available. Previous work has centered on understanding the sign change observed at low biases. The magnitude of the 3T signal at high biases and low temperatures is also not well understood.

Chapter 2

Hyperfine Effects in Fe/GaAs Heterostructures

In the previous chapter we were primarily concerned with the polarization of electron spins. We will now consider the nuclear spin polarization and its effects on electron spin dynamics.

2.1 Nuclear Polarization

Consider an assemble of identical nuclei, each associated with an angular momentum (nuclear spin) $\hbar\mathbf{I}$ and a vector magnetic dipole moment (magnetic moment) $\boldsymbol{\mu}_n = g_n\mu_B\mathbf{I}$, where g_n is the nuclear g-factor. The usual way to achieve nuclear spin polarization is to apply an external magnetic field B. The Zeeman interaction $H = -\boldsymbol{\mu}_n \cdot B$ establishes $2I + 1$ energy levels with $E_m = -g_n\mu_B mB$. The quantum number $m = \langle I_z \rangle$ parameterizes each energy level (we have picked the

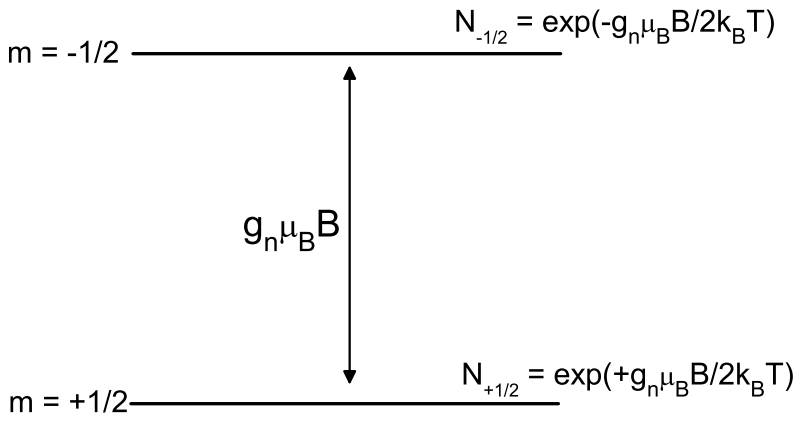

Figure 2.1: Energy levels of a population of $I = 1/2$ nuclei in magnetic field B and temperature T.

quantization axes and magnetic field to be in the z direction). In thermal equilibrium, the number of nuclei in a particular energy level is simply given by the Boltzmann factor $N_m = \exp(E_m/k_BT)$ where T is the temperature.

Fig. 2.1 shows an example of a population of $I = 1/2$ nuclei. Two energy levels, are created by the applied magnetic field, and the population of each level is given by $N_{+1/2}$ and $N_{-1/2}$. Clearly the population of up spins ($m = +1/2$) is larger than the population of down spins ($m = -1/2$). We can therefore define the nuclear spin polarization as

$$P_n = \frac{N_{+1/2} - N_{-1/2}}{N_{+1/2} + N_{-1/2}}. \tag{2.1}$$

Taking $\mu_B = .927 \times 10^{-20}$ erg/Oe, we find that

$$P_n = \tanh\left(\frac{g_n\mu_B B}{2k_BT}\right) \approx 10^{-3}\frac{B}{T}\left[\frac{Tesla}{Kelvin}\right]. \tag{2.2}$$

In order to obtain an appreciable nuclear polarization ($\sim 1\%$) by this method

would require fields of about 10 T at 1 K (an extremely large field at low temperatures). In the case of a system with arbitrary I, ($I = 3/2$ in GaAs), the polarization is given by

$$P_n = \frac{1}{I}\frac{\sum_m mN_m}{\sum_m N_m}. \tag{2.3}$$

We can see clearly that the polarization is the proportional to $\langle I_z \rangle / I$.

An alternative method of creating nuclear polarization is to locate the nuclei in a paramagnetic ion, thus making use of the hyperfine interaction ($\propto \mathbf{I} \cdot \mathbf{S}$), which has an effective field of 10 T to 100 T.[77] Electrons, which have a nuclear magnetic moment three orders of magnitude larger than that of nuclei, can be polarized with significantly smaller fields ($\sim$ 1 T/K), which in turn polarize the nuclei through the hyperfine interaction.

2.1.1 Dynamic Nuclear Polarization

The methods described in Sec. 2.1 are static thermal equilibrium methods. Even with the enhancement of local fields from the hyperfine interaction, a large field still has to be applied to polarize the electron spins. In 1953, Overhauser suggested that the saturation of microwave spin resonance of conduction electrons in a metal, could lead to polarization of the nuclei.[78] This method is known as dynamic nuclear polarization, DNP. In this method, spin pumping with a microwave field of a particular frequency induces transition between energy levels of the combined electron-nuclear spin system. Transitions that involve simultaneous flipping of electron and nuclear spins, directly by the applied microwave field, and indirectly through relaxation processes, yields a dynamic equilibrium (as opposed to thermal equilibrium) with enhanced nuclear polarization.

An alternate way of inducing DNP in semiconductors is to establish a non-equilibrium electron spin polarization through spin injection. The polarized electrons then undergo 'flip-flop' interactions with the nuclei in which the electrons and nuclei exchange spin directions. This effect is due to fluctuations of the electronic field.[79] If electron spin polarization is continually injected, this hyperfine interaction will result in a net nuclear polarization. As mentioned previously, the first experiments on electron spin injection into semiconductors were performed using inter-band optical pumping by absorption of circularly polarized light.[4]

The hyperfine coupling in semiconductors for s-type electrons is given by the contact Fermi interaction[6]

$$H = \frac{2}{3}\mu_0 g_0 \mu_B \gamma_n \hbar |\psi(\mathbf{R})|^2 \mathbf{I} \cdot \mathbf{S}, \tag{2.4}$$

where $\psi(\mathbf{R})$ is the electronic wave function and $\mathbf{R}$ is the distance of the electron from the nucleus. g_0 is the free electron g-factor, and γ_n is the nuclear gyromagnetic ratio. From Eq. 2.4 we can define an effective hyperfine electronic magnetic field B_e acting on a particular nucleus i at position $\mathbf{R_i}$:

$$\mathbf{B}_e^i = -\frac{2\mu_0}{3}\hbar\gamma_e \sum_q \mathbf{S}_q |\psi_q(\mathbf{R}_i)|^2, \tag{2.5}$$

where the sum is over all electronic states q, and γ_e is the electron gyromagnetic ratio.

Analogously, an orbital state ψ_q of effective g-factor $g^\star$ experiences an effective nuclear hyperfine field

$$\mathbf{B}_n^q = \frac{2\mu_0}{3}\frac{g_0}{g^\star}\hbar \sum_i \gamma_n^i \mathbf{I}_i |\psi_q(\mathbf{R}_i)|^2, \tag{2.6}$$

where the sum is over all nuclear sites i. Note that although $\gamma_n \ll \gamma_e$, for a semiconductor the number of nuclei, N_n is much larger than the number of conduction band electrons N_e, such that $N_n/N_e \gg \gamma_e/\gamma_n$ and $B_N \gg B_e$.

In GaAs, there are three types of nuclei, all of spin 3/2: ^{69}Ga, ^{71}Ga, and ^{75}As. As seen from Eq. 2.4 the strength of the hyperfine interaction is dependent on the position of the electrons relative to the nucleus. The interaction is therefore strongest for localized s-type electrons, whose wave-functions are densest at the donor center. In GaAs, the effective donor electron Bohr radius is $a_0^* \approx 100$ Å, which covers many lattice sites. An electron localized on a donor, will therefore polarize many nuclei within the envelop of its wave-function.

If we consider state q at the bottom of the conduction band, the electronic orbital wave function is[6]

$$\psi_q(\mathbf{R}) = F_q(\mathbf{R}) u_0'(\mathbf{R}), \tag{2.7}$$

where $F_q(\mathbf{R})$ is an envelope wave function and $u_0'(\mathbf{R})$ is the periodic Bloch function. $u_0'(\mathbf{R})$ has different values on anion and cation sites. The electronic density given by $d = |u_0'(\mathbf{R})|^2$ for each nuclear species in GaAs calculated in Ref.[81] is

$$\begin{aligned} d(^{75}As) &\approx 9.8 \times 10^{25}\ cm^{-3}, \\ d(^{69}Ga) = d(^{71}Ga) &\approx 5.8 \times 10^{25}\ cm^{-3}. \end{aligned} \tag{2.8}$$

The degree of localization is determined by the envelope function $F_q(\mathbf{R})$. For fully delocalized electrons, $F_q(\mathbf{R}) = (\Omega_c/V)^{1/2}$ everywhere inside the crystal, where V and Ω_c are the sample and cell volumes respectively. For a donor state on the other hand,

$$F_q(\mathbf{R}) = \left(\frac{\Omega_c}{\pi a_0^{*3}}\right)^{1/2} e^{-r/a_0^{*3}}. \tag{2.9}$$

Note that the envelope functions are normalized such that

$$\int |F_q(R)|^2 d^3r = \Omega_c. \tag{2.10}$$

Paget *et al.*[81] have calculated the electronic field B_e experienced by nuclei due to polarized electrons. Taking Eq. 2.5 for a single electron they obtained

$$\mathbf{B}_e^{\alpha}(R) = \Gamma b_e^{\alpha} \mathbf{S} e^{-2R/a_0^*}, \tag{2.11}$$

where α indexes the nuclear species, and

$$b_e^{\alpha} = -\frac{2}{3}\frac{\Omega_c}{\pi a_0^{*3}} \mu_0 g_o \mu_B d^{\alpha}. \tag{2.12}$$

Γ is the fraction of the time the donor is occupied by the electron. Since the electronic density is different for the Ga and As nuclei, the values of b_e^{α} in GaAs are[81]

$$\begin{aligned} b_e^{(^{75}As)} &\approx -220\ Oe, \\ b_e^{(^{69}Ga)} = b_e^{(^{71}Ga)} &\approx -130\ Oe. \end{aligned} \tag{2.13}$$

Eq. 2.4 can be rewritten as

$$H = \frac{2}{3}\mu_0 g_0 \mu_B \hbar \sum_i \gamma_n^i |\psi(\mathbf{R_i})|^2 \left(I_z^i S_z^i + \frac{I_+^i S_- + I_-^i S_+}{2} \right), \tag{2.14}$$

where $I_{+(-)}$ and $S_{+(-)}$ are the raising and lowering operators for nuclear and electron spins respectively. The index i represents the nuclear sites. The second term of Eq. 2.14 describes the spin 'flip-flop' interaction which involve the simultaneous spin flip of a nucleus and electron. Under conditions of continuous electron spin injection, this results in dynamic nuclear polarization DNP of the nuclear spins. As seen from Eq. 2.11, DNP is most effective for electrons localized on donor

sites, where $\mathbf{B}_e$ is strongest. The polarization time of nuclei a distance R from an impurity is estimated by[79]

$$\frac{1}{T_{pol}}(R) \approx \Gamma(\gamma_n b_e)^2 \tau_c e^{-4R/a_0^*}, \tag{2.15}$$

where τ_c is the correlation time of the relaxing interaction. Since it is the capture and release of the electron that induces the fluctuating hyperfine interaction, τ_c is of the same order of magnitude as the lifetime of a trapped electron, which ranges from $10^{-9} - 10^{-8}$ s. One therefore finds that $T_{pol} \sim 10^{-2} - 10^{-1}$ s for $\Gamma \sim 1$.

In the mean field approximation the 'flip-flop' term is zero and Eq. 2.14 describes the interaction of an electron with the effective hyperfine field B_n. For a sample with uniformly polarized nuclei and using Eqs. 2.6, 2.7 and 2.8, we get

$$B_n^\alpha = b_n^\alpha \langle I^\alpha \rangle, \tag{2.16}$$

where

$$b_n^\alpha = \frac{2\mu_0}{3}\frac{g_0}{g^*}\hbar \sum_{i \in \alpha} \gamma_i^\alpha \left|\psi_q(r_i)\right|^2. \tag{2.17}$$

The sum is over all nuclear sites of nuclear species α. For GaAs, [81]

$$\begin{aligned} b_n^{(^{75}As)} &\approx -18.4\ kOe, \\ b_n^{(^{69}Ga)} &\approx -9.1\ kOe, \\ b_n^{(^{71}Ga)} &\approx -7.8\ kOe. \end{aligned} \tag{2.18}$$

The different values for each nuclear species are due to differing electronic densities given in Eq. 2.8 and differing nuclear concentrations (^{69}Ga:^{71}Ga $\approx$ 3 : 2). The total hyperfine field experienced by a particular electron is due to the sum of the hyperfine field exerted by all nuclei enveloped by the electron wave function. As

a result, although only localized electrons are responsible for DNP of nuclei, the hyperfine field is also exerted on delocalized electrons, due to the large number of nuclei that overlap the electron's extended form factors.

However, the number of donors is actually quite small compared to the total number of nuclei in the bulk. Our experiments are performed in n-GaAs with donor concentration 5×10^{16} cm^{-3}. This yields an average inter impurity distance of ≈ 250 $\mathring{A}$. In GaAs, $a_0^* \approx 100\mathring{A}$. Nuclei within the Bohr radius are also effectively polarized. Additionally, the nuclear spin diffusion constant was observed to be $\approx 10^{-13}$ cm^2/s[82], which yields a nuclear spin diffusion length of ≈ 140 $\mathring{A}$. Spin diffusion will therefore polarize the bulk nuclei as well. The total hyperfine field B_n acting on conduction electrons can therefore be quite large.

2.1.2 Spin Exchange

As we discussed in the previous section, the form of the hyperfine interaction would result in a different hyperfine field acting on delocalized and localized electrons. It has, however, been shown that the NMR signal of localized and delocalized electrons in GaAs are of the same magnitude.[88] This unexpected result is resolved if there is an averaging mechanism mixing the two electron spin populations.

When the spins of the localized and delocalized electronic states are antiparallel, the Coulomb interaction may result in a mutual flip-flop interaction.[89] If the spin flip-flop scattering rate between the two electronic states is larger than the electron spin relaxation rate, the two states will reach a mean equilibrium state. We can therefore describe the hyperfine field acting on the whole system in terms of a mean between the large field on the localized states and the weak field on the

delocalized states.

The spin exchange scattering cross section σ_e between a free electron and an occupied donor was calculated by Paget:[88]

$$\sigma_e = \frac{1}{4}\Big[\sigma_T + \sigma_S + 2(\sigma_T\sigma_S)^{1/2}\cos(\delta_{T0} - \delta_{S0})\Big], \tag{2.19}$$

where

$$\begin{aligned} \sigma_T &= \frac{4\pi}{k^2}\sin^2\delta_{T0} \\ &\text{and} \\ \sigma_S &= \frac{4\pi}{k^2}\sin^2\delta_{S0} \end{aligned} \tag{2.20}$$

are the scattering cross sections of the triplet and singlet two electron states. δ_{S0} and δ_{T0} are the zero-order phase shifts for the singlet and triplet states for the case of scattering of free electrons by hydrogen atoms. [90] k is the momentum of the delocalized electron. Taking $k = k_T$, where k_T is the thermal momentum of the electron for $T = 10$ K,

$$\sigma_e \approx 10^{-11}\ cm^2, \tag{2.21}$$

we can write the rate equation of the mean spin for the free (S_f) and localized (S_l) electrons as

$$\begin{aligned} \frac{\partial S_f}{\partial t} &= -\frac{n_l}{n_l + n_f}\frac{1}{\tau_e}(S_f - S_l), \\ \frac{\partial S_l}{\partial t} &= -\frac{n_f}{n_l + n_f}\frac{1}{\tau_e}(S_l - S_f), \end{aligned} \tag{2.22}$$

where n_l and n_f are the localized and free electron density respectively. The spin of localized and free states will equilibrate at a rate given by

$$\frac{1}{\tau_e} = (n_f + n_l)\sigma_e v, \tag{2.23}$$

where v is the thermal velocity ($v \sim 10^7$ cm/s in GaAs at 10 K). Taking the a typical donor concentration for our samples $n = n_f + n_l = 10^{16}$ cm^{-3} we get a spin exchange time $\tau_e \approx 1$ ps. This is 3 to 4 orders of magnitude smaller than the typical electron spin lifetime of free electrons in GaAs ($\tau_s \approx 10$ ns at 10 K in n-GaAs), demonstrating that spin exchange is effective in equilibrating the free and localized spin populations.

The resultant dynamics of localized electrons under the influence of a strong nuclear field will therefore be averaged with that of the free electrons, which experience a weaker nuclear field.

2.1.3 Steady State Nuclear Field

We expect that in the steady state, the average nuclear spin polarization transverse to the effective magnetic field acting on the nuclei $\mathbf{B}_{eff}$ is negligible. The reason is that the nuclear gyromagnetic ratio in GaAs is ~ 1 kHz/Oe, whereas the nuclear lifetime $T_1 \sim 10$ s. The transverse component of the average nuclear polarization is then fully de-phased in the time scale of our experiments (~ 100 ms). This is just the Hanle effect described previously for electron spin polarization. The difference is that even in modest transverse fields, the nuclear polarization can precess many times before decaying. The nuclear Hanle FWHM is $\sim 10^{-4}$ Oe. As a result, the average steady state nuclear polarization is always along the direction of $\mathbf{B}_{eff}$. Note however, that the total field acting on the nuclei includes the applied magnetic field $\mathbf{B}$ and the electronic field (or Knight field) $b_e\mathbf{S}$, such that $\mathbf{B}_{eff} = \mathbf{B} + b_e\mathbf{S}$. Let us assume that $\mathbf{B}_{eff}$ is along the z direction. We can determine the steady state nuclear polarization by writing down the following rate

equation[77, 91],

$$\frac{d\langle I_z\rangle}{dt} = -\frac{1}{T_{pol}}(\langle I_z\rangle - k\langle S_z\rangle) - \frac{1}{T_1}\langle I_z\rangle, \tag{2.24}$$

where $k = f\left[I(I+1)\right]/\left[S(S+1)\right]$ and f is the leakage factor. T_{pol} is taken as the average of the nuclear polarization time due to the 'flip-flop' hyperfine interaction with the electrons defined in Eq. 2.15. T_1 is the nuclear spin relaxation time due to non-hyperfine interactions. For nuclear relaxation due to fluctuations of the local dipole-dipole field, $T_1^{-1} \propto (B_L/B)^2$.[91] The nuclear spin relaxation rate is suppressed by an applied field because the Zeeman splitting of the nuclear spin sub-levels increases the required transition energy.[86, 91] Eq. 2.24 can be solved in steady state for $\langle \mathbf{I}\rangle = \langle I_z\rangle\hat{z}$:[86]

$$\langle \mathbf{I}\rangle = k\frac{\langle S_z\rangle\hat{z}}{1 + T_{pol}/T_1}. \tag{2.25}$$

If we generalize to an effective magnetic field pointing in an arbitrary direction, we obtain

$$\begin{aligned}\langle \mathbf{I}\rangle &= k\frac{(\mathbf{B}_{eff}\cdot\mathbf{S})\mathbf{B}_{eff}}{(\mathbf{B}_{eff})^2 + \frac{T_{pol}}{T_1}B_{eff}^2} \\ &= k\frac{(\mathbf{B}_{eff}\cdot\mathbf{S})\mathbf{B}_{eff}}{(\mathbf{B}_{eff})^2 + \xi B_L^2}.\end{aligned} \tag{2.26}$$

where $\vec{S}$ is the average electron spin ($|\vec{S}| = 1/2$ for $P = 100\%$), B_L is the local dipolar field experienced by the nuclei, and

$$\xi = \frac{T_{pol}}{T_1}\left(\frac{B_{eff}}{B_L}\right)^2, \tag{2.27}$$

parameterizes the assisting processes which allow energy to be conserved in mutual spin flips between electrons and nuclei. The total hyperfine field is

$$\boldsymbol{B}_n = \sum_\alpha B_n^\alpha = \sum_\alpha b_n^\alpha \langle \boldsymbol{I}^\alpha\rangle. \tag{2.28}$$

We therefore have the following expression for the steady state average nuclear field[6, 81, 86]

$$\mathbf{B_n} = b_n \frac{(\mathbf{B}_{eff}) \cdot \mathbf{S}}{(\mathbf{B}_{eff})^2 + \xi B_L^2} (\mathbf{B}_{eff}) = b_n \frac{(\mathbf{B} + b_e \mathbf{S}) \cdot \mathbf{S}}{(\mathbf{B} + b_e \mathbf{S})^2 + \xi B_L^2} (\mathbf{B} + b_e \mathbf{S}), \tag{2.29}$$

where b_n and b_e are effective nuclear field coefficients appropriately averaged over all the values of the different nuclei species in Eq. 2.18 and 2.13. Note that the leakage factor, f and fraction of donor occupancy time Γ will suppress b_n and b_e from their ideal values:

$$\begin{aligned} b_n &= f b_n', \\ b_e &= \Gamma b_e', \end{aligned} \tag{2.30}$$

where the calculated ideal values for GaAs are given by[81]

$$\begin{aligned} b_n' &= -170 \ kOe, \\ b_e' &= -170 \ Oe. \end{aligned} \tag{2.31}$$

The value of b_e' here is merely an average of the b_e values in Eq. 2.13. Both Ga and As nuclei have $I = 3/2$ and $S = 1/2$ for electrons, so

$$b_n' = [I(I+1)] \,/\, [S(S+1)] \sum_\alpha b_n^\alpha = -170 \text{ kOe}, \tag{2.32}$$

where b_n^α are given in Eq. 2.18.

As stated previously, nuclear spin relaxation through the fluctuating part of the hyperfine electronic field is responsible for DNP. This relaxation rate is given by $1/T_{pol}$ as in Eq. 2.15. However, nuclear spins can also relax through other means, particularly by fluctuating local dipole-dipole fields from neighboring nuclei, paramagnetic impurities or quadrapolar relaxation.[93] The non-hyperfine

nuclear relaxation rate is $1/T_1$. The leakage factor is the ratio of the hyperfine interaction rate to the total relaxation rate $T_{1,tot}^{-1} = T_{pol}^{-1} + T_1^{-1}$:

$$f = \frac{T_{pol}^{-1}}{T_{1,tot}^{-1}} = \frac{T_1}{T_1 + T_{pol}}. \tag{2.33}$$

We see that the non-hyperfine relaxation mechanisms tends to reduce the effectiveness of DNP.

From Eq. 2.29, $\boldsymbol{B}_N$ points either parallel or antiparallel (depending on the sign of $\mathbf{B}_{eff} \cdot \mathbf{S}$), to the total field $\mathbf{B}_{eff}$. When the applied field $\mathbf{B}$ is much larger than $b_e\mathbf{S}$ (typically $\sim$ 10 Oe) $\mathbf{B}_n$ is aligned with the applied field. However, when $\mathbf{B}$ is approximately equal or less than $b_e\mathbf{S}$, $\mathbf{B}_n$ rotates into the direction of $\mathbf{S}$. Due to the large nuclear field coefficient b_n, the changes in the direction of $\mathbf{B}_n$ at low applied fields can result in rather complicated electron spin dynamics.[81, 87]

2.2 Low Field Electron-Nuclear Spin Dynamics

Nuclear field effects were apparent in the earliest electrical measurements of electron spin polarization in Fe/GaAs heterostructures performed in our group.[38] Particularly, Hanle curves at low temperatures were observed to exhibit anomalously narrow line-widths at low fields, and non-local spin valve data showed cusps close to zero field.[39] Both were attributed to rapid de-phasing of electron spins by a large transverse hyperfine field $B_{n,z}$.

Fig. 2.3(a) shows a non-local spin valve (NLSV) measurement at T = 60 K under forward bias. In anticipation of the existence of large hyperfine fields, the field sweep was taken very slowly, $\approx$ 0.025 Oe/s at low fields, to ensure the nuclear spins are in steady state ($T_1 \sim$ 30 s at 60 K). The typical small field

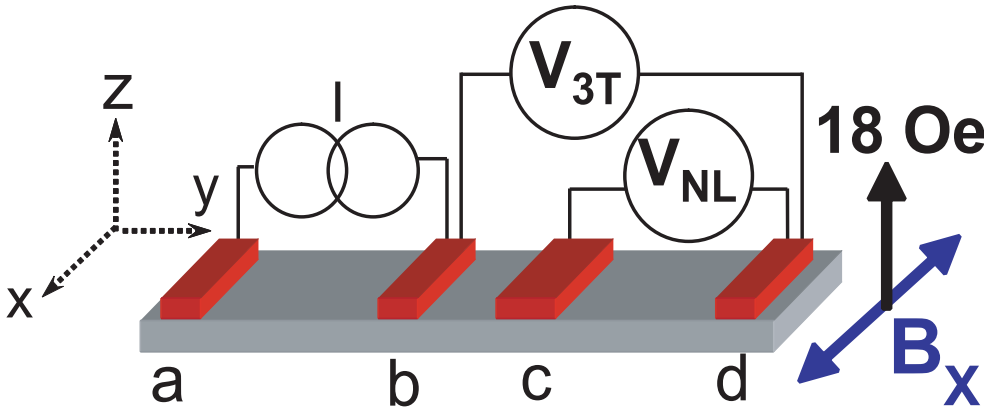

Figure 2.2: Schematic of the lateral spin transport device. I establishes a forward bias at contact b. The spin polarization in the GaAs channel at contact b or c is determined by measuring the 3-terminal voltage V_{3T} or non-local voltage V_{NL} relative to reference contact d (drawing not to scale).

spin depolarization observed previously in NLSV data measured with a fast field sweep[38] is not observed. The zero field depolarization feature is due to the non-steady state hyperfine field that builds up at large B applied with a slight misalignment from the x axes.

Fig. 2.3(b) (and (c) for a low field closeup) shows the same NLSV data measured in approximate steady state, with an applied constant transverse field $B_z = 18$ Oe to induce a non-trivial B_n at small fields. A schematic of the measurement configuration is shown in Fig. 2.2. The electron spin initially undergoes depolarization. Then, at a particular field indicated by $B_x = B_R$ the spin repolarizes before depolarizing once again. B_R is negative for B_x swept from large positive fields and vice versa. The magnetization of the injection contact, and thus the injected spins, for curves swept from opposite fields are in opposite directions. The depolarization of S at small B_x can be understood by invoking a

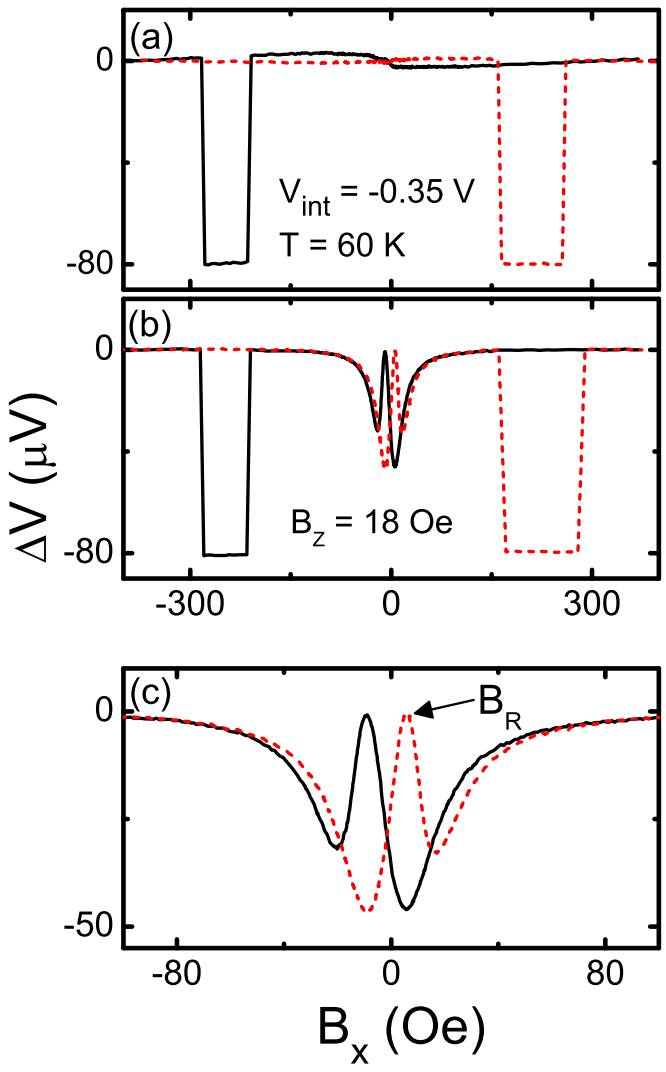

Figure 2.3: (Q59-6) (a) Non-local spin valve measurement at T = 60 K with magnetic field swept along the Fe [110] axes (x-direction) and no transverse field, $B_z = 0$ Oe. (b) Non-local spin valve with transverse field $B_z = 18$ Oe. (c) Low field close up of (b)

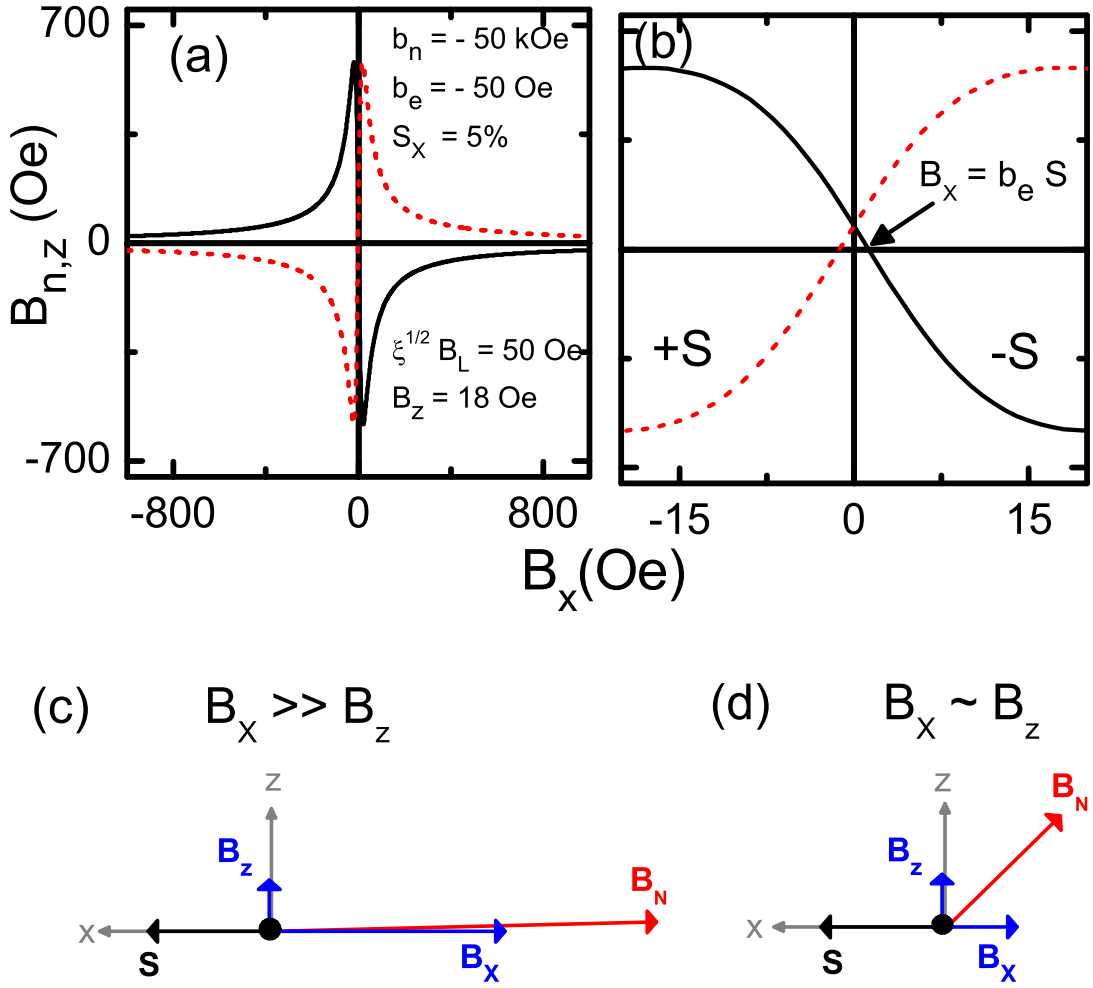

Figure 2.4: (a) Hyperfine field $B_{n,z}$ in the transverse z direction calculated using Eq. 2.29 with nuclear parameters indicated in the figure as a function of B_x with a constant $B_z = 18$ Oe. The spin polarization is in the x direction and fixed: $\mathbf{S} = S_x = +0.025$ or $-.025$ for the solid and dashed lines respectively (b) Low field region of the calculated $B_{n,z}$. Note that $B_{n,z} = 0$ at opposite signs of B_x for $S_x = \pm 0.025$. Schematics show the direction of the hyperfine nuclear field $\mathbf{B_N}$ for large B_x (c), and for B_x comparable to the transverse field B_z (d).

hyperfine field of the form shown in Eq. 2.29. As seen in Fig. 2.4(a) and (c), for large B_x, B_n points essentially along B_x and is collinear with **S**, which remains polarized. When $B_x \sim B_z$, B_n rotates into the transverse direction, as shown in Fig. 2.4(d), thus de-phasing **S**. However, when $B_x = b_e S$, ($b_e S$, is known as the Knight field), $B_n = 0$, as shown in Fig. 2.4(b). At this field, **S** will re-polarize as shown in Fig. 2.3(b) and (c). When **S** changes sign, the Knight field will change sign, explaining the change in sign of B_R with sweep direction.

In optical orientation experiments, the argument of the previous paragraph has been used to determine b_e by setting $B_R = b_e S$, where S is the known optically generated spin polarization.[81, 87] In our experiment, we can enhance S by increasing the injector bias, as shown by the increase of the NLSV signal in Fig. 2.5(a). It is clear from Fig. 2.5(b), that B_r initially decreases precipitously with increasing forward bias ($V_{inj} < -0.2V$), then increases slightly when $V_{inj} > -0.2V$. This is in direct contradiction of the bias dependence of $V_{\uparrow\uparrow} - V_{\uparrow\downarrow}$, which increases monotonically with increasing forward bias. This anomaly, which precludes a simple identification of the Knight field, is due to the fact that the electron spin polarization at small fields is reduced by precession. This fact, which was ignored in the calculation of $B_{n,z}$ in Fig. 2.4 and in the interpretation of the early optical orientation measurements, has a profound influence on the electron spin dynamics at very low fields.

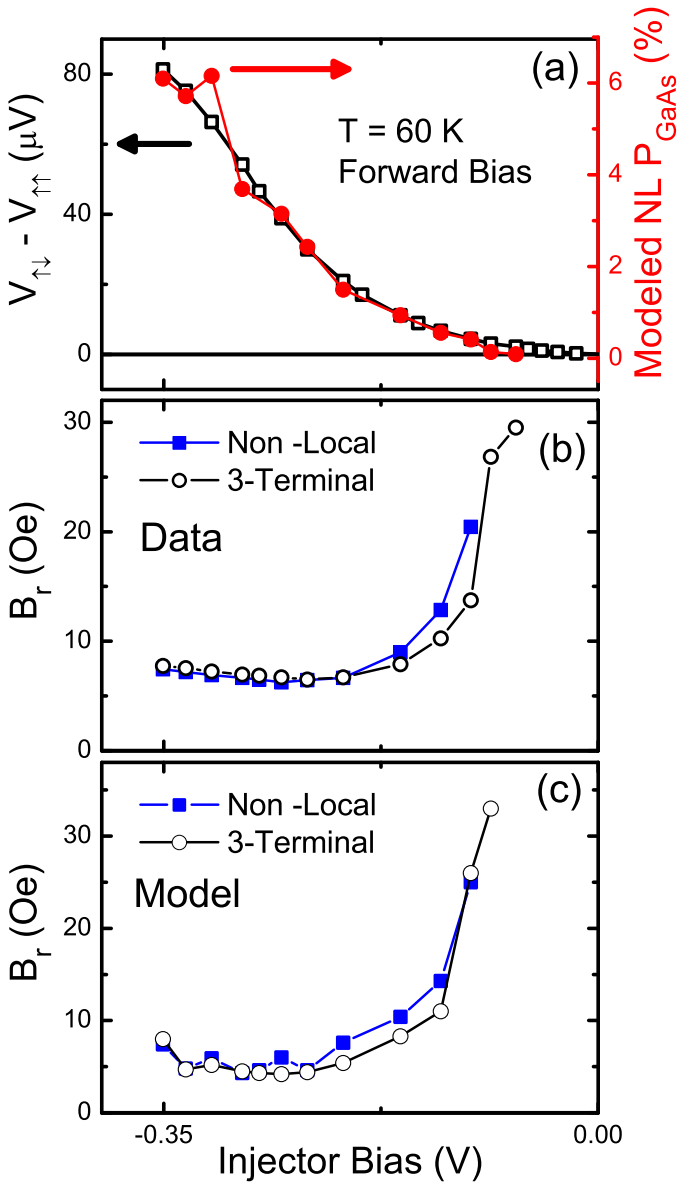

Figure 2.5: (a) Measured non-local spin valve NLSV signal (open black squares, left axes) and modeled spin polarization in the GaAs P (closed red circles, right axes) for different injector forward biases. (b) Measured re-polarization field B_R as a function of injector bias in the three-terminal 3T (closed blue squares) and NL (open black circles) configurations. (c) B_R extracted from the modeling results as a function of injector bias in the 3T (closed blue squares) and NL (open black circles) configurations.

2.2.1 Modeling Electron Spin Dynamics Under the Influence of a Hyperfine Field

In order to address the discrepancy discussed in the previous section and to model the measured electron spin dynamics as a function of applied field, we consider the rate equation of electron spins with drift and diffusion in the y direction

$$\frac{\partial \mathbf{S}}{\partial t} = -v_d \frac{\partial \mathbf{S}}{\partial y} + D\frac{\partial^2 \mathbf{S}}{\partial y^2} - \frac{\mathbf{S}}{\tau_s} - \mathbf{\Omega}_L \times \mathbf{S}, \tag{2.34}$$

where v_d, D, and τ_s are the drift velocity, diffusion constant, and spin lifetime; $\Omega_L = g^* \mu_B \mathbf{B}_{tot}/\hbar$ is the Larmor frequency, $g^* = -0.44$ is the electron g-factor in GaAs, μ_B is the Bohr magneton. In Chapter 1 we only considered precession of $\mathbf{S}$ about the externally applied field. Here we consider $\mathbf{B}_{tot} = \mathbf{B} + \mathbf{B}_n$ where the hyperfine field $\mathbf{B_n}$ defined in Eq. 2.29 is included in the total field. Note that $\mathbf{B}_n$ is a nonlinear function of $\mathbf{S}$, which in turn is nonlinearly dependent on $\mathbf{B}_n$. We therefore have to solve Eq. 3.31 self consistently. To do so, we discretize Eq. 3.31 using the Crank-Nicholson method [60]. A one-dimensional spatial grid and injector/detector cells are identified. A constant spin generation rate $\dot{S}_0$ is introduced in each injector cell at each time step. $\mathbf{S}$ and $\vec{B}_N$ are calculated from Eqs. 2.29 and 3.31 at each position as the calculation is temporally evolved. The calculation is stopped when the $\vec{S}$ has reached a steady state (typically after 50 ns). The NL and 3T signals are determined from the spatial average of the steady state S_x (since the detector is only sensitive to the x spin component) at the detector and injector respectively. To obtain the field dependence, the same calculation is repeated for each magnetic field point. The parameters v_d and D are determined independently from Hall and resistivity measurements as discussed in Chapter 1.

	h_N (kOe)	b_e (Oe)	B_L (Oe)	$\sqrt{\xi}B_L$ (Oe)	τ_s (ns)	D (μm^2/ns)
Experiment	-53	-50	-	40	9	2.5
Ideal [81]	-170	-170	1.45	2.14	-	-

Table 2.1: Experimentally determined nuclear, Knight and local field coefficients and the spin lifetime. Theoretical values are from Ref.[81].

In the simulations, we set $v_d = 0$ outside of the charge current path, i.e. between the injector and detector. $b_n, b_e, \sqrt{\xi}B_L$, and τ_s are obtained from fits of a field sweep at one bias current and are then kept fixed while fitting the data for other bias currents. Only $\dot{S}_0$ varies with bias, but it is kept the same for NL and 3T simulations of the same bias. As indicated by the solid curves in Figs.2.6, Fig. 2.7 and Fig. 2.5(c), the modeling clearly reproduces the measured field dependence and bias dependence of B_R.

From the modeling we determine that $b_n = -53$ kOe and $b_e = -50$ Oe, which are, as expected, smaller than the theoretical ideal values of $b_n' = -170$ kOe and $b_e' = -170$ Oe (calculated by Paget *et al.*[81] for a closed electron-nuclear spin system and in which the donor sites are always occupied by spin-polarized electrons) but larger by a factor of 1.3 to 4 then previously measured values for p-type GaAs (acceptor concentration $n_a \sim 2 \times 10^{18}$ cm^{-3} and compensation $n_d/n_a \sim 0.3$)[81] and Ge-doped GaAs.[87]

The consistency of the fits in Fig. 2.6 and Fig. 2.7 given a single set of parameters allows us to use this approach to measure the spin polarization $P = 2\langle|\vec{S}|\rangle$ averaged over the non-local detector. The results extracted from the modeling, shown in Fig. 2.5(a), are in excellent qualitative agreement with the bias dependence of $V_{\uparrow\uparrow} - V_{\uparrow\downarrow}$. It is extremely important to note that this measurement of

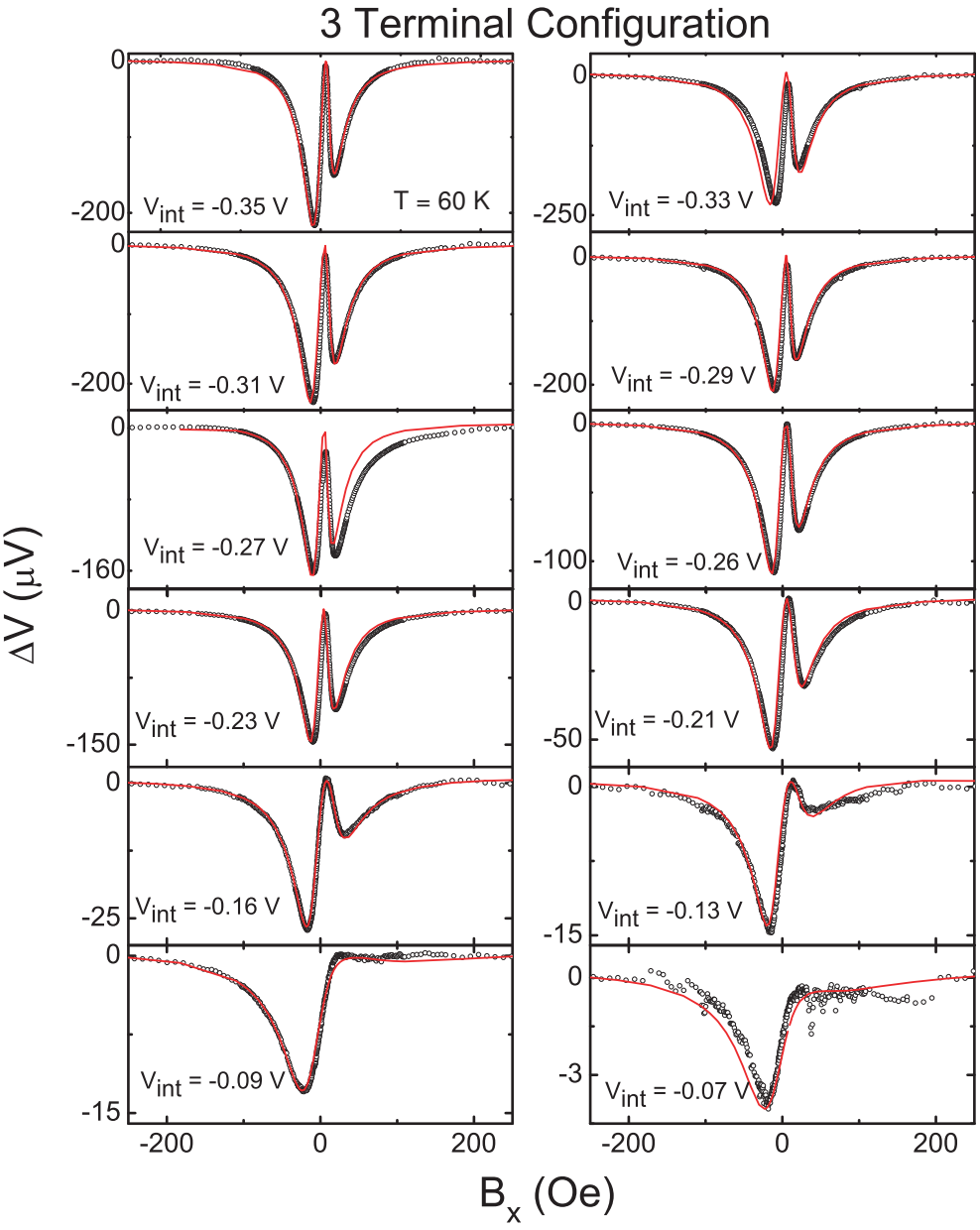

Figure 2.6: (Q59-6) Voltage as a function of applied longitudinal field B_x in the three terminal 3T configuration for various injector biases at $T = 60$ K. A transverse field $B_z = 18$ Oe is also applied. Open circles are data, and solid lines are modeling results as described in the text.

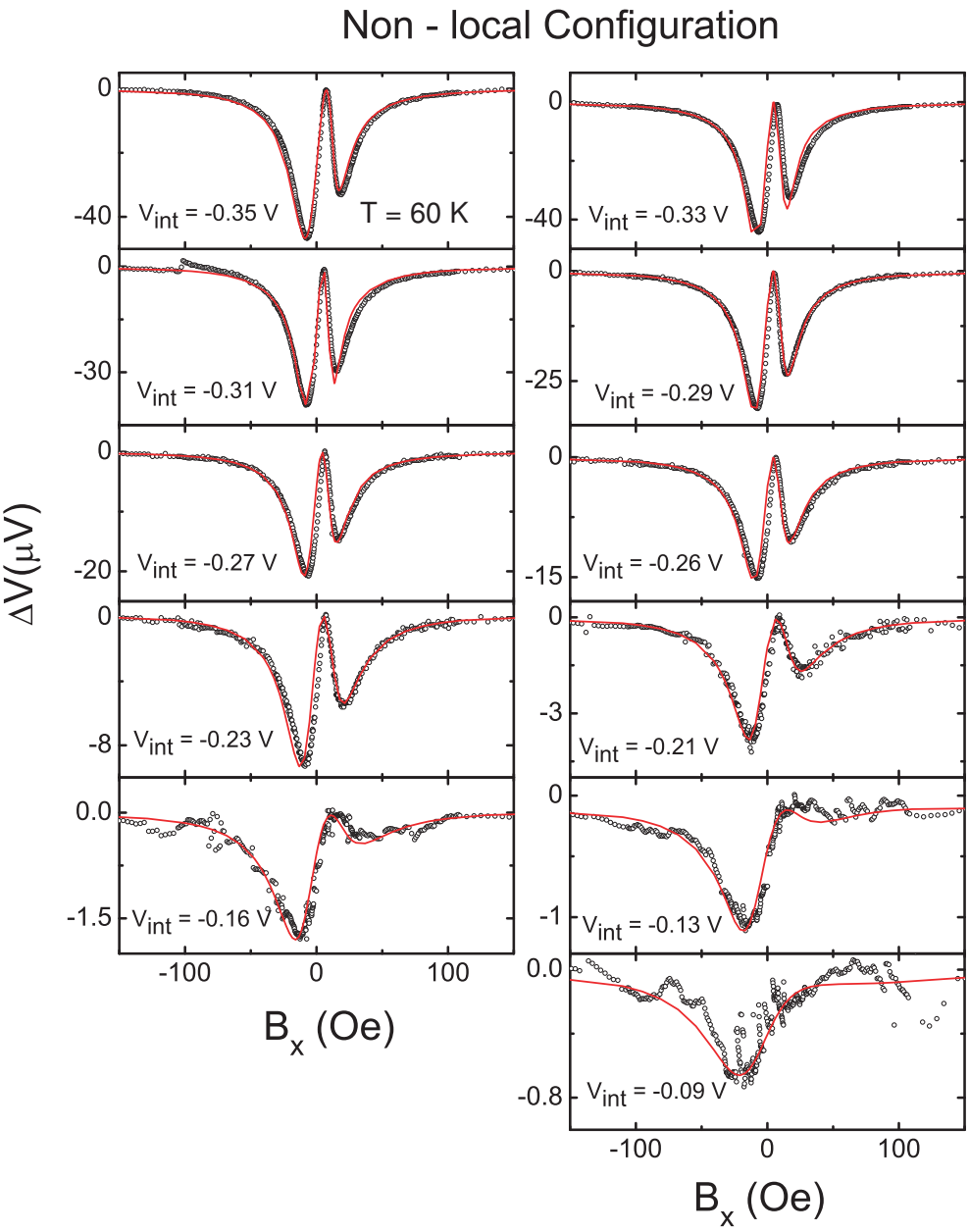

Figure 2.7: (Q59-6) Voltage as a function of applied longitudinal field B_x in the non-local NL configuration for various injector biases at $T = 60$ K. A transverse field $B_z = 18$ Oe is also applied. Open circles are data, and solid lines are modeling results as described in the text.

P, which is based on the Knight field, is independent of any of the usual assumptions underlying spin transport measurements. It is therefore of particular interest to compare, quantitatively, with the polarization as inferred from the non-local voltage using standard arguments discussed in Chapter 1. P can be estimated from

$$V_{\uparrow\uparrow} - V_{\uparrow\downarrow} = \frac{2}{3e}\eta' P E_F, \tag{2.35}$$

where η' is the interface spin transmission efficiency, and E_F is the fermi energy of GaAs, which is assumed to be the that of a Pauli metal with an effective mass $m^* = 0.07m_e$. From the measured $V_{\uparrow\uparrow} - V_{\uparrow\downarrow}$ in Fig. 2.5 we have calculated P (for $\eta' = 0.2$, which is expected based on spin-LED measurements [62] and a measured carrier density of 4.3×10^{16} cm^{-3} at $T = 60$ K) to be between 0.2% and 6% for the injector bias range shown. This is in good agreement with the values obtained from the analysis of the coupled electron-nuclear spin dynamics shown in Fig. 2.5 (a). Among the important implications of this result is that the *magnitude* of the density of states in the semiconductor near the Fe/GaAs interface is not grossly different from that given by the naive Pauli model. This is not obvious *a priori* since one might expect hybridization between the impurity and conduction bands at a doping level above the metal insulator transition. Nevertheless, the successful modeling of the nuclear effects indicates that using the bulk Pauli model as the density of states for GaAs is a reasonable assumption when estimating the electron spin polarization from the detected spin dependent voltage signals.

From the fitting we have performed, we estimate the error in each individual parameter to be about 20%. Although the simultaneous fits from our model presented in Fig. 2.6 and 2.7 are quite successful, we should note that there were

5 free parameters: b_n, b_e, $\sqrt{\xi}B_L$, $\dot{S}_0$, and τ_s. The effect of each on the longitudinal field sweep curves is shown in Fig. 2.8. Decreasing τ_s decreases the relative height of the second depolarization feature. b_e shifts the position of B_R but does not significantly effect the shape of the curve. A decrease in either b_n or $\dot{S}_0$, or an increase in $\sqrt{\xi}B_L$, decreases the relative height of the second depolarization feature, and shifts B_R towards larger fields. It might therefore be argued that a large shift in one of the parameters can be balanced by a opposite shift of another. Without further constraints on the parameters, we cannot rule out such a scenario, although we note that, aside from $\sqrt{\xi}B_L$ the results we obtained are reasonably consistent with theoretical calculations and previous measurements of hyperfine effects in GaAs. As we will show in the next section, we are able to model Hanle and oblique Hanle curves successfully without modifying any of the parameters found in this section, thus further constraining the fitting parameters. Although b_n and $\sqrt{\xi}B_L$ can compensate for each other in the fits of the longitudinal field sweeps, we will show that the high field satellite peak observed in the oblique Hanle curves is insensitive to $\sqrt{\xi}B_L$ but depends linearly on b_n. The b_n determined here reasonably reproduces the position of the high field satellite peak, indicating that the value of $\sqrt{\xi}B_L$ found here is accurate.

Independent measurements of the nuclear and electronic hyperfine field coefficients b_n and b_e can be obtained by determining shifts of the electron or nuclear resonance lines respectively.[88] All electrical nuclear magnetic resonance (NMR) measurements on a Fe/GaAs device have been performed. However, we found that the Knight shift is not resolvable in our measurements due to the large width of the resonance lines, as will be discussed in Sec. 2.5. We are currently pursuing

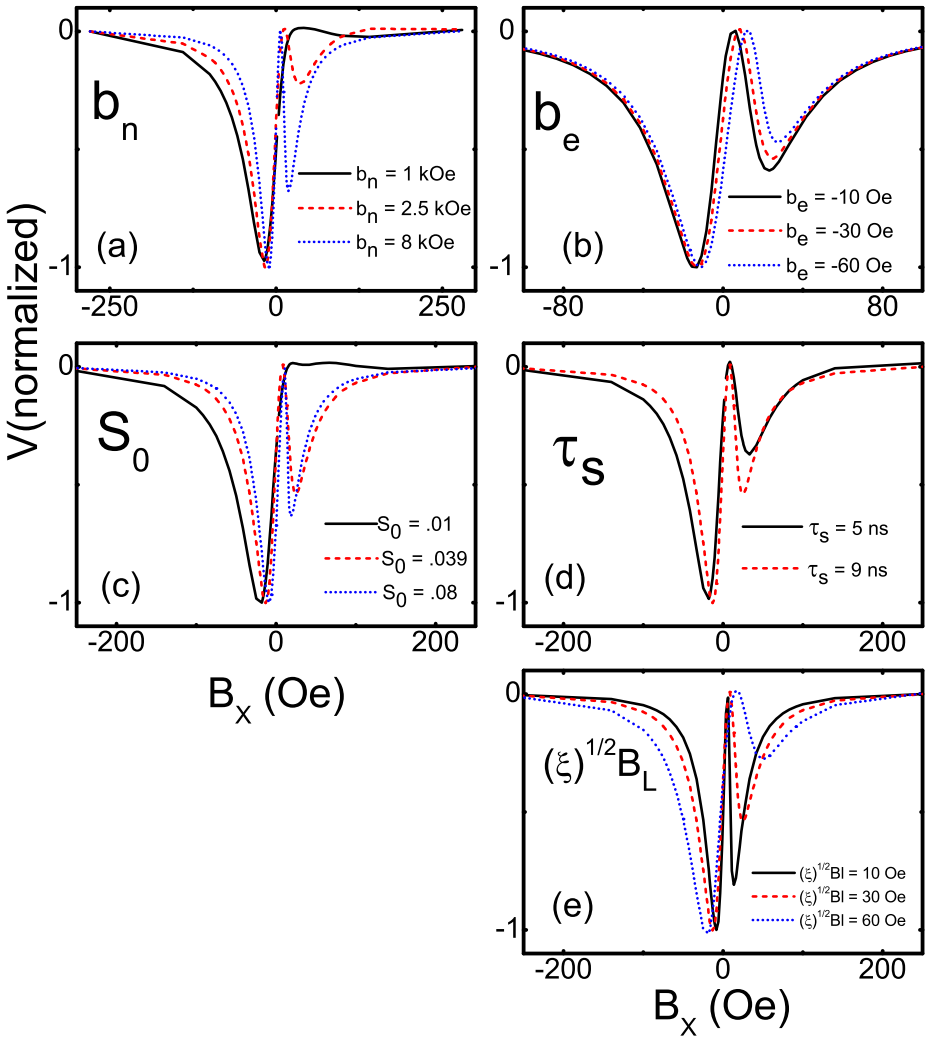

Figure 2.8: Evolution of modeled longitudinal field sweeps with varying fitting parameter values.

electron spin resonance (ESR) signatures in this system as well.

2.3 Hyperfine Effects in the Oblique Hanle Configuration

The extraordinary sensitivity of the electron spin dynamics to hyperfine effects in the Fe/GaAs system was initially observed in the distortion of the Hanle effect, in which electron spin polarization is suppressed by precession in a transverse magnetic field.[38] Fig. 2.9 shows V_{NL} for field sweeps along the z-axis and at a polar angle of 17^o from the z-axis. The salient features of these data are reproduced by the model introduced above with the same parameters used to fit the data of Fig. 2.7 and 2.6 (see Table 2.1). Of particular interest are the narrowing of the Hanle curve in Fig. 2.9(a) and the weak splitting of the zero-field peak shown in the inset of Fig. 2.9(b). Both are due to the effect of the Knight field. In its absence, the Hanle curves in Fig. 2.9(a) and (b) would show the form indicated by the dashed curves. Clearly, an extraction of the spin lifetime τ_s from Hanle curves without consideration of hyperfine fields will result in an overestimation of τ_s. This point was noted in the original electrical measurements in Fe/GaAs heterostructures [38] and later by Awo-Affouda *et al.*[42] The nuclear field elimination procedure discussed in Sec. 2.6 is therefore necessary to extract accurate spin lifetimes at low temperatures.

The two satellite peaks observed in the oblique Hanle curves can be understood as points at which the transverse component of the nuclear field cancels out the applied field, $B_{n,z} = -B_z$, such that the total transverse field is zero, $B_{tot,z} = 0$.

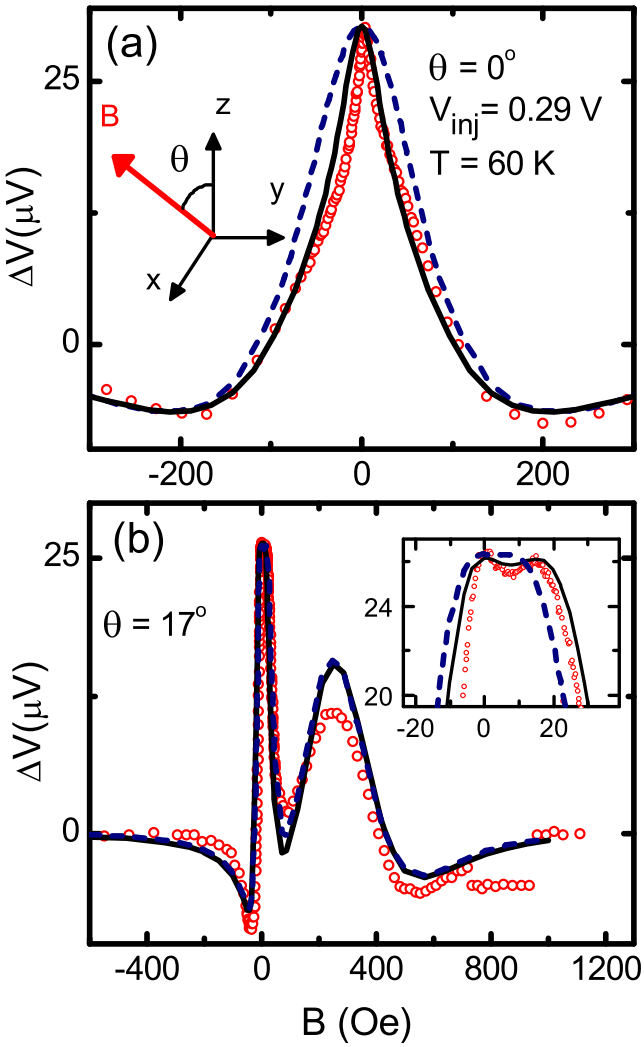

Figure 2.9: (Q59-6) Non-local voltage field dependence: measured curves (open circles)and modeled curves with Knight field (solid line) and without Knight field ($b_e = 0$, dashed line) for magnetic field swept along the z axes (Hanle) (a) and along polar angle $\theta = 17^o$ from the z axes (oblique Hanle) (b). Modeled curves are calculated with the same parameters used to fit data in Fig. 2.7 and 2.6. (b) Inset: closeup of the oblique Hanle curves.

At such points, the electron spins are no longer de-phased, resulting in a peak of the signal. Fig. 2.10 shows the calculated total transverse field using Eq. 2.29 for a fixed $\mathbf{S} = S_x$ in the oblique Hanle geometry. The high field satellite peak at B_2 is due to direct cancelation of the applied field by the hyperfine field, as shown in Fig. 2.10(c). B_2 is most sensitive to b_n and relatively insensitive to the Knight field b_e, as evidenced from the modeled curves in Fig. 2.9(b). The low field satellite peak, on the other hand, is due to the rotation of B_n into the spin direction when $B \sim b_e S$, as shown in Fig. 2.10(d), and is thus only observable when a Knight field is present.

The self consistent Crank-Nicolson (CN) calculation shown in Fig. 2.9(b) reproduces the shape of the oblique Hanle curve. The height of the high field satellite peak, which does not recover to the zero field value, is due to the spatial inhomogeneity of the electron, and therefore also the nuclear, spin polarization. This results in a spatially inhomogeneous B_n. Fig. 2.11(a) shows the CN-calculated total transverse field $B_{tot,z} = B_z + B_{n,z}$ along the channel in the oblique geometry. The injector and detector are indicated. The calculated NL signal is obtained by a spatial average of the values between the two white lines. The black lines are the $B_{tot,z} = 0$ Oe contours. Note that the high field $B_{tot,z} = 0$ Oe contour, i.e. B_2, shown in Fig. 2.11(a), indicates that the applied field for which the total field is zero varies by about 200 Oe within the spatial extent of the detector. This spatial inhomogeneity means that the average $B_{tot,z}$ at the detector is never exactly 0 Oe, and the spin signal will not recover its full polarization. We believe that the model's overestimation of the magnitude of the high-field satellite peak is due to the assumptions of purely one-dimensional diffusion as well as a uniform

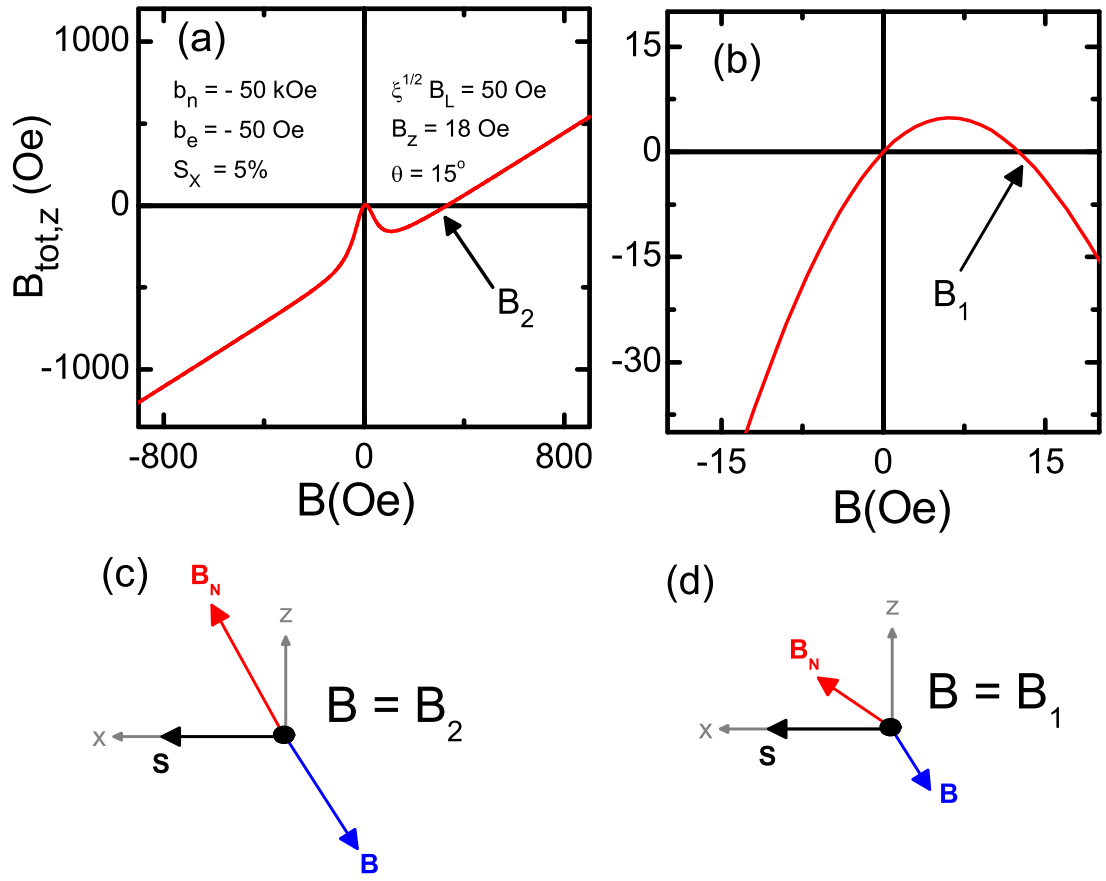

Figure 2.10: (a) Total field in the transverse z direction $B_{tot,z}$ calculated using Eq. 2.29 with nuclear parameters indicated in the figure as a function of B applied at $\theta = 15^o$ relative to the z direction. The spin polarization is in the x direction and fixed: $\mathbf{S} = S_x = +0.025$. (b) Low field region of the calculated $B_{tot,z}$. Schematics show the direction of the hyperfine nuclear field $\mathbf{B}_N$ for $B = B_2$ (c), and for $B = B_1$(d) where B_2 and B_1 are the positions of the high field and low field satellite peaks respectively.

current density across the injection contact, which does not capture the full spatial distribution of the spin polarization in our actual device. Fig. 2.11(b) shows the low field $B_{tot,z} = 0$ Oe, B_1 contour. The low field satellite peak signal is approximately equal to the zero field peak because the B_1 contour is approximately uniform across the detector.

2.3.1 Satellite Peak Positions

The position of the satellite peaks, B_1 and B_2, can be determined analytically[87] by setting

$$B_{tot,z} = B_z + B_{n,z} = 0. \tag{2.36}$$

If we assume that, $\mathbf{S}(B) = S_0$, where S_0 is the spin polarization at $B = 0$ Oe, we obtain the following

$$B^2 + B(b_n + 2b_e)S_0 \sin(\theta) + (b_n + b_e)b_e S_0^2 + \xi B_L^2 = 0. \tag{2.37}$$

Since $b_n \gg b_e$, we can ignore b_e terms in the round brackets. The solution for the two satellite peaks is therefore

$$B_1 = \frac{-b_n S_0 \sin(\theta)}{2} - \sqrt{\left(\frac{b_n S_0 \sin(\theta)}{2}\right)^2 - \left(b_n b_e S_0^2 + \xi B_L^2\right)}, \tag{2.38}$$

$$B_2 = \frac{-b_n S_0 \sin(\theta)}{2} + \sqrt{\left(\frac{b_n S_0 \sin(\theta)}{2}\right)^2 - \left(b_n b_e S_0^2 + \xi B_L^2\right)}. \tag{2.39}$$

Fig. 2.12 shows the measured oblique Hanle curves for different injector biases. CN calculations using the parameters shown in Tab.2.1 and the spin injection rate previously determined from fitting the curves in Fig. 2.6 and 2.7 reproduces the evolution of the satellite peak with bias. At low bias, S is smaller, and B_2 is small enough such that it is not resolved from the central peak. As V_{int} is increased, B_2

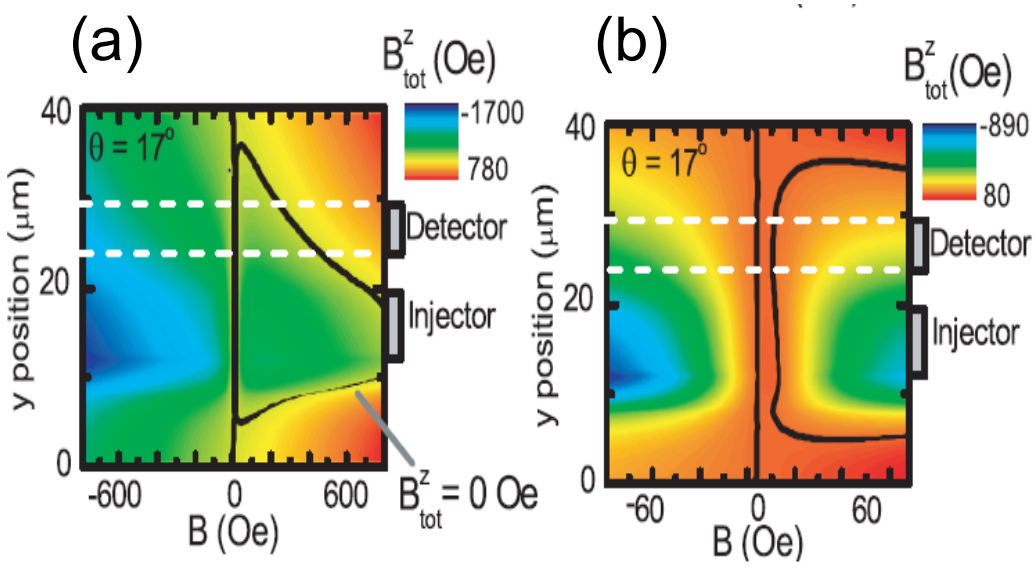

Figure 2.11: (a) Calculated steady state $B_{tot,z} = (\vec{B} + \vec{B}_N)_z$ as a function of position along the GaAs channel (y-position: left axis) and applied magnetic field (bottom axis). $\theta = 17^o$ and $V_{inj} = -0.33$ V. The black lines are the $B_{tot,z} = 0$ Oe contours. The position of the injector and detector are indicated. The white lines mark the boundaries of the detector electrode. (b) Same as (a) with smaller field scale.

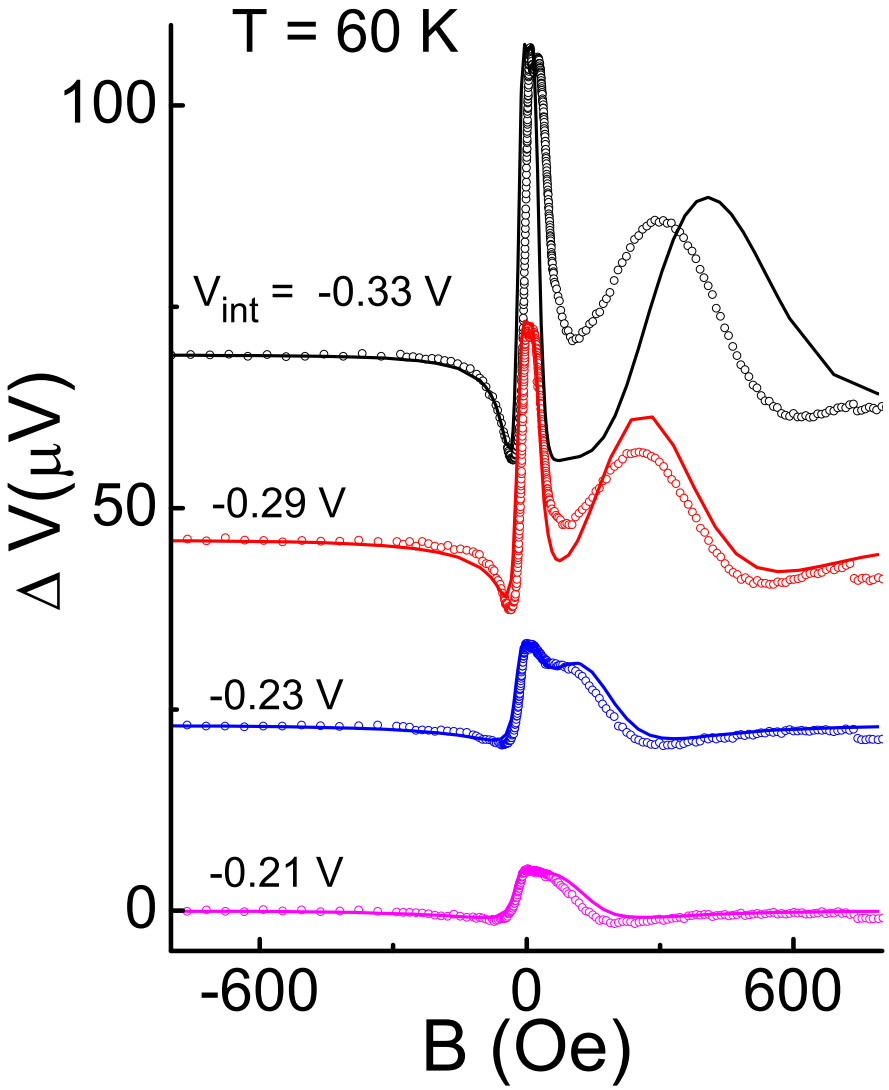

Figure 2.12: (Q59-6) Measured oblique Hanle curves for various injector bias values at $T = 60$ K and $\theta = 17^o$ in the non-local geometry. Open circles are measured and solid lines are calculated self-consistently as described in the text.

increases, and the satellite peak is resolvable. As shown in Fig. 2.13 the measured B_1 and B_2 increase with increasing V_{int}, consistent with the increase of S_0 with injector bias.

The CN modeling reproduces B_1 to approximately 20 % of the measured values. The analytical expression Eq. 2.38 however predicts a decreasing B_1 with increasing V_{int} in contradiction of the measured trend. The failure of the analytical expression for B_1 is not surprising considering the discussion of low field hyperfine effects in Sec. 2.2. At small B, the direction of $\mathbf{B_n}$ is very sensitive to $\mathbf{S}$, which, in the analytical expression, is assumed to be constant. The self consistent CN modeling accounts for the precession of $\mathbf{S}$ and is therefore more successful in reproducing B_1. In the high field regime ($B \gg b_e S$), on the other hand, the direction of $\mathbf{B_n}$ is primarily determined by the direction of $\mathbf{B}$. As stated previously, B_2 is only weakly dependent on b_e, as demonstrated by the modeled curves with and without b_e shown in Fig. 2.9. Since $b_n \gg b_e,\ B_L$, Eq. 2.39 can be approximated, independently of the Knight field, by

$$B_2 = -b_n S_0 \sin(\theta). \tag{2.40}$$

As a result, the analytical expression for B_2 given by Eq. 2.39 reproduces the V_{int} dependence of the measured B_2 shown in Fig. 2.13(b). B_2 as determined from the CN modeling and by Eq. 2.39 is within 50 Oe ($\approx 30\%$) of the measured values at low bias ($V_{int} > -0.3$ V). For high bias, however, both theoretical approaches generate B_2 50% larger than the measured values. As discussed in Chapter 1, the high injector bias regime is not yet fully understood. As a result, the electron spin polarization determined from the NLSV signal size might be incorrect, resulting in the discrepancy of measured and modeled B_2 at high bias. Another possible reason

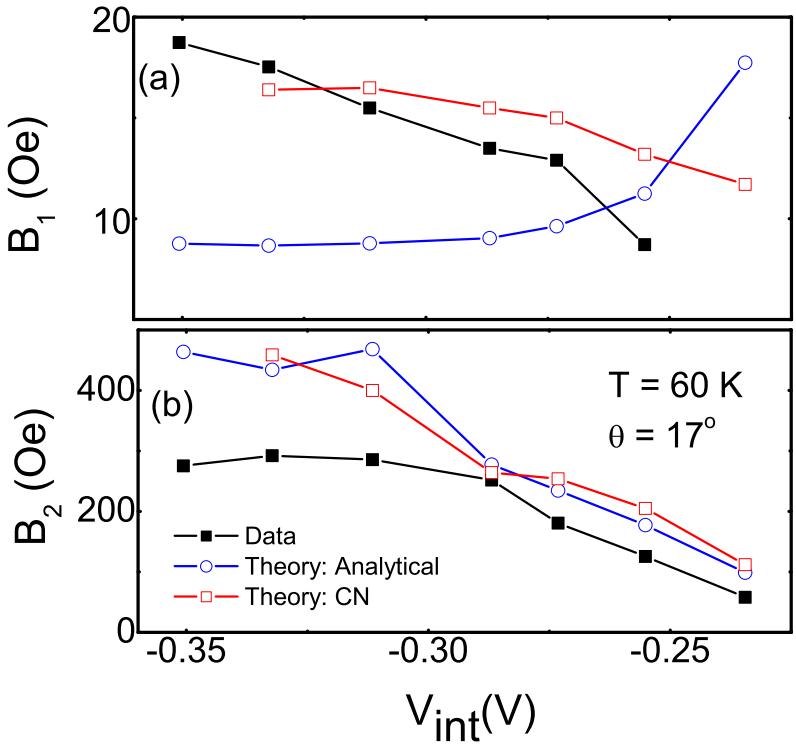

Figure 2.13: (Q59-6) Position of low field (B_1) (a) and high field (B_2) (b) satellite peaks as a function of injection bias in the oblique Hanle configuration. Closed black squares are measured. Open red squares were obtained from CN modeling as described in the text. Open blue circles are calculated from Eqs. 2.38 and 2.39. $T = 60$ K and $\theta = 15^o$.

for the discrepancy is that the large electric fields in the semiconductor under large applied bias produce greater spatial inhomogeneity in the spin polarization along the channel, which is not sufficiently accounted for by the theoretical models used.

As the polar angle θ of the applied field is increased, the high field satellite peak shifts to larger fields, as shown in Fig. 2.14. Both the analytical and CN models reproduce the evolution of B_2 with θ very accurately, as shown in Fig. 2.15. The high degree of agreement between the measured and calculated curves in the oblique Hanle geometry without using any free parameters, further adds to the confidence we have in the extracted parameter values. We have found that it is not possible to determine the Knight field coefficient, b_e, by simply reading out measured peaks or dips in the field dependence of the spin signal. A self consistent calculation that accounts for the co-evolution of nuclear-electron spin system is required to understand the low field features which are sensitive to the Knight field. On the other hand, given S_0, the nuclear hyperfine coefficient, b_n can be easily estimated from the position of B_2 in the oblique Hanle geometry by using Eq. 2.40.

2.4 Temperature Dependence of the Hyperfine Interaction

As mentioned in Sec. 2.1.1, the nuclei in GaAs are oriented through dynamic nuclear polarization arising from localized donor electrons. As the temperature increases, the localized donor electron density decreases because of thermal excitation into the conduction band. We would therefore expect that dynamic nuclear

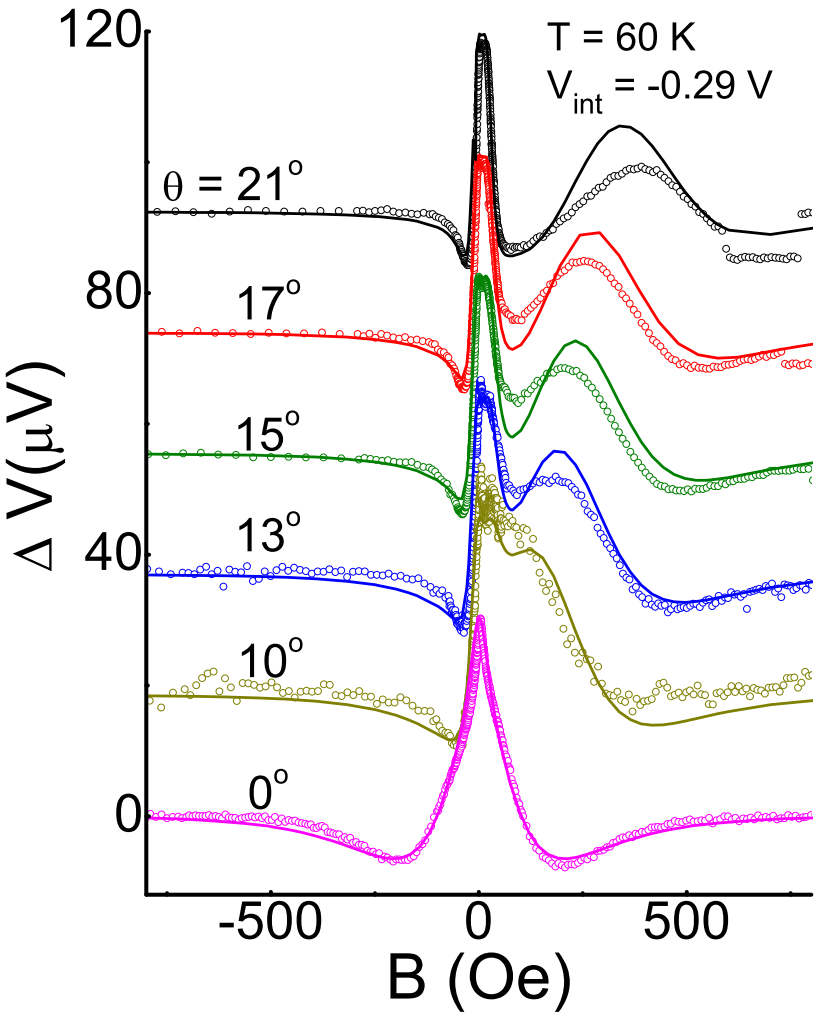

Figure 2.14: (Q59-6) Oblique Hanle curves in the non-local configuration for applied field B applied at different angles relative to the z axis. Open circles are measured curves. Solid lines are self consistent calculations as described in the text. $T = 60$ K and $V_{int} = -0.29$ V.

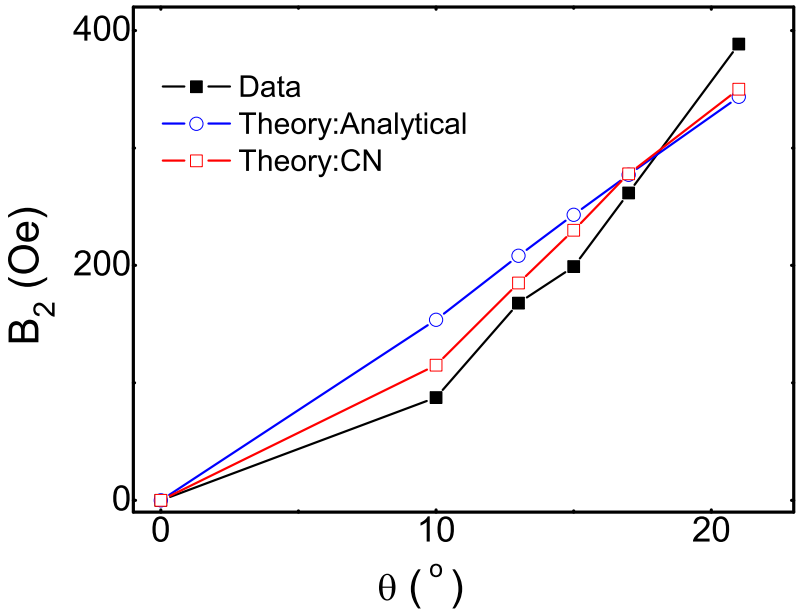

Figure 2.15: (Q59-6) Position of the high field satellite peak in the non-local oblique Hanle configuration as a function of polar angle. Closed squares are data. Open circles and squares are theoretical calculations using Eq. 2.39 and self consistent Crank - Nicholson calculations respectively.

polarization is suppressed at high temperatures. The low field features in longitudinal field sweeps are attributable to precession of **S** about the transverse hyperfine field, as discussed in Sec. 2.2. Fig. 2.16 shows the temperature dependence of the low field features (normalized by the NLSV signal at each temeprature in order to exclude the temperature dependence of the spin signal) in both the three terminal and non-local configurations. A constant transverse field of $B_z = 26$ Oe is applied. In order to ensure that the nuclear polarization is approximately in steady state, the sweep rate was kept very low, ≈ 0.01 Oe/s at $T = 20$ K. T_1 at 20 K is measured to be about 120 s in the field range in question. It is clear

that the hyperfine features in Fig. 2.16 are suppressed with increasing temperature, eventually disappearing, within experimental resolution, at about 120 K. The temperature dependence of the NLSV signal is shown in Fig. 1.23(a). The electron spin signal persists above 120 K, and is observable up to 200 K.

The solid lines are modeling results using Eq. 3.31 and the CN method as described previously. In this modeling, D and v_d were previously determined from transport measurements. τ_s was determined from fitting non-local Hanle measurements shown in Fig. 1.22, which were measured on the same sample and contacts as those used for the data in Fig. 2.16. The spin injection rate $\dot{S}_0$ was set such that the modeling produced the correct spin polarization at the detector as calculated from the NLSV signal and Eq. 2.35. b_n, b_e, and $\sqrt{\xi}B_L$ were free parameters for each temperature. The 3T and NL curves were calculated simultaneously with the same modeling parameters.

The temperature dependence of the extracted parameters are shown in Fig. 2.17 (b)-(d). Both b_n and b_e decrease monotonically with temperature, approaching zero at $\approx 120\ K$. $\sqrt{\xi}B_L$ on the other hand increases with increasing temperature. Values above 120 K are not obtainable because, as seen in Fig. 2.16, hyperfine features are not observable. The resistivity of the GaAs channel ρ measured in a 4-terminal configuration for applied biases above and below the impact ionization threshold is shown in Fig. 2.17(a). It is clear from the resistivity data that donor impact ionization is only active below $\approx$ 130 K, indicating the lack of localized electrons on donor sites above 130 K. At lower temperatures, the observation of donor impact ionization suggests trapping of electrons on donor sites. This temperature dependence agrees with that for the hyperfine coefficients shown in

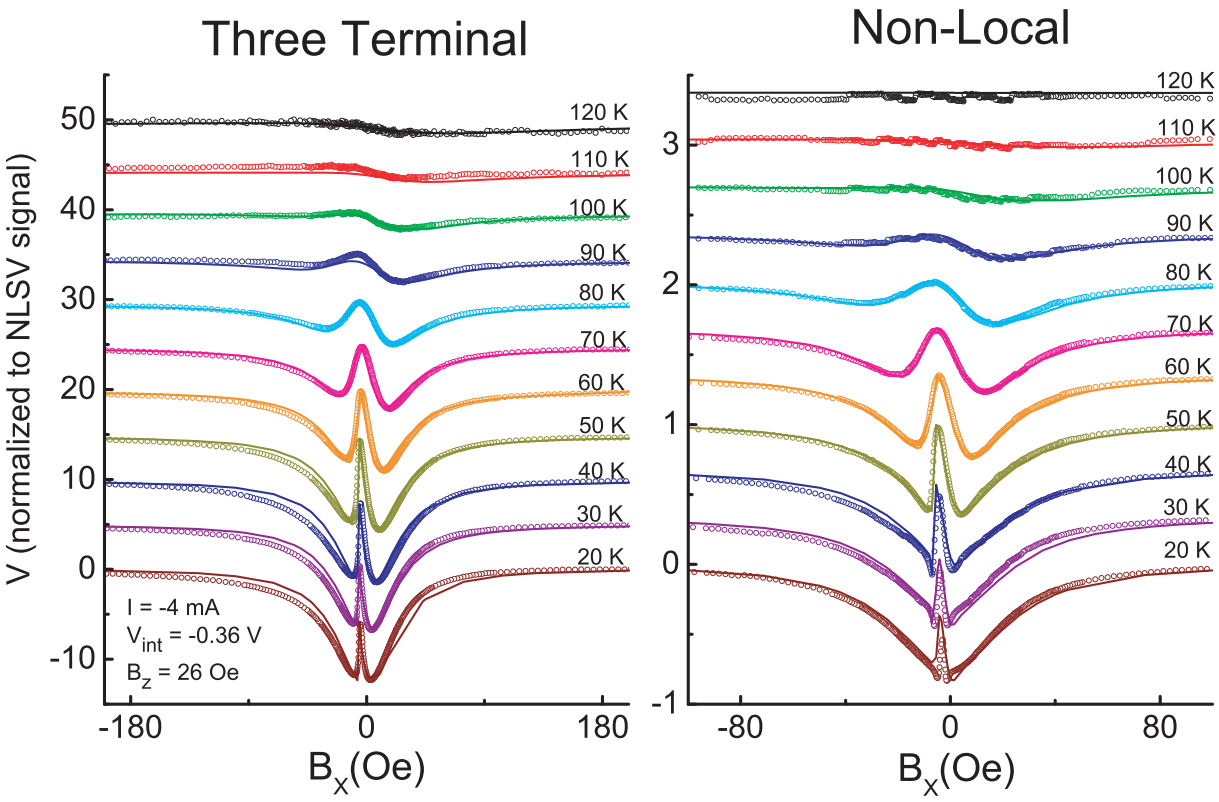

Figure 2.16: (Q62-1) Three terminal (left panel) and non-local (right panel) curves with field swept in the longitudinal x direction as a function of temperature. A constant transverse field $B_z = 26$ Oe was applied. $V_{int} = -0.36$ V. Open circles are data. Solid lines are the result of self-consistent Crank-Nicholson modeling as described in the text.

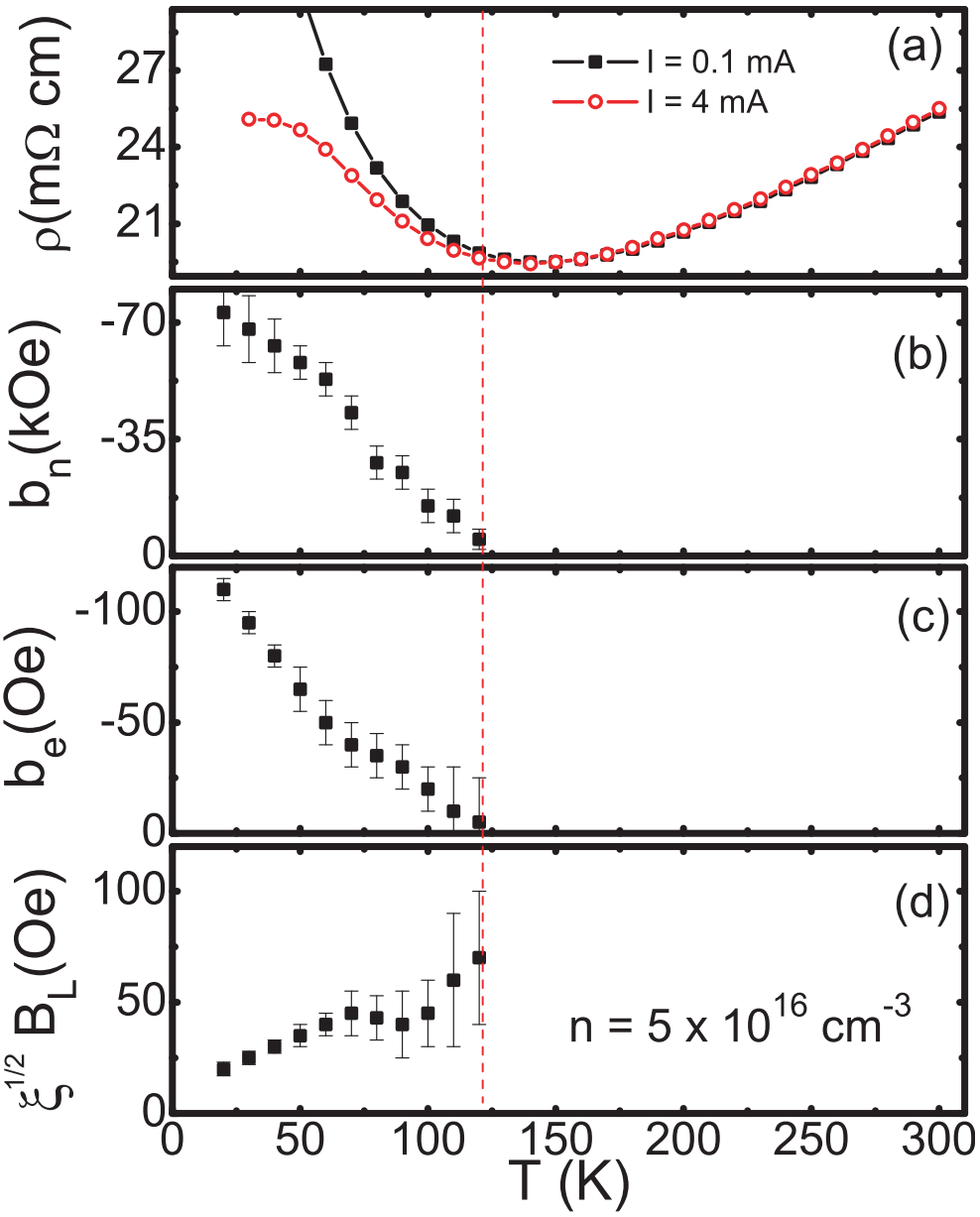

Figure 2.17: (Q62) (a) Temperature dependence of resistivity ρ for applied bias below(open circles) and above(solid squares) the impact ionization threshold. Temperature dependence of b_n (b), b_e (c), and $\sqrt{\xi}B_L$ (d) extracted from fitting the measured longitudinal field sweeps. (Transport data in (a) is courtesy of Eric Garlid)

Fig. 2.17(b)-(d) and is consistent with the importance of localized electrons to DNP.

As stated earlier, b_n and b_e are reduced from their theoretical maximum values from Eq. 2.31 by the pre-factors f and Γ. Γ, which parameterizes the fraction of time the electron is localized on the donor site, decreases with increasing temperature. The leakage f is given by the ratio of the hyperfine relaxation rate to the total nuclear relaxation rate $f = T_{pol}^{-1}/(T_1^{-1} + T_{pol}^{-1})$, Eq. 2.33. ξ on the other hand is proportional to the ratio of the total relaxation to the hyperfine mediated relaxation rate T_{pol}/T_1. As the relative relaxation rate of the hyperfine and non-hyperfine processes change, f and ξ should evolve in opposite directions. From Eq. 2.15, $T_{pol} \propto 1/\Gamma$, so T_{pol} is expected to increase with increasing temperature, thus resulting in the observed drop in f and increase in ξ at higher temperatures.

2.5 Nuclear Magnetic Resonance (NMR)

A final indication of the strong coupling of the electron and nuclear spin systems is provided by the detection of nuclear magnetic resonance (NMR) when an ac magnetic field is applied by a small coil placed over the sample. In NMR measurements, $\mathbf{B}$, applied at a polar angle $\theta = 15^o$, is fixed at ≈ 320 Oe, which is close to the position of the high field satellite peak, as indicated by the dotted vertical line in Fig. 2.18(a) and (b). The frequency f of the AC field is swept while monitoring either V_{3T} or V_{NL}. The resonance condition for NMR is given by $B_{tot} = \gamma_i f_i$, where B_{tot} is the total magnetic field exerted on the nuclei, γ_i is the gyromagnetic ratio for the nuclear species in question, parameterized by i, and f_i is the resonance frequency. When the nuclei are off-resonance, the electron spin polarization

is suppressed by precession around B_n. At a resonance, the nuclei are partially thermalized, B_n is reduced, and the the satellite peak shifts to lower fields. The shift in the satellite peak is observed as peaks (Fig. 2.18(c)) or dips (Fig. 2.18(d): note the negative sign of the left axes) in the frequency spectra. This approach can be used to observe all of the possible transitions in the $I = 3/2$ manifold for each of the three isotopes (^{69}Ga, ^{71}Ga, and ^{75}As) present in the sample, as shown in Fig. 2.19. The observation of higher order ($\Delta m = \pm 2, \pm 3$) transitions is due to dipolar interactions (which also lead to the "sum transitions" from two different isotopes) or quadrupolar coupling. [32]

The NMR frequency f_i is set by the the total applied field, which is the sum of the externally applied field and the Knight field: $B_{tot} = B + b_e S$. The shift in f_i from the one expected from the applied field can therefore provide a direct measure of the Knight field. In our system, at $T = 60$ K we estimate that $S \approx .07$ ($P = 14\%$), which, taking $b_e = -50$ Oe as determined previously, yields a Knight field of ≈ 4 Oe, or, using a typical $\gamma \approx 1$ kHz/Oe for GaAs, a Knight shift of $\delta f_i \approx 4$ kHz. In Fig. 2.20, we show NMR spectra for various injector biases measured in the three terminal configuration. From the previously determined 3T spin polarization, we expect $\delta f_i \approx 0.5$ kHz between the highest and lowest V_{int} shown in Fig. 2.20 (b). The shift is exceedingly small because $\mathbf{B}$ and $b_e\mathbf{S}$ are not parallel to each other in the oblique geometry used here. As a result the contribution of the Knight field to the magnitude of B_{tot} is rather small when $B \gg b_e S$. The width of the resonance peaks is ≈ 20 kHz, and no perceptible shift in the resonance frequency is observed. Further experiments at lower temperatures and in the longitudinal configuration offer better prospects for observing the Knight

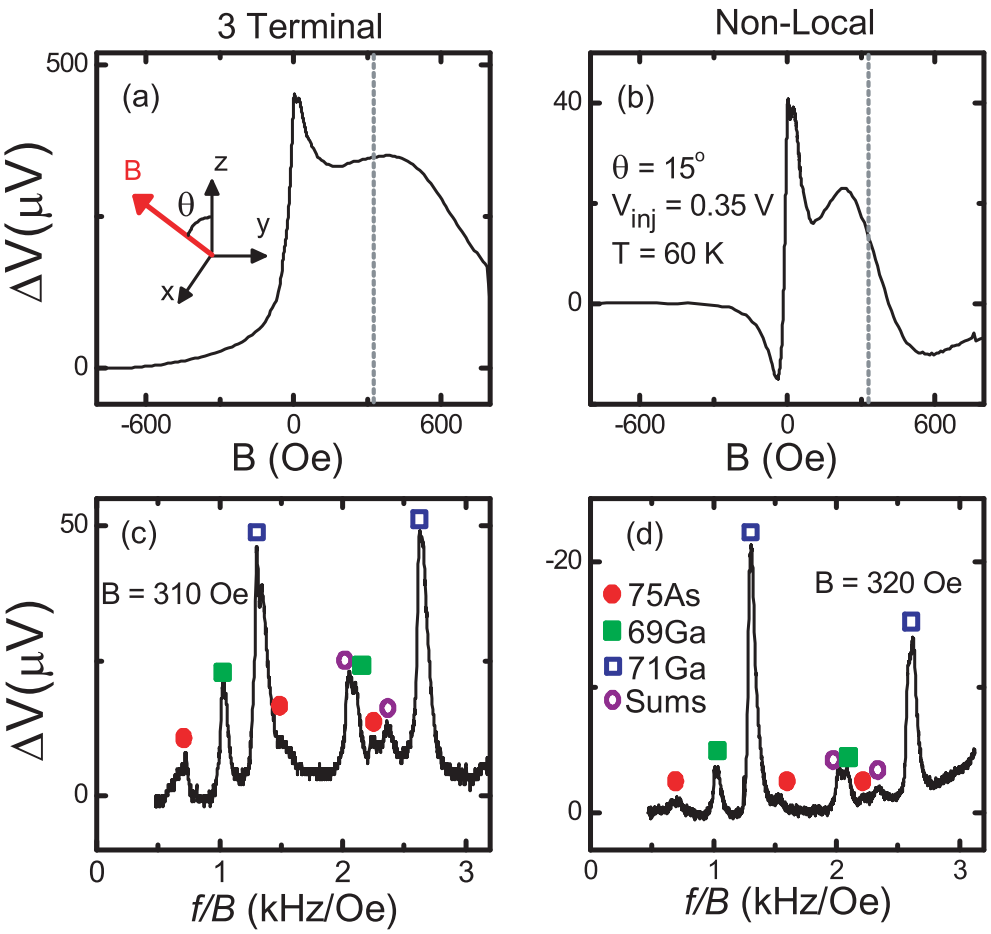

Figure 2.18: (Q59-6) Oblique Hanle curves: Three-terminal voltage (V_{3T}) (a) and non-local voltage (V_{NL}) (b) as a function of magnetic field B applied at polar angle $\theta = 15^o$ at $T = 60\ K$. The schematic indicates the direction of the magnetic field. Spin injection is along the x direction. The dotted lines indicates the constant magnetic field at which the frequency dependence of the three-terminal (c) and non-local (d) voltage is measured. The observed resonances are identified with each isotope as indicated in the legend. At the resonance frequency, the high field satellite peak moves closer to 0 Oe due to the suppression of the nuclear field B_n. This results in a positive change in V_{3T} and negative change in V_{NL} as shown in (c) and (d). Note that a constant offset has been subtracted from (c) and (d)

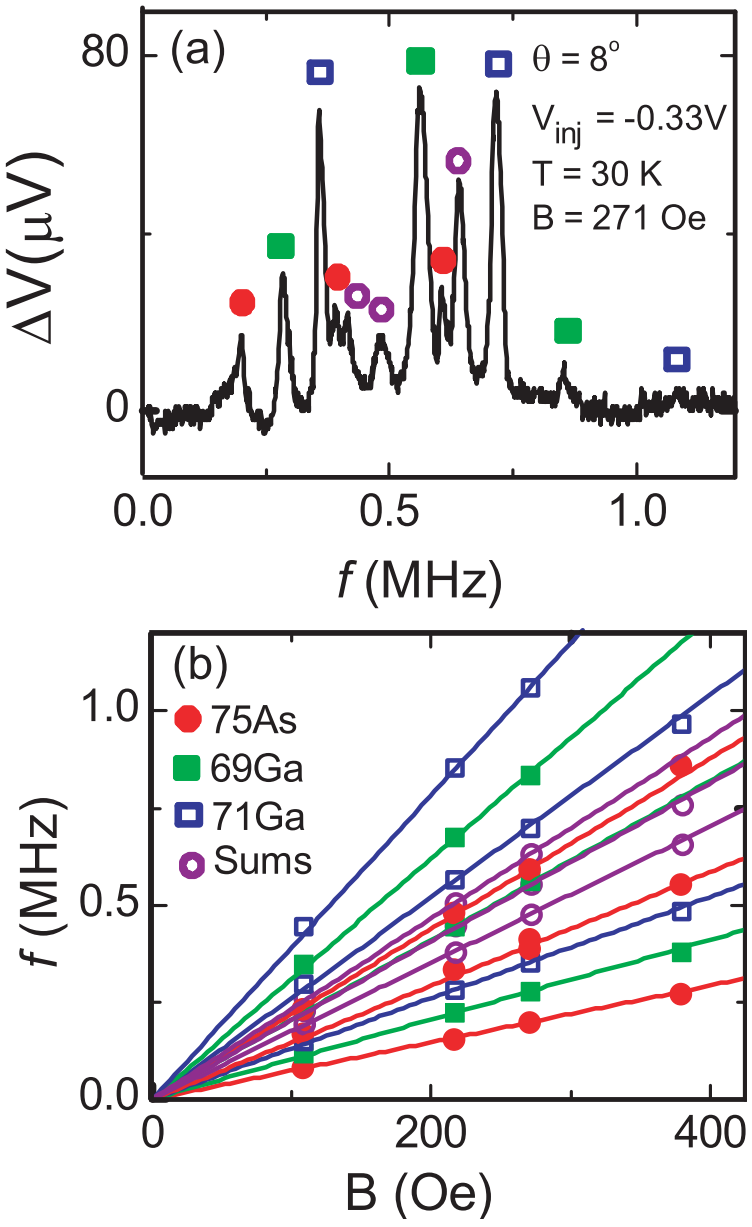

Figure 2.19: (Q59-6) (a) The three-terminal voltage V_{3T} as a function of frequency of applied ac magnetic field. The observed resonances for each isotope are indicated in the legend. Transitions at the sums of the fundamental frequencies of different isotopes are also observed. (b) Resonant frequencies as a function of applied field. The points were determined from NMR spectra at fixed field. The lines are calculated for 1^{st}, 2^{nd}, 3^{rd}, and sum harmonics of Ga and As nuclei.

shift.

2.6 Nuclear Field Suppression

As shown in Fig. 2.9(a), the hyperfine field B_n acting on the electron spins results in a narrowing of the Hanle curve. In order to extract the electron spin lifetime τ_s from Hanle measurements, we would have to include hyperfine effects. By performing measurements in various applied field configurations, as shown in Sections 2.2 and 2.3 we were able to extract the nuclear field coefficients, as well as τ_s. This method, however, involves a large number of measurements in order to constrain the large number of free parameters in the fitting procedure. An alternative method is to suppress the effects of the nuclear field during the measurement.

Previous electrical measurements have attempted to avoid the worst effects of the hyperfine interaction by starting the field sweep at zero applied field, where B_n is nominally very small.[43] We have found, however, that this is insufficient at low temperatures. The large value of b_n means that even a small remnant field of ~ 1 Oe can produce a large enough transverse nuclear field (~ 100 Oe) to alter the measured Hanle curve. Additionally, the nuclear spin polarization will build up as B is swept to larger fields.

In experiments where electron spin polarization is injected optically, nuclear field suppression can be achieved easily by modulating the excitation light between left and right polarizations at a frequency much greater than $1/T_1$.[94] In this way, the time averaged electronic spin polarization is zero and the nuclei do

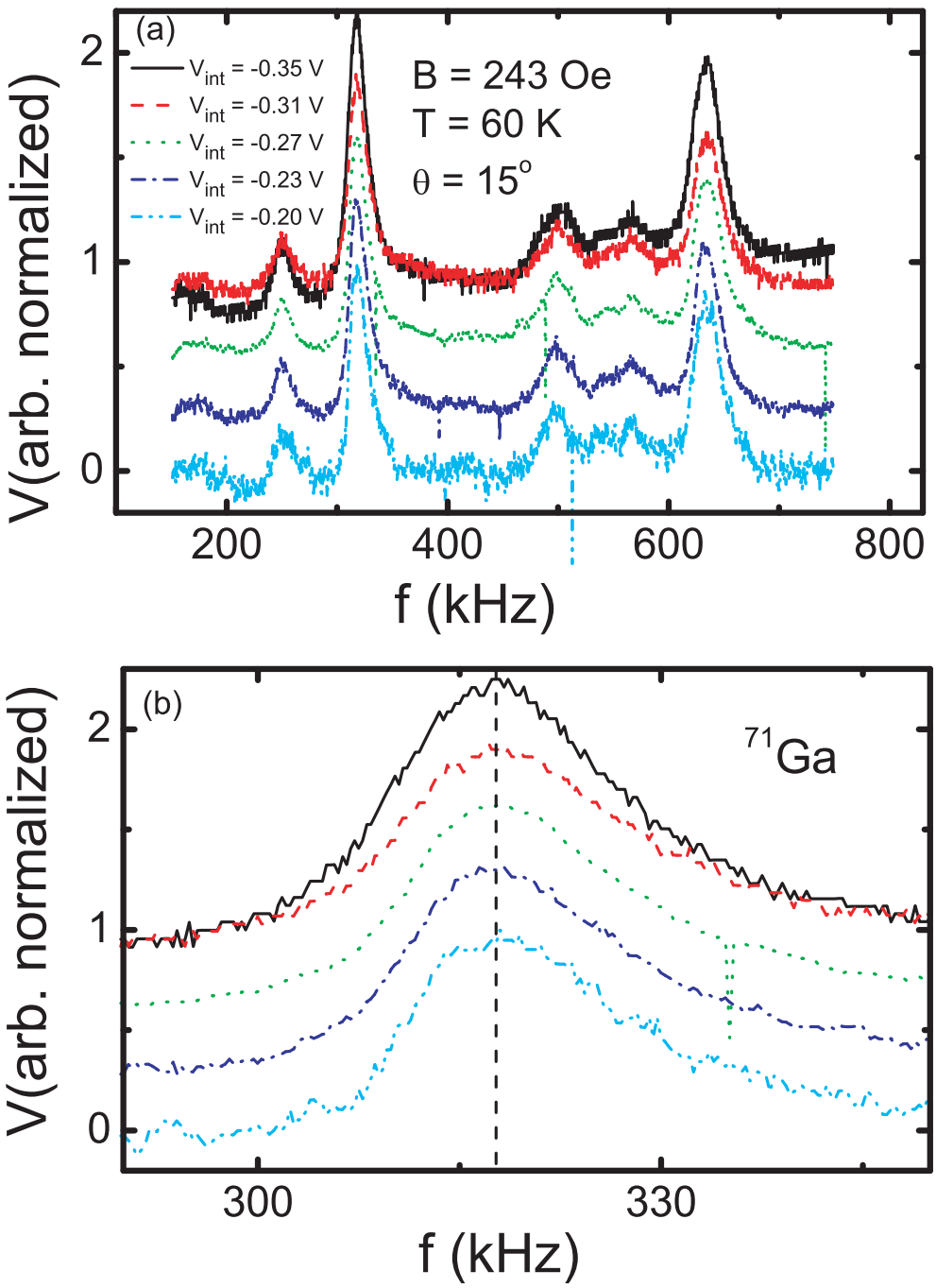

Figure 2.20: (Q59-6) (a) NMR spectra for various injector biases (V_{int})measured in the three terminal configuration. The signal is normalized to the ^{71}Ga peak height, and spectra are shifted vertically for clarity. $T = 60$ K. (b) Closeup of the ^{71}Ga peak for different V_{int}.

not polarize. This method cannot be employed in our experiment unless we can quickly modulate the sign of the electrically injected spin polarization, which is not feasible. Another method, employed by Berkovitz *et al.*[95], exploited the long T_1 in nuclei. In their experiment, linearly polarized light is initially incident on the sample, holding nuclear spins unpolarized. Circularly polarized light is then quickly switched on to inject electron spin polarization, and the electron spin is measured before the nuclear polarization can build up.

Due to the sensitivity of the measured voltages in our experiments to temperature variations, we are not able to implement this method exactly. When the injector bias is changed to turn spin injection on and off, the sample temperature does not equilibrate quickly enough to perform a stable measurement before the nuclei polarize. Instead, we use irradiation by an AC magnetic field at $B \approx 0$ Oe to depolarize the nuclei, then ramp B quickly to the desired field, and measure the electron spin polarization at a rate $\gg 1/T_{pol}$. Implementation of this field cycling procedure successfully suppresses the influence of the hyperfine field on the measured Hanle curves.

The schematic in Fig. 2.21 shows a summary of the field cycling procedure. Before starting the field sweep, we wait at $B \approx 0$ Oe for ~ 60 s while irradiating the sample with B_{AC}. B_{AC} is applied in order to depolarize the nuclei. Since γ_i in GaAs is ≈ 1 kHz/Oe, B_{AC} is applied at frequencies: 2 kHz and 5 kHz, thus accounting for the relatively large remnant fields (~ 5 Oe) of the electromagnet used. The applied field is then swept quickly (≈ 100 ms) to the measurement field $B_{measure}$, where it stays for $T_{measure} \approx 500$ ms before the voltage is read out. The field is then ramped quickly back to $B = 0$ Oe, and stays there for

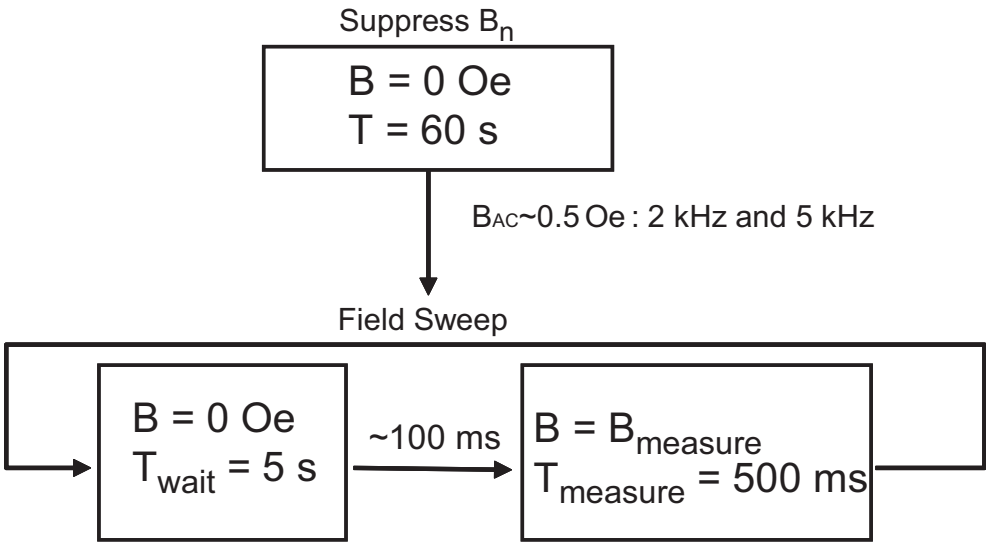

Figure 2.21: Schematic of the field cycling procedure to suppress B_n.

$T_{wait} = 5$ s while being irradiated by B_{AC}. This step ensures that any built up nuclear polarization is again suppressed. This cycle is repeated for all constituent $B_{measure}$ in the field sweep. Note that $T_{measure} \ll T_{pol}$, where $T_{pol} \sim 10$ s. This ensures that B_n does not build up significantly during the measurement.

Fig. 2.22 shows the effect of the field cycling procedure on a measured oblique Hanle curve. The solid square red data points show an ordinary 3T oblique Hanle curve measured without the field cycling procedure at a polar angle $\theta = 5^o$ and $T = 10$ K. The satellite peak indicating a hyperfine field is observed. The open circles show data obtained using the field cycling procedure described above, in the same oblique geometry. The satellite peak is no longer observed. Furthermore, the Hanle curve is almost perfectly symmetric about 0 Oe, indicating full suppression of B_n within the resolution of our measurement. The solid line in Fig. 2.22 is the calculated Hanle curve with $B_n = 0$ Oe and the same τ_s, D_f and v_d as those used to fit the 10 K curve in Fig. 1.26. The close agreement between the measured

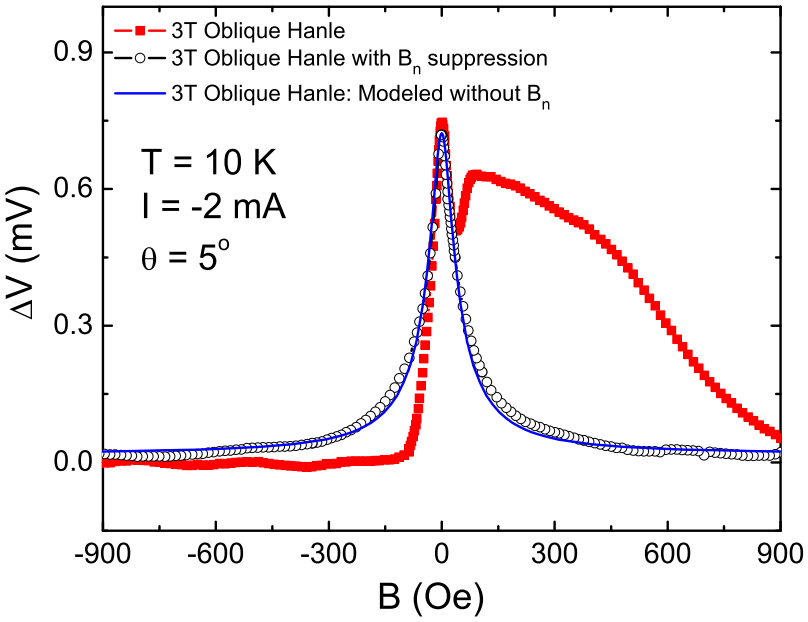

Figure 2.22: Measure oblique Hanle curves with (open circles) and without (solid squares) B_n suppressing field cycling procedure. Solid line is the calculated curve ignoring B_n and with $\tau_s = 11.2$ ns.

and calculated curves indicates successful elimination of hyperfine effects. This procedure was used to determine τ_s accurately as a function of temperature in Chapter 1.

2.7 Conclusion

In this chapter we have discussed the dynamic nuclear polarization of nuclear spins by polarized electrons in Fe/GaAs heterostructures. The resultant large nuclear polarization manifests itself in a hyperfine field acting on electron spins. We have

observed rich applied field dependence of electron spin dynamics as electron spins precess about the hyperfine field. By implementing a self consistent numerical calculation of the electron spin dynamics and of the mean field nuclear spin polarization, we were able to determine the strength of the hyperfine and Knight fields. This numerical calculation accurately reproduces the field dependence of the measured electron spin signal in various applied field configurations. We have also shown that it is possible to perform all electrical nuclear magnetic resonance measurements in GaAs in applied fields of only a few hundred Oe.

Chapter 3

Spin-dependent Hall Effect

3.1 Spin Hall Effect: An Introduction

In Chapter 1 we discussed transport of electron spin polarization in Fe/GaAs heterostructures. In Chapter 2, we showed that the electron and nuclear spins are coupled through the hyperfine interaction. This chapter concerns transport phenomena that couple the spin degree of freedom and charge transport through spin-orbit (SO) coupling. These effects, are varieties of the spin Hall effect, which was predicted in 1971 by D'yakonov and Perel'.[96, 97] We will show that the electron transport is coupled to *both* the electron and nuclear spin degrees of freedom through measurements of a spin-dependent Hall effect.

3.2 Phenomenological Description

In this section, we will review the phenomenological equations introduced by D'yakonov and Perel' describing the transport of charge and spin currents with

spin-orbit interaction.[96] We start by introducing charge and spin currents without spin-orbit coupling:

$$\frac{\mathbf{j}^0}{e} = \mu n \mathbf{E} + D\nabla n, \tag{3.1}$$

$$q^0_{ij} = -\mu E_i p_j - D\frac{\partial p_j}{\partial x_i}, \tag{3.2}$$

where μ is the mobility, n is the carrier density, E is the electric field, and D is the diffusion constant. The superscript ' ^{0} ' indicates that spin-orbit interactions have not yet been included. $p_j = P_j n$ is the spin polarization density, and has units $[1/\mathrm{m}^3]$. q_{ij} is the spin current density flowing in the i direction for spins polarized in the j direction. It is defined, for the example of spins in the z direction flowing in the i direction, as

$$q_{iz} \equiv -\frac{j_i^{\uparrow} - j_i^{\downarrow}}{e}, \tag{3.3}$$

where $j_i^{\uparrow}$ and $j_i^{\downarrow}$ are the charge current densities of the up and down spin channels, quantized in the z direction. The spin orbit interaction couples $\mathbf{j^0}$ and q^0_{ij}, such that the charge and spin current densities can be rewritten as

$$\frac{\mathbf{j}}{e} = \frac{\mathbf{j}^0}{e} - \gamma \varepsilon_{ijk} q^0_{jk}, \tag{3.4}$$

$$q_{ij} = q^0_{ij} + \gamma \varepsilon_{ijk} \frac{j^0_k}{e}, \tag{3.5}$$

where γ is a dimensionless parameter that is proportional to the strength of the spin-orbit interaction. Rewriting the two equations above we get

$$\frac{\mathbf{j}}{e} = \mu n \mathbf{E} + D\nabla n + \gamma \mu \boldsymbol{E} \times \boldsymbol{p} + \gamma D \nabla \times \boldsymbol{p}, \tag{3.6}$$

$$q_{ij} = -\mu E_i p_j - D\frac{\partial p_j}{\partial x_i} + \gamma \mu n \varepsilon_{ijk} E_k + \gamma D \varepsilon_{ijk} \frac{\partial n}{\partial x_k}. \tag{3.7}$$

Note that unlike the charge density, the spin density is dissipative; thus

$$\frac{\partial p_j}{\partial t} + \frac{\partial q_{ij}}{\partial x_i} + \frac{p_j}{\tau_s} = 0, \tag{3.8}$$

where τ_s is the spin relaxation time. The various effects associated with the SO coupling can be described using the above expressions.

Eqs. 3.6 and Eq. 3.7 cover numerous effects. The third and fourth terms in Eq. 3.6 are known as the anomalous Hall effect (AHE) and the inverse spin Hall effect (iSHE) respectively. They describe conversion of spin current into charge current. The third term in Eq. 3.7 is known as the spin Hall effect (SHE), which describes a conversion of charge current into spin current. All of these effects have essentially the same microscopic origins. We will sometimes refer to them generally as the spin Hall effect (SHE) despite the more specific definition of the term given below.

3.2.1 Anomalous Hall Effect (AHE)

The anomalous Hall effect in ferromagnets was discovered by Hall in 1880.[98] Fig. 3.1(a) shows the Hall measurement configuration. A longitudinal electric field is applied along the y direction. B is applied out of the plane, and the Hall voltage is measured in the transverse direction. For non-magnetic materials, the normal Hall effect describes the transverse Lorentz force acting on the electrons, resulting in charge build up along the edges of the channel. This is described in Sec. 1.6.2 as a means to determine the carrier density. In a ferromagnetic material, an anomalously large Hall voltage is observed as the magnetization of the film tilts towards the applied transverse field. Empirically, the Hall resistivity is written as[100]

$$\rho_H = -\rho_{xy} = R_0 B_z + 4\pi R_s M_z, \tag{3.9}$$

where R_0 and R_s are the ordinary and anomalous Hall coefficients respectively, and M_z is the magnetization in the z direction. The large change in V_H as B_z is increased is due to the the increase in M_z as the magnetization $\mathbf{M}$ aligns with the applied field. When $\mathbf{M}$ is saturated in the z direction, M_z no longer changes with applied B_z, and the slope of V_H returns to a small value, representing the ordinary Hall effect. It is generally agreed that the AHE is caused by the spin-orbit interaction, but the details of the microscopic origins are a hotly debated topic.[100] From Eq. 3.6, the AHE is represented by $j_x/e = \gamma\mu E_y p_z$ where the polarization density in the z direction p_z is directly proportional to M_z.

In non-magnetic semiconductors, the ordinary Hall effect, due to the low number of carriers, is typically larger than the AHE. Chazalviel and Solomon managed to separate the two effects by measuring the Hall voltage in InSb as it is driven through the resonance of the conduction electrons.[101]

3.2.2 Inverse Spin Hall Effect (iSHE)

The term $\gamma D \nabla \times \mathbf{p}$ in Eq. 3.6 is referred to as the inverse spin Hall effect (iSHE). Unlike the AHE which is driven by the electric field, the iSHE is due to diffusion of in-homogenous spin polarization. The first measurement of this effect was performed by Bakun *et al.* The measurement configuration is shown in Fig. 3.2(a). They injected spins polarized in the z direction into a thin slab of $Ga_{0.73}Al_{0.27}As$ with circularly polarized light. The Hall voltage was measured as a magnetic field was applied in the transverse direction. At $B = 0$ Oe, $\nabla \times \mathbf{p} = \mathbf{0}$ and no Hall voltage is measured, as shown in Fig. 3.2(b). The application of a transverse magnetic field tilts $\mathbf{p}$ into the y direction and a Hall voltage is measured. The

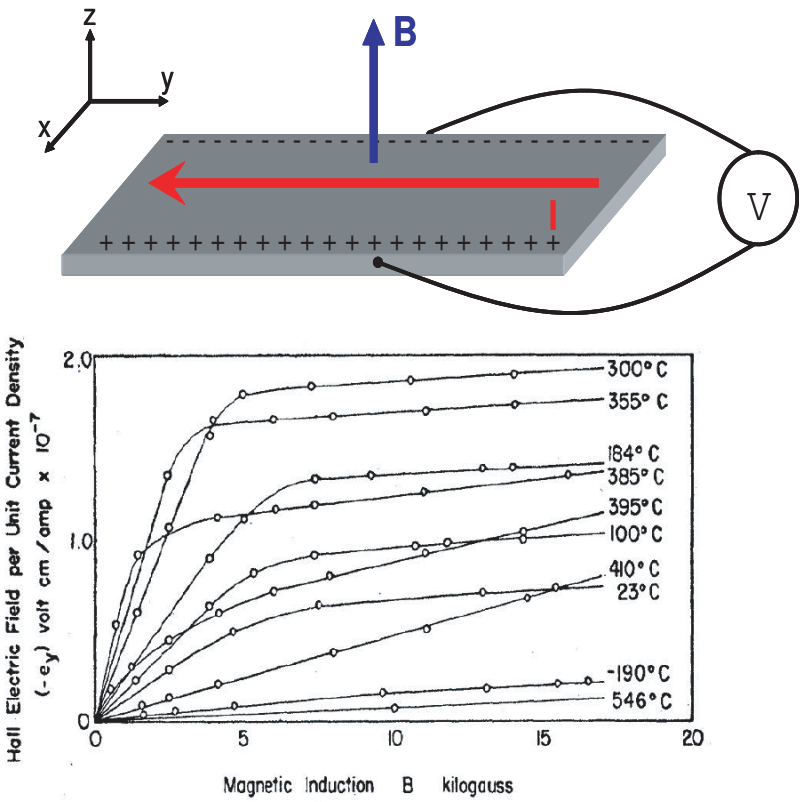

Figure 3.1: (a) Hall measurement configuration. A longitudinal electric field is applied in the y direction. B is applied out of the plane. The Hall voltage is measured across the channel. (b) Example of anomalous Hall effect data for Ni (from Ref. [99]).

shape of the V_H curve is just the transverse component of the average longitudinal spin polarization curve, shown in Fig. 3.2(c). Tkachuk *et al.*[103] implemented the same measurement configuration as Bakun and co-workers. They, however, optically injected spins at a slow enough rate such that dynamic nuclear polarization of the nuclei was active. They monitored V_H, while applying a constant magnetic field and sweeping the frequency of an applied AC field. They were able to observe nuclear magnetic resonances due to thermalization of the polarized nuclei, showing conclusively that the measured Hall voltage is spin-dependent.

In metallic systems, the iSHE was first measured by Valenzuela and Tinkham in aluminium.[104] In their experiment, spins were injected electrically through a ferromagnetic contact. Hall arms, placed in the non-local configuration along the channel monitors V_H due to diffusion of spins from the injector contact. When the magnetization of the F injector was switched, $\mathbf{p}$ changed sign, and they observed a corresponding change in sign of V_H. Since then, a number of similar experiments have been reported in various metallic systems.[105–107] The Hanle effect for the iSHE has, however, not been observed in metals.

The AHE and iSHE in non-magnetic semiconductors can also be observed for electrically injected spin polarization, as suggested by Zhang[108] and Hirsch[109]. Although Zhang only considered the AHE, we will include both the AHE and the iSHE below. A simple schematic of a proposed device is shown in Fig. 3.3(a). Spin polarization is injected from an Fe/GaAs Shottky contact. The direction of injected spin polarization at the interface P_0, is determined by the magnetization of the Fe injector M_i. Spin-orbit coupling results in preferential transverse scattering of the spin polarized current, thus resulting in a spin-dependent Hall

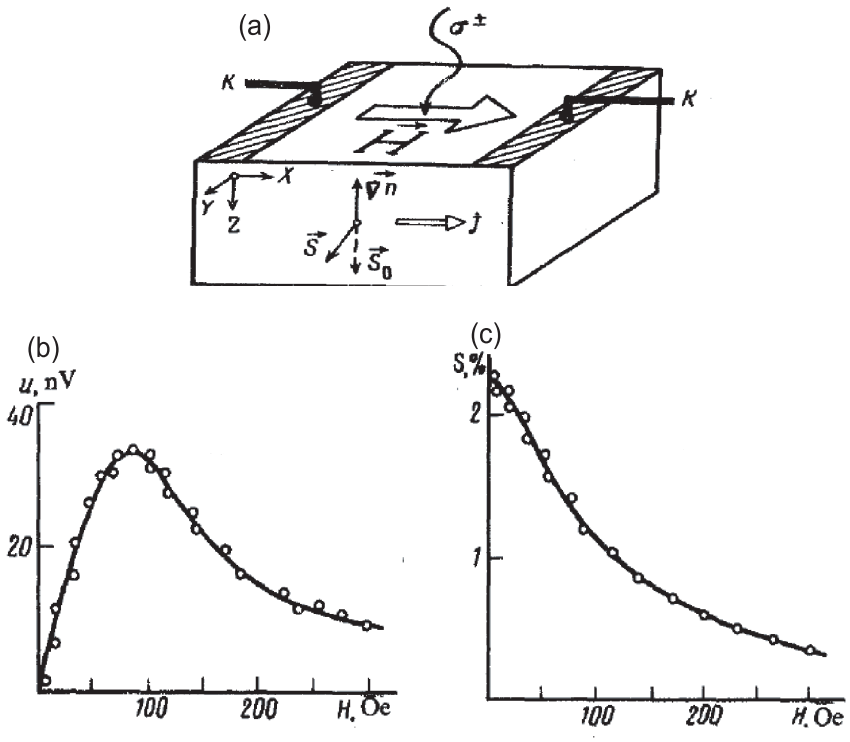

Figure 3.2: (a) Measurement configuration used in the first experimental observation of the inverse spin Hall effect. Circularly polarized light injects spin polarization in the z direction. Magnetic field H is applied in plane to rotate spins into the y direction. The Hall voltage is measured across the sample in the x direction. (b) Measured Hall voltage as a function of applied field. (c) Measured circular polarization of luminescence, which is proportional to the z component of average electron spin in the sample.(from Ref. [102]).

voltage measured along the transverse x direction. The expected spin-dependent Hall voltage is determined from steady state considerations such that $j_y = 0$ in Eq. 3.6. From the continuity equation: $P = P_0 e^{-z/\lambda}$ where λ is the spin diffusion length. Assuming uniform charge density, we have

$$V_H = wE_x = -w\frac{\sigma_{AHE}}{\sigma^2} jP_y + w\frac{\sigma_{iSHE}}{\sigma} P_y, \tag{3.10}$$

where w is the width of the Fe contact, $P_z = p_z/n$, and

$$\sigma_{AHE} \equiv en\gamma\mu, \tag{3.11}$$

$$\sigma_{iSHE} \equiv en\gamma D/\lambda. \tag{3.12}$$

Note that σ_{iSHE} is not a true conductivity, and so does not have the units of conductivity. Eq. 3.10 includes both the AHE (drift) and iSHE (diffusive) contributions to the measured Hall signal. We have assumed that the electric field is only in the z direction and that P does not vary spatially in the y direction, such that V_H is dependent only on P_y. If M_i is aligned along the x direction, $P_0 \parallel x$, and $V_H = 0$. However, as was done in the experiment by Bakun *et al.*[102], a transverse magnetic field can be applied to tilt the spin polarization in the GaAs into the y direction, thus resulting in a non-zero V_H. This is just a Hanle measurement, analogous to the electrical measurements of spin polarization performed using an Fe contact as a detector. The expected transverse field dependence of V_H is shown in Fig. 3.3(b). When M_i is flipped, P_0 changes sign, and V_H follows suite. However, if M_i is aligned along the y direction such that $P_0 \parallel y$, V_H would have the form shown in Fig. 3.3(c). We can control the direction of M_i by fabricating the device along different directions. The Fe in-plane easy axis is along the crystal [110] direction. Therefore if $x \parallel [110]$, $P_0 \parallel x$, and likewise, if $y \parallel [110]$, $P_0 \parallel y$.

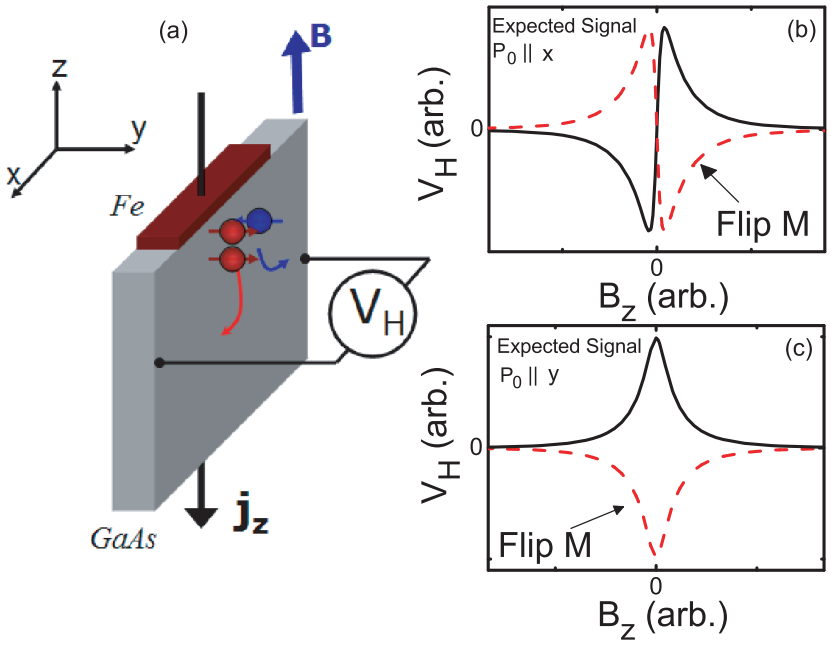

Figure 3.3: (a) Anomalous Hall effect measurement configuration. Spins are injected through an Fe/GaAs Shottky tunnel barrier contact. The Hall voltage is measured across the channel and a magnetic field is applied in the z direction. The direction of injected polarization P_0 is dependent on the orientation of the Fe injector magnetization. (b) Expected measured AHE signal as a function of transverse magnetic field for spins injected in the y direction, $P_0||y$. The dashed curve is the expected signal when the magnetization of the injector is flipped, such that $P_0||-y$. (c) Expected AHE signal when $P_0||\pm x$ as a function of applied transverse field.

Note that under forward bias, the diffusive and drift terms in Eq. 3.10 have opposite signs and therefore oppose each other. One might imagine that if we increased the current density sufficiently, under forward bias, the drift term will overcome the diffusive term, and V_H can change sign. This turns out not to be the case if we take into account that the spin diffusion length λ is also field dependent, as discussed in Sec. 1.2.1 and Fig. 1.1. For large forward bias $\lambda = \lambda_u \approx D/\mu E$. Putting this into Eq. 3.10, we find that $V_H = 0$ in the limit of large j for a forward biased contact. The spin current is therefore always flowing from the Fe contact into the GaAs channel, as expected, and V_H has the same sign, regardless of whether the injector is forward or reverse biased as long as the accumulated spin polarization does not change sign.

3.2.3 Spin Hall Effect (SHE)

In the AHE and the iSHE, a transverse charge current is induced by a spin polarized current. For the spin Hall effect on the other hand, a charge current induces a transverse spin current. This is represented by the term $q_{ij} = \gamma\mu n\varepsilon_{ijk}E_k$ in Eq. 3.7. The spin current results in spin accumulation, of opposite sign, at opposite edges of the sample. The SHE was observed, only recently by Kato *et al.* [10] in 2004. Their measurement is shown in Fig. 3.4. In their experiment, an electric field was applied along a GaAs channel. Spins accumulated at the edges of the sample were measured optically using a polar Kerr microscope. The measured Kerr rotation at opposite edges of the channel was of opposite sign, consistent with the SHE.

The spin accumulation at the sample edges can be determined by considering

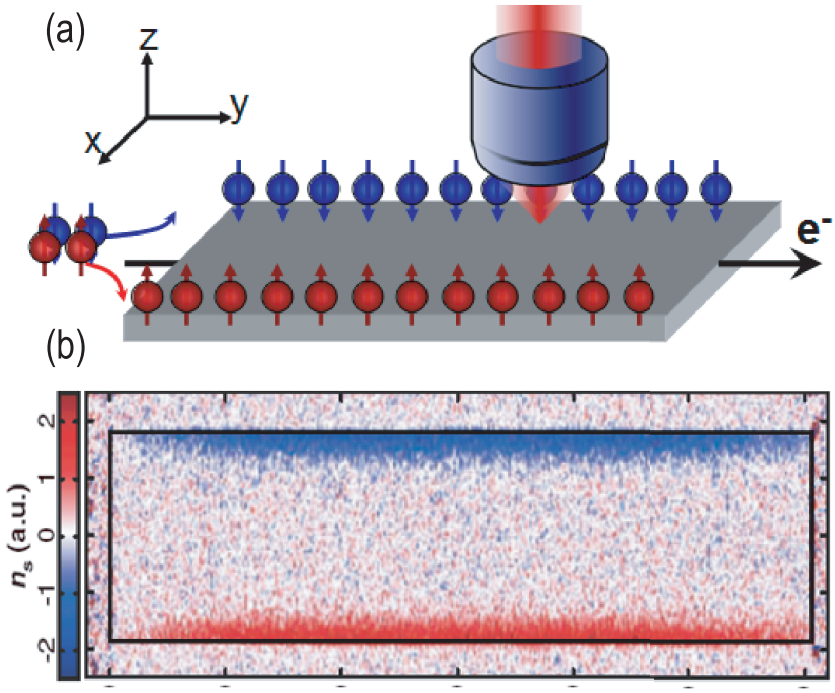

Figure 3.4: (a) Measurement configuration for optical detection of the spin Hall effect. Electric field is applied along the channel in the y direction. Spin polarization accumulates along the transverse edges. A Kerr microscope rasters across the sample, allowing for spatial dependent mapping of the z component of spin polarization. (b) Measured spin Hall signal using Kerr microscopy. The Kerr signal is of opposite sign on opposite transverse edges of the GaAs sample (from Ref. [10]).

the continuity equation (Eq. 3.8) and setting $\partial p_j/\partial t = 0$. We take the electric field along the y axis as shown in Fig. 3.4(a). The sample dimension in the x direction is wider than the spin diffusion length λ. The boundary condition should correspond to the vanishing of the spin current $q_{xj} = 0$. Following Ref. [96] we get the following boundary conditions from Eq. 3.7

$$\begin{aligned} \frac{dp_x}{dx} &= 0, \\ \frac{dp_y}{dx} &= 0, \\ \frac{dp_z}{dx} &= \frac{\gamma \mu n E_y}{D}. \end{aligned} \tag{3.13}$$

The spin polarization as a function of position relative to the edge is then given by

$$p_z(x) = -\frac{\gamma j_y \lambda}{eD} e^{-x/\lambda}, \tag{3.14}$$

$$p_x = p_y = 0. \tag{3.15}$$

where we have used $j_y = en\mu E_y$. The edge spin accumulation layer is approximately a spin diffusion length in width.

3.3 Microscopic Mechanism

Microscopically, spin-orbit interactions can be divided, roughly, into three classes. One of the first proposals to explain the SHE considered 'skew scattering', which is essentially the same as Mott scattering and is due to spin asymmetry in electron scattering due to the spin-orbit interaction.[96, 97] The 'side jump' mechanism, first proposed by Berger, is due to spin-dependent lateral displacement of electrons scattering off of impurities.[110, 111] Both skew scattering and side jump

mechanisms are typically considered extrinsic effects because they both involve impurity scattering. A diagram comparing the two effects is shown in Fig. 3.5. The 'intrinsic' mechanism was first proposed by Karplus and Luttinger [112] and is related to the spin-dependent band structure of the material in question.

3.3.1 Skew Scattering

The Hamiltonian for a spin 1/2 particle, including SO effects, is

$$H = \frac{\hbar^2 k^2}{2m^*} + V(\mathbf{r}) + \Lambda \boldsymbol{\sigma} \cdot (\boldsymbol{k} \times \nabla V), \tag{3.16}$$

where the last term represents the SO coupling. In vacuum $\Lambda = -\hbar^2/(4m_o^2c^2) \approx -3.7 \times 10^{-6}\text{Å}^2$, where m_0 is the bare electron mass and c is the speed of light. In a direct gap cubic semiconductor, the Kane model applied to conduction electrons within $\boldsymbol{k} \cdot \boldsymbol{p}$ theory results in $\Lambda = (P^3/3)\left[1/E_0^2 - 1/(E_0 + \Delta_0)^2\right]$.[113] E_0 is the band gap, Δ_0 is the SO splitting, and P is the properly normalized interband momentum matrix element. For GaAs $\Lambda = 5.3\text{Å}^2$, which is 6 orders of magnitude larger than the vacuum value. The Hamiltonian above can be written as[118]

$$H = \frac{1}{2m^*}\left(\hbar\mathbf{k} - e\mathbf{A}_{SO}\right)^2 + V(\mathbf{r}), \tag{3.17}$$

where we have defined

$$\boldsymbol{A}_{SO} \equiv \frac{m^*}{e\hbar}\Lambda\left(\boldsymbol{\sigma} \times \boldsymbol{\nabla} V\right). \tag{3.18}$$

We can then write an effective spin-dependent magnetic field, due to the SO interaction,

$$\mathbf{B}_{SO} = \boldsymbol{\nabla} \times \boldsymbol{A}_{SO} = \frac{m^*}{e\hbar}\Lambda\left(\boldsymbol{\nabla} \times (\boldsymbol{\sigma} \times \boldsymbol{\nabla} V)\right). \tag{3.19}$$

The SO field influences the conducting charge carriers in a similar way as an externally applied magnetic field. The SO field, however, is dependent on the

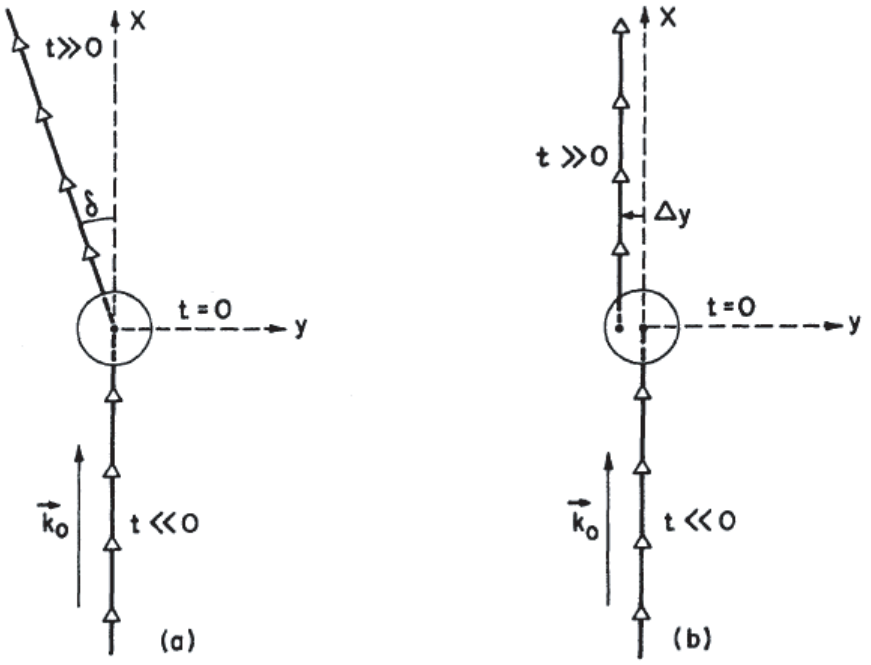

Figure 3.5: Diagram of average electron motion before and after scattering by a central potential in the presence of spin-orbit scattering. The spin is along the z direction. The incident electron has $k_0 \parallel x$. Skew scattering is shown in (a) and side jump is shown in (b). The deflection angle δ and the lateral displacement of the wavefunction (side jump) Δy of an electron upon scattering from an impurity are spin-dependent. These two effects are usually both active. Figure is from Ref. [110]

spin polarization of the carrier. In order to obtain a non-zero B_{SO}, $\nabla_i \nabla_j V$ must be non-zero, on average. The SHE therefore requires spatial inhomogeneity of the electric potential. This can be due to the Coulomb potential of impurity atoms from which the charge carriers scatter [110, 113, 115, 116] or the from the crystal field.[118]

In the extrinsic mechanism for the SHE, the spin-orbit (SO) interaction of the bulk crystal produces a SO contribution to the impurity potential. Engel *et al.* [113] showed that scattering from charged impurities can reasonably reproduce the experimentally determine spin Hall conductivity observed by Kato *et al.*[10]

Engel *et al.* calculated the SO scattering parameter due to skew scattering, γ_{ss} (using the Boltzmann equation) to be

$$\gamma_{ss} = \frac{1}{2} \frac{\int d\Omega I(\vartheta) S(\vartheta) \sin \vartheta}{\int d\Omega I(\vartheta)(1 - \cos \vartheta)}. \tag{3.20}$$

$I(\vartheta)$ is the spin independent part of the scattering cross section. It was calculated for an exponentially screened impurity potential in the second order Born approximation using the Dalitz formula.[114] $S(\vartheta)$ is known as the Sherman function, and measures the polarization of outgoing particles scattered into direction **k** from an unpolarized incoming beam of momentum **k**'.[114] The SO coupling parameter Λ is incorporated into $S(\vartheta)$. They find that (note that the value here is 1/2 of the value cited in Ref. [113] because they have defined γ as 2 times the definition given in Eqs. 3.6 and 3.7)

$$\gamma_{ss} = 5 \times 10^{-4}. \tag{3.21}$$

This yields $\sigma_{SH} \equiv \gamma \mu n \approx 1.7\ (\Omega\mathrm{m})^{-1}/|e|$ for a GaAs sample with $\sigma = 3 \times 10^3\ (\Omega\mathrm{m})^{-1}$. σ_{SH} is defined from Eq. 3.7 such that $\sigma_{SH} \equiv -q_{yz}/E_x$. $|e|\sigma_{SH}$ is approximately 0.1% of σ. This value is within the experimental error in Ref. [10].

Abakumov and Yassievich performed a similar calculation in the second order Born approximation.[115] From their results, we can approximate γ_{ss} by

$$\gamma_{ss} \sim \frac{\Lambda k_F}{a_0^*}, \tag{3.22}$$

where k_F is the Fermi wave vector and $a_0^* = \hbar^2\epsilon/m^*e^2$ is the Bohr radius, where ϵ is the effective dielectric constant. For bulk GaAs with $n = 5 \times 10^{16}$ cm^{-3}, we get $\gamma_{ss} \sim 2 \times 10^{-4}$, which is comparable to the value calculated by Engel *et al.*[113]

3.3.2 Side Jump

The side jump mechanism was proposed by Berger [110] and describes the lateral displacement of the electron wave packet during each scattering event. In order to derive the side jump contribution to the SHE, we write down the equation of motion from Eq. 3.16:

$$\dot{\mathbf{r}} = \frac{\partial H}{\partial \mathbf{p}} = \frac{\mathbf{p}}{m} + \frac{2\Lambda}{\hbar}\left(\nabla V \times \mathbf{s}\right), \tag{3.23}$$

where $\mathbf{p} = \hbar\mathbf{k}$ and $\mathbf{s} = \boldsymbol{\sigma}/2$. The second term above is the anomalous velocity due to SO interaction. Following Nozières and Lewiner [116], we can substitute to first order of SO interaction $\dot{\mathbf{p}} = -\nabla V$. Then, integrating over time, and assuming $\mathbf{s}$ is constant, we arrive at the lateral displacement[113]

$$\delta\mathbf{r} = \frac{4\Lambda}{\hbar}\left(\mathbf{s} \times \delta\mathbf{p}\right), \tag{3.24}$$

where $\delta\mathbf{p} = \mathbf{p}' - \mathbf{p}$ is the change in electron momenta before and after the collision. Note that an additional factor of 2 was included in $\delta\mathbf{r}$ to account for corrections to the coordinate operator when SO coupling is taken into account.[113, 117]

For spin polarized current, the resultant anomalous Hall charge current (transverse current) is given by

$$\mathbf{j} = en\frac{\delta \mathbf{r}}{\tau}, \tag{3.25}$$

where τ is the impurity momentum scattering time. From the lateral displacement in Eq. 3.24, the momentum dissipated per scattering event $\delta \boldsymbol{p} = -e\boldsymbol{E}\tau$, and $\langle \boldsymbol{\sigma} \rangle = \boldsymbol{P}$, we arrive at

$$\boldsymbol{j} = -\frac{2e^2 n}{\hbar}\Lambda(\boldsymbol{P} \times \boldsymbol{E}). \tag{3.26}$$

By comparing to the third term in Eq. 3.7, we determine the side jump contribution to SO coupling[113]

$$\gamma_{sj} = \frac{2e}{\hbar\mu}\Lambda. \tag{3.27}$$

Note that, for electrons, $\gamma_{sj} < 0$, which is the opposite sign as γ_{ss} determined in Ref. [113]. The side jump and skew scattering mechanisms contribute opposite signs to the total SO coupling. For our typical n-GaAs samples, $\mu \sim 1$ m$^2/Vs$, and using $\Lambda = 5.3$ $\mathring{A}^2$ [113] we estimate $\gamma_{sj} \approx -2 \times 10^{-4}$ which is of the same order of magnitude as γ_{ss}.

3.3.3 Intrinsic

The intrinsic contribution to SO coupling arises even in the absence of impurities. It is caused by spin splitting of the conduction band. In bulk III-V semiconductors with bulk inversion asymmetry (BIA), such as GaAs, the conduction band Hamiltonian has the following Dresselhaus term[74]

$$H_D = ß\boldsymbol{\kappa} \cdot \boldsymbol{\sigma}, \tag{3.28}$$

where $\boldsymbol{\sigma}$ are the Pauli spin 1/2 matrices, ß $\approx 27\ eV\mathring{A}^3$ [119], and

$$\boldsymbol{\kappa} \equiv \left[k_x(k_y^2 - k_z^2), k_y(k_z^2 - k_x^2), k_z(k_x^2 - k_y^2)\right]. \tag{3.29}$$

ß$\boldsymbol{\kappa}$ acts as an internal momentum dependent magnetic field, which results in the spin Hall effect. Bernevig and Zhang have calculated the Dresselhaus contribution to the SHE and arrived at a range of values $e\sigma_{SH} = 0.02\ (\Omega m)^{-1}$ to $0.2\ (\Omega m)^{-1}$ for the dirty to clean limits.[120] The experimentally determined value by Kato *et al.* is within this extremely large range.[10]

3.4 Measurement of Spin-Dependent Hall Effect

We have demonstrated in Chapter 1 that we are able to inject non-equilibrium spin polarization into *n*-GaAs electrically through a Fe/GaAs Schottky tunnel barrier. The non-equilibrium spin polarization was then detected with another Fe contact. SO effects, particularly the AHE and iSHE, can allow us to measure the spin polarization without the use of a separate Fe contact. Additionally it can provide insight into SO interactions in GaAs.

3.4.1 Device Design

In order to measure the SO coupling we will employ the method shown in Fig. 3.3. We have fabricated devices with the general structure shown in Fig. 3.6(a) and (b). The channel on the left and right of the Fe contact is etched down to create a trench. This forces the electric current to flow vertically. Note, however that the channel thickness is $\approx 2.5\ \mu$m while the Fe contact width is $\approx 5\ \mu$m. The trench can be etched down about 1.7 μm. We have also used devices with a channel

thickness of 5 μm, in which case the trench was 4 μm deep. We have found, however, that the spin Hall measurements did not change significantly when a trench is not fabricated. Because the Fe contact is located on top of the channel, the total current flowing in the z direction is always just the applied bias current. We will assume that the current density is I/A where A is the Fe contact area. Thin Hall arms ($\sim 1\mu$m wide) are defined along the crystal [110] direction (Fe easy axis). Fig. 3.6 shows a closeup of the device. Note that the Hall arms are obscured from the top by the Au leads which contact the Fe injector. The Hall arms are contacted many spin diffusion lengths away from the injector by large Fe pads, which in turn are connected to Au leads. A SiN insulating layer is used to isolate the Au leads from the GaAs channel and Hall arms. For the spin Hall experiments, the Fe injector is current-biased from both sides of the channel. This reduces the lateral flow of electrons (which can produce a rather large background ordinary Hall voltage that can obscure the spin signal) and increases the spin polarization under the Fe injector. By careful design of the relative sizes of the Hall arms, Fe contacts and channel widths, we are able to eliminate most background effects that are due to inhomogeneity of the electric field.

3.4.2 Odd Spin-Dependent Hall Signal

For the measurement configuration shown in Fig. 3.6(a), the expected spin-dependent Hall voltage (we will refer to this as the SDH signal from now on, since the AHE and iSHE are both active in this measurement) as a function of applied transverse field is shown in Fig. 3.3(b). The Fe easy axis [110] is in the x direction, so the injected spin polarization is along the x direction, $P_0 \parallel x$. The expected signal

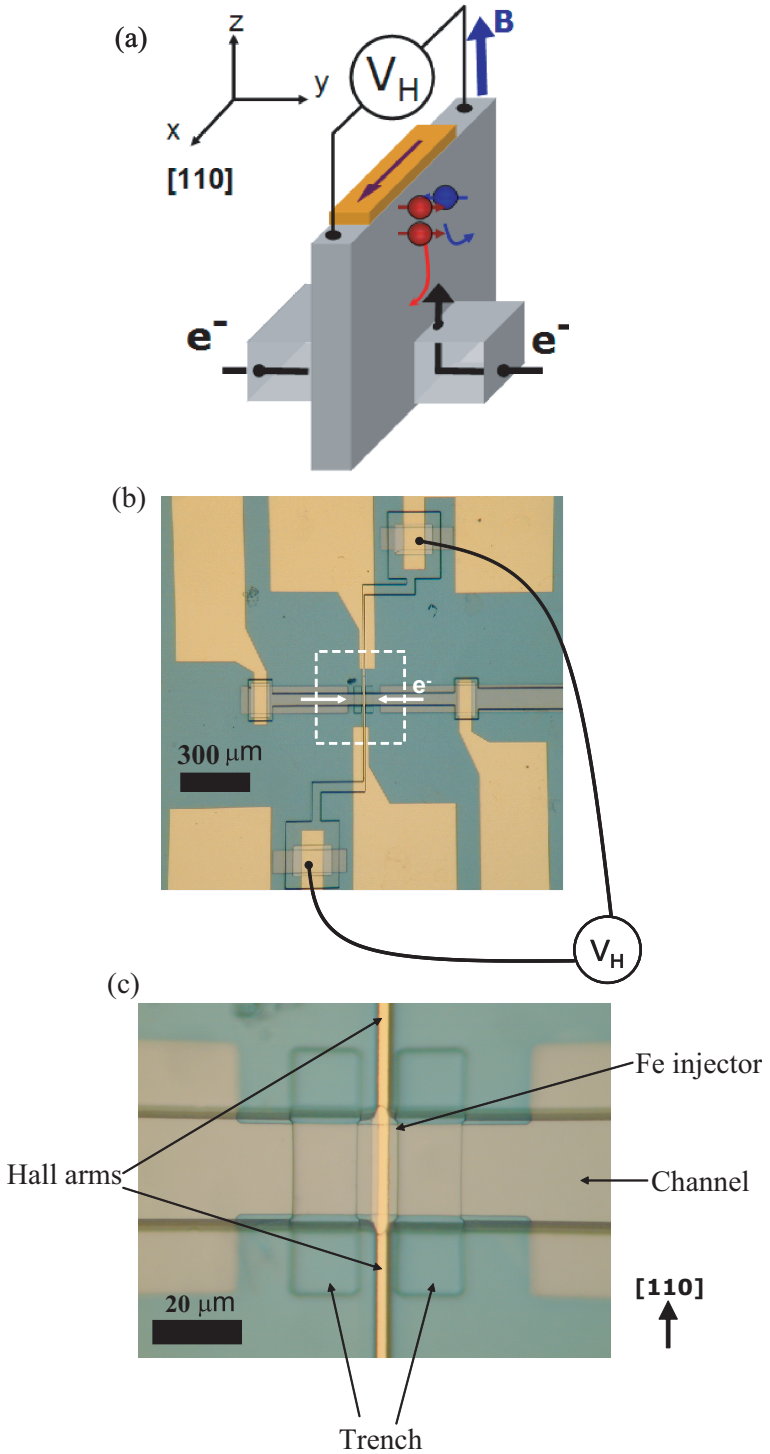

Figure 3.6: (a) Schematic of the device design used for AHE measurements in Fe/GaAs heterostructures. (b) Optical micrograph of device Q59-10 fabricated for even AHE measurements. The Fe easy axis is the crystallographic [110] direction. The region bounded by the dashed box is shown schematically in (a) and expanded in (c). (c) Closeup of a device used for AHE measurements.

is 'odd' with respect to the applied transverse field. We thus refer to it as the odd SDH signal. Fig. 3.7(a) shows the measured Hall signal for a forward biased (electrons tunneling from GaAs into Fe) contact as a function of magnetic field applied along the z direction. The Fe contact is 5×75 μm^2 in size. The GaAs channel is doped nominally at 5×10^{16} cm^{-3}. We observe a ≈ 3 mV offset and a small slope. Most strikingly we also observe a horizontal "S" shaped feature centered around 0 Oe. The solid squares and open circles correspond to $M_i \,||\, \pm x$. When the magnetization of the injector is switched, the SDH signal should switch sign. The offset and slope are not affected by flipping M_i, and are therefore presumed to be spin independent, while the "S" shaped feature does switch sign. We subtract the spin independent linear background from the data in Fig. 3.7(a) to extract the SDH signal shown in Fig. 3.7(b). The result agrees qualitatively quite well with expectation (see Fig. 3.3(b)).

We can estimate the SO coupling parameter γ from the size of the SDH signal with Eq. 3.10. Using $w = 75$ μm, $n = 5 \times 10^{16}$ cm^{-3}, $j = 2 \times 10^6$ A/m^2, $P = 0.1$, as well as μ, ρ, and λ determined from charge and spin transport measurements in Chapter 1, we find that

$$\gamma \approx 1 \times 10^{-2}, \tag{3.30}$$

which is approximately 2 orders of magnitude larger than that determined experimentally [10] and calculated theoretically for extrinsic mechanisms.[113] Even if we set $P = 1$, our measured γ would still be an order of magnitude larger than previously estimated values. The large discrepancy suggests that we are observing a manifestation of a different mechanism for the SHE than the extrinsic mechanisms previously discussed.

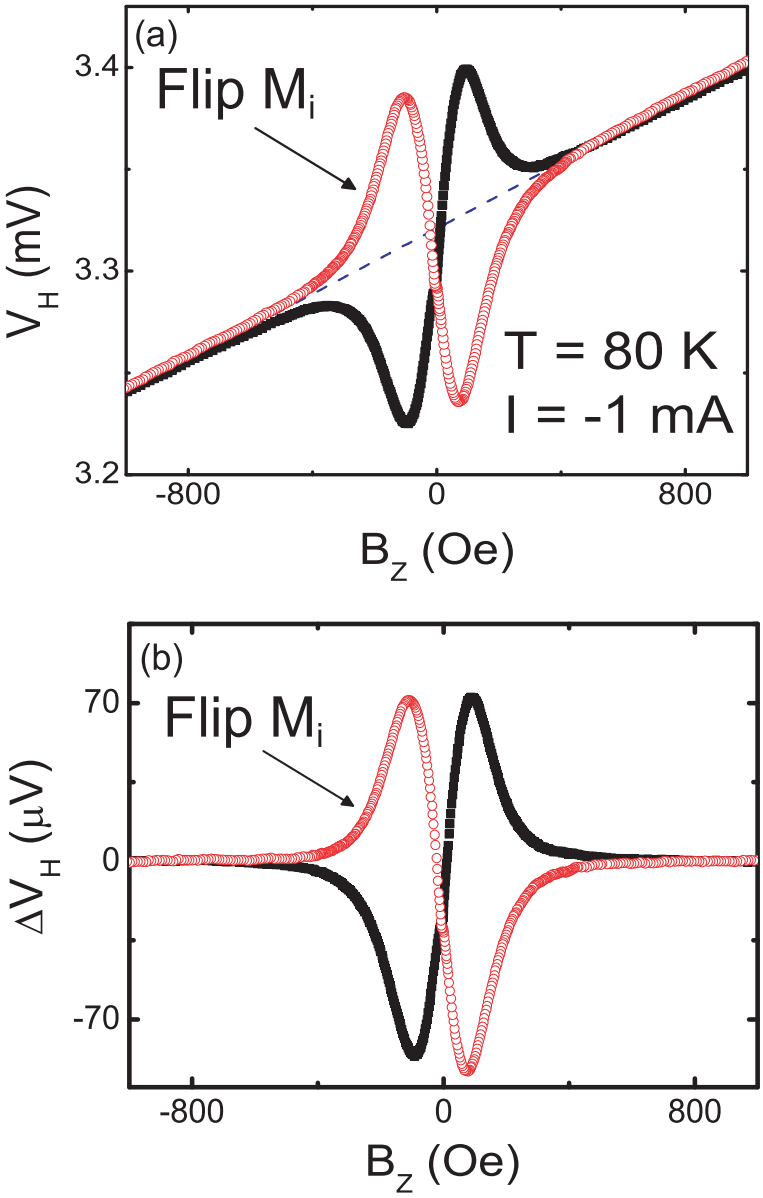

Figure 3.7: (Q62-1) (a) Hall signal measured in the configuration shown in Fig. 3.6(a). The open circles and closed squares are field sweeps taken with M_i in opposite direction. The dashed line is the spin *independent* background. (b) The spin-dependent Hall signal obtained by subtracting the spin independent component from (a).

3.4.3 Bias Dependence of the Spin-Dependent Hall Signal

Fig. 3.8 shows the SDH Hanle curves measured at low temperatures ($T = 20$ K) for various biases. Curves for injector magnetization in opposite directions are shown. We observe severe distortion of the SDH curves at high bias. This can be attributable to the strong hyperfine field B_n at low temperatures and large P. The measured 3T Hanle curves for the same temperature are shown in Fig. 3.9. We see that besides the peak at $B_z = 0$ Oe, there is a satellite peaks on both sides of 0 Oe. As was discussed in Sec. 2.3, the hyperfine field results in a narrowing of the observed Hanle curve width. However, a sufficiently large B_n can result in the appearance of the two satellite peaks (which are due to cancelation of the applied field by the hyperfine field) observed in Fig. 3.9. This effect has also been observed in optical orientation experiments.[6, 87] Ideally, the 3T Hanle curve should be perfectly symmetric about $B_z = 0$ Oe. However, slight misalignments (we estimate $\lesssim 0.5^o$) of the applied magnetic field from the z direction can result in the observed asymmetry. When the injector bias is reduced, the electron spin polarization and consequently B_n is also reduced. Therefore, the low bias 3T Hanle curve ($V_{int} = -0.1$ V shown in Fig. 3.9) does not exhibit the two satellite peaks. The distortion in the 3T electron spin signal as a function of B_z under high bias is reflected in the SDH signal which presents two extrema on either side of 0 Oe.

Going from forward bias to small reverse bias, the SDH signal changes sign, as shown by the SDH curve for $V_{int} = 0.2$ V in Fig. 3.8. The sign switches once again at high reverse bias (see the $V_{int} = 0.5$ V curve). Fig. 3.10(a) shows the summary of injector bias dependence of the odd SDH signal for injector magnetization

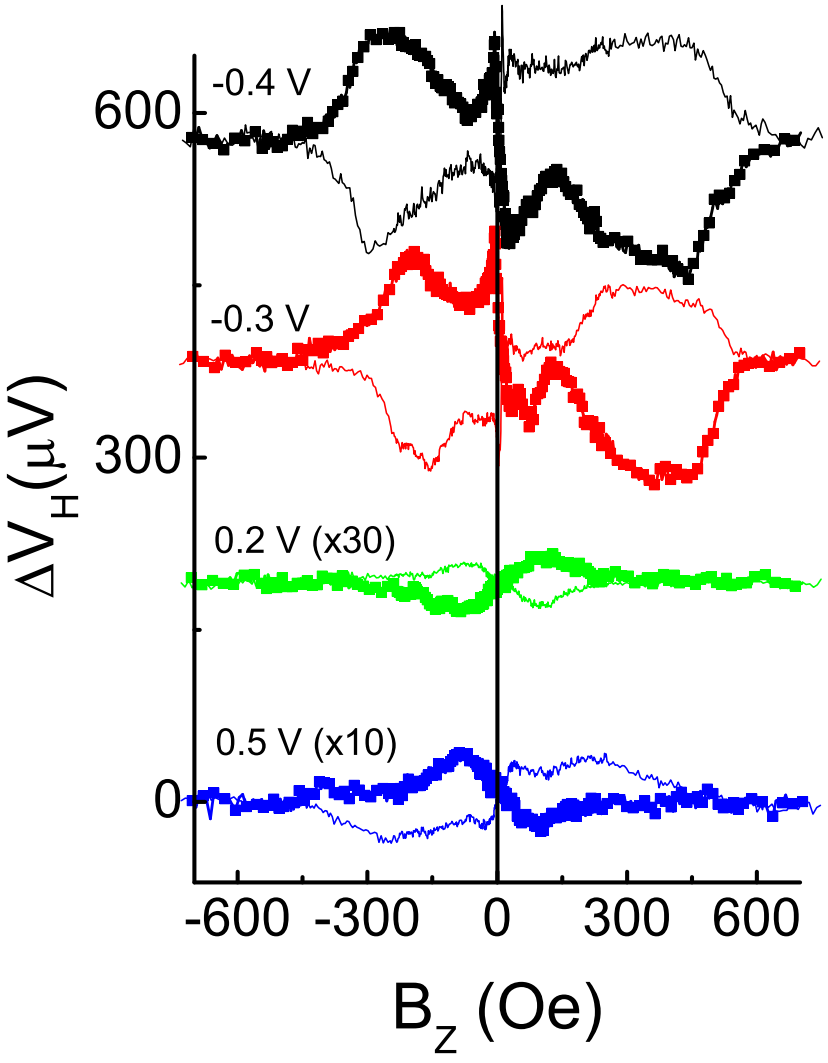

Figure 3.8: (Q59-9) Odd spin-dependent Hall Hanle curves for various injector biases. Symbols and lines are measurements for injector magnetization pointing in opposite directions. $T = 20$ K. Curves of different biases are offset vertically for clarity. Injector contact size is 5×75 μm^2.

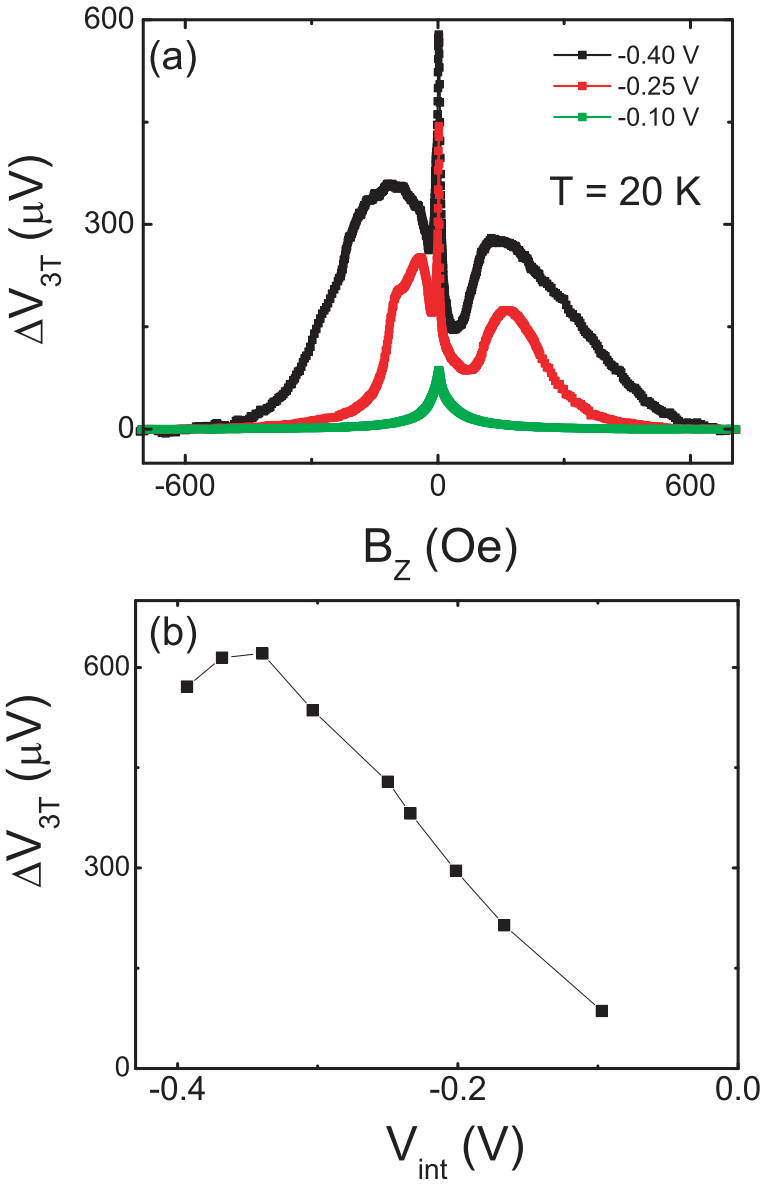

Figure 3.9: (Q59-9) (a) Hanle curves measured in the three terminal configuration for various injector biases. (b) Summary of the bias dependence of the 3T Hanle peak magnitude. Injector contact size is 5×75 μm^2.

$M_i||\pm x$. As demonstrated in Fig. 3.8(a), the SDH signal for the two magnetization directions are mirror images of each other. The size of the signal is extracted from taking the voltage difference between the minimum and maximum values of the ΔV_H curves shown in Fig. 3.8. As a comparison, the bias dependence of the non-local spin valve NLSV signal is displayed in Fig. 3.10(b). Both the SDH signal and the NLSV signal increases with increasing forward bias, change sign at small reverse bias, then changing sign once again at high reverse bias. As was discussed in Sec. 1.6.3, majority spin polarization is accumulated in the GaAs channel under large forward and reverse biases, while minority spin polarization is accumulated in the small injector bias window ($0\ V < V_{int} < 0.3\ V$ for this particular device) where the NLSV signal changes sign. The sign change of the SDH signal within this bias window reflects the change in sign of injected spin polarization. As discussed in Sec. 3.2.2 the direction of spin current for the device design used in this experiment is always away from the Fe/GaAs interface regardless of the sign of V_{int}. The sign of the bias current is therefore relevant to the sign of the SDH signal only in so far as it changes the sign of the accumulated spin polarization. The decrease of the NL and 3T signal at large forward bias is attributable to the decrease in spin injection efficiency observed previously in the detector bias experiment in Sec. 1.6.3.

3.4.4 Even Spin-Dependent Hall Signal

We have also fabricated devices such that the Fe easy axis is along the y axis as shown in Fig. 3.11. In such a device, $P_0 \parallel y$, and the expected SDH signal is maximum at and symmetric about $B_z = 0$ Oe, as shown in Fig. 3.3(c).

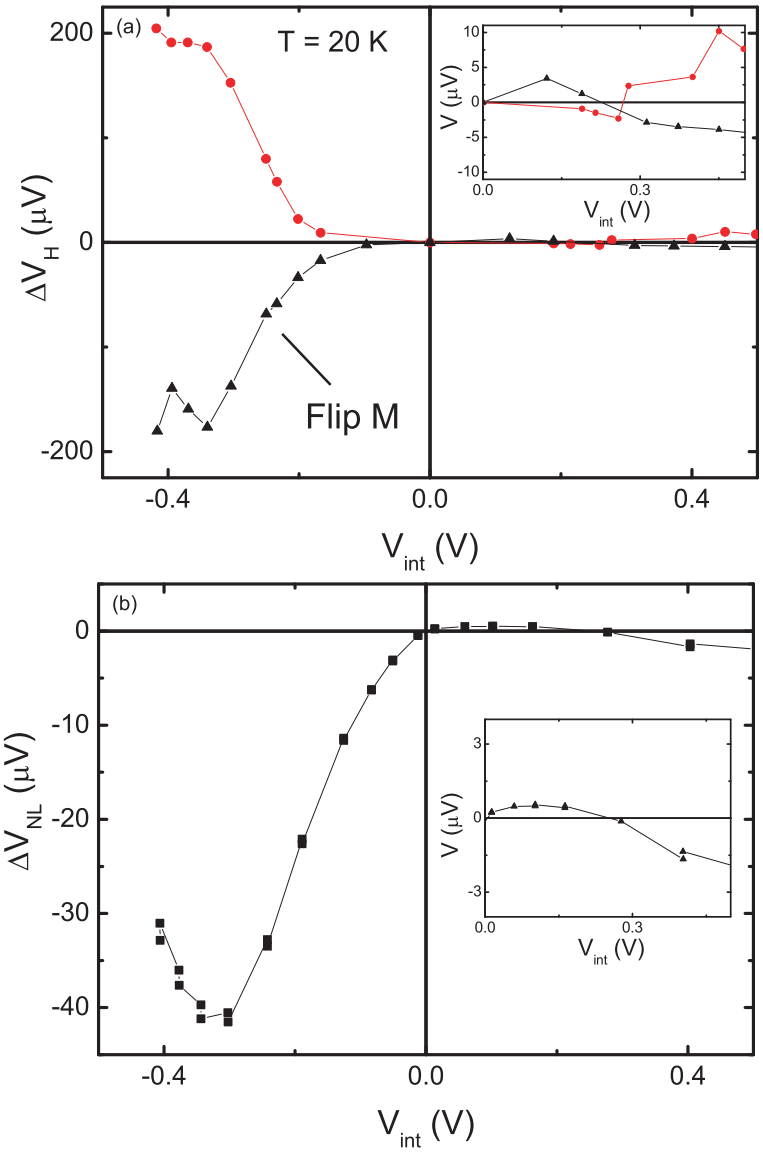

Figure 3.10: (Q59-9) (a) Bias dependence of the spin-dependent Hall SDH signal measured at $T = 20$ K. Circles and triangles represent measurements with the injector magnetization pointing in opposite directions. Inset shows a closeup of the SDH signal with a reverse biased injector. (b) Bias dependence of the non-local spin valve NLSV signal measured at $T = 20$ K. Injector and detector sizes are 8×38 μm^2 and 5×38 μm^2 with a 10 μm center to center gap. Inset shows a closeup of the NLSV signal with reverse biased injector.

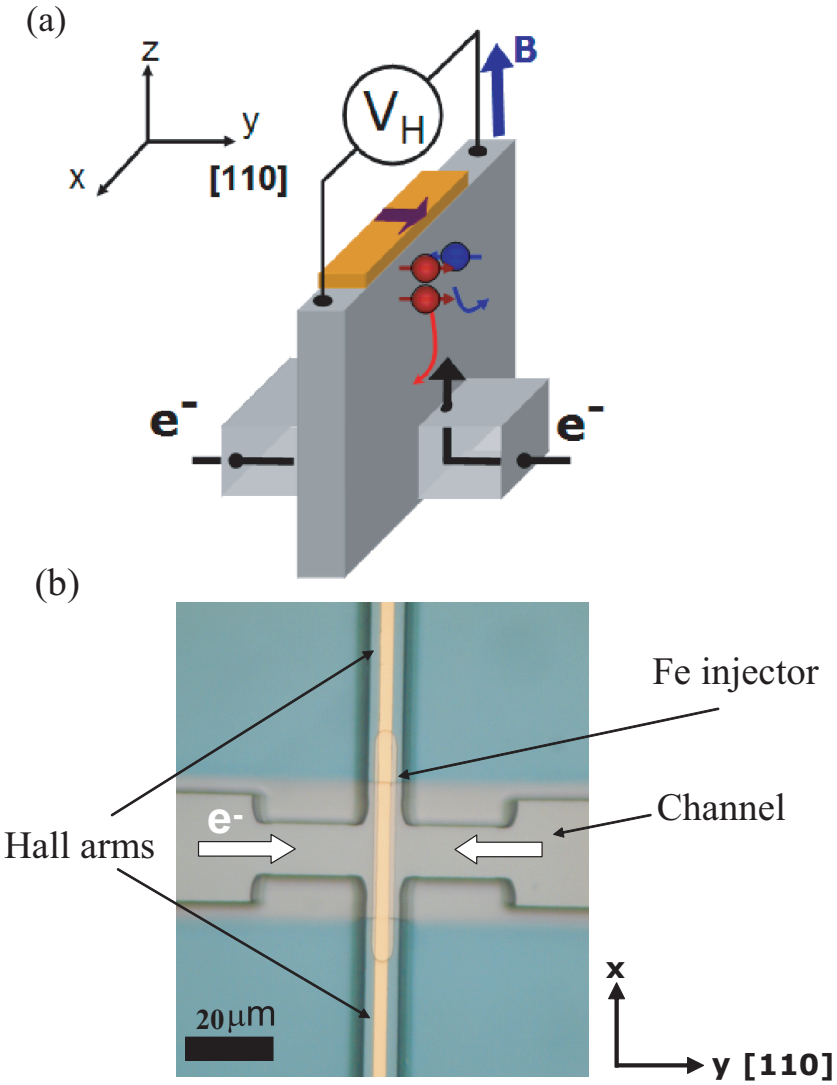

Figure 3.11: (Q59-10) (a) Schematic of device used to measure the even spin-dependent Hall signal. The Fe easy axis is now along the y axis. (b) Optical micrograph of device Q59-10 fabricated for even AHE measurements. The easy axis is along the y direction. Note that no trench was fabricated for this particular device, but the Fe contact is still elevated by ≈ 100 nm above the channel. Samples with trenches were also fabricated.

Fig. 3.12 shows the surprising measured field dependence of the Hall signal. A linear background is subtracted from the Hall data to extract the SDH signal shown in Fig. 3.12(b). Although ΔV_H is symmetric about $B_z = 0$ Oe, the magnitude of the signal is not at a maximum there. Instead, a broad valley is observed, with a small peak in the center. Flipping M_i switches the sign of ΔV_H, as expected for a spin-dependent signal. The Fe injector used is 5×75 μm^2 in size. The even SDH signal is, just as the odd SDH signal, much larger than what one would expect from the extrinsic spin Hall effect. The discrepancy between the expected and measured shape of the even SDH Hanle curve is an indication that the SDH signal is not sensitive solely to the electron spin polarization.

3.4.5 Hyperfine Effects and the Spin-Dependent Hall Signal

In Sec. 2.6 we presented a method to suppress the nuclear field, and thus eliminate hyperfine effects from the measured Hanle curves. As a reminder: the field cycling procedure proceeds by first suppressing the nuclear field by applying an AC magnetic field of frequency between 1-5 kHz while the DC applied field $B_z \approx 0$ Oe. B_z is then ramped quickly to the measurement field, where it stays for time $T_{measure}$. We take a measurement before the nuclear field builds up, and then ramp back to $B_z \approx 0$ Oe. The procedure is repeated for each data point on the Hanle curve. We will apply the same field cycling procedure to eliminate the hyperfine effects in the observed SDH signal.

Fig. 3.13(a) shows the 3T Hanle curve (see Sec. 1.5.2) measured at approximately steady state. The distortion of the Hanle curve is a result of a strong

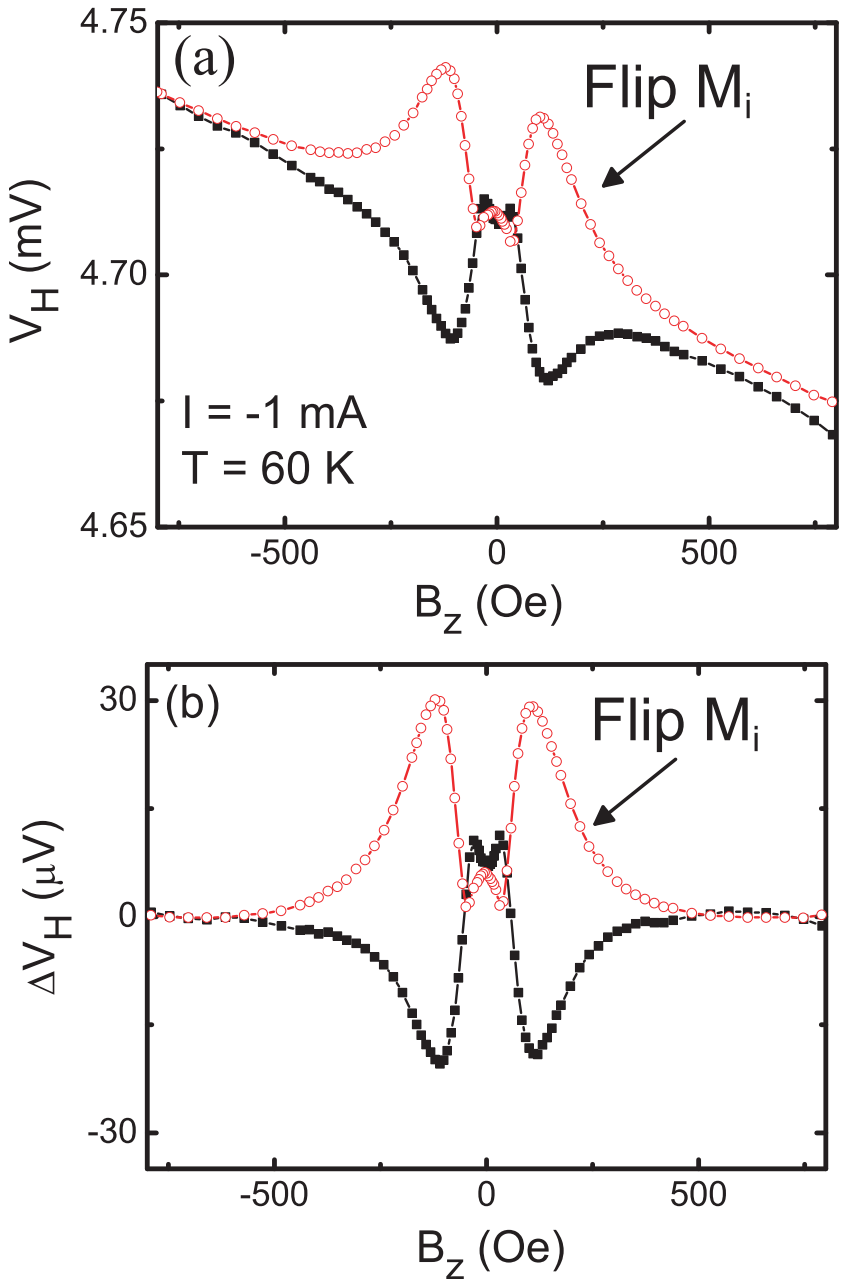

Figure 3.12: (Q59-10) (a) Measured Hall signal as a function of applied field in the z direction for $P_0 \parallel y$. Solid squares and open circles are for M_i in the $\pm y$ directions. (b) The spin-dependent part of the Hall signal shown in (a) after a linear background is subtracted.

hyperfine field, B_n. The measurement implementing B_n suppression is shown for the subsequent curves in Fig. 3.13(a) with decreasing $T_{measure}$. In general, the larger $T_{measure}$ is, the more time B_n has to build up. We can see, however that even for $T_{measure} = 10$ s, the hyperfine features are essentially eliminated. As $T_{measure}$ is decreased further down to 0.7 s, no significant changes in the Hanle curve are observed. Note the magnitude of the measured 3T signal peak does not change appreciably as the nuclear field elimination is applied.

If the SDH signal is dependent on only the electron spin polarization, we would expect that application of the nuclear field elimination procedure should produce a cleaner odd Hanle curve (in the case when $P_0 \parallel x$), but no change in the magnitude of the maximum signal. Fig. 3.13(b) shows the steady state odd SDH signal measured at $T = 60$ K. The Hanle curve is distorted due to hyperfine effects. Also shown are the SDH Hanle curves when B_n is suppressed. Just as in the case of the 3T measurement, the SDH signal becomes more symmetric. However, the magnitude of the SDH signal decreases with greater B_n suppression. For the greatest B_n suppression shown here, i.e. smallest $T_{measure}$, the SDH signal is only $\approx 10\%$ of the maximum steady state value. This is conspicuously counter to the electron spin signal as measured in the 3T configuration, which always maintains its maximum peak height when B_n elimination is employed. Fig. 3.14(a) shows an example where the SDH signal is fully eliminated through elimination of the hyperfine field. Additionally, nuclear field elimination results in a similar suppression of the *even* SDH signal, as shown in Fig. 3.14(b).

The major implication of the measurements shown in Fig. 3.13 is that the SDH Hall signal magnitude is related intimately to the nuclear spin polarization. In

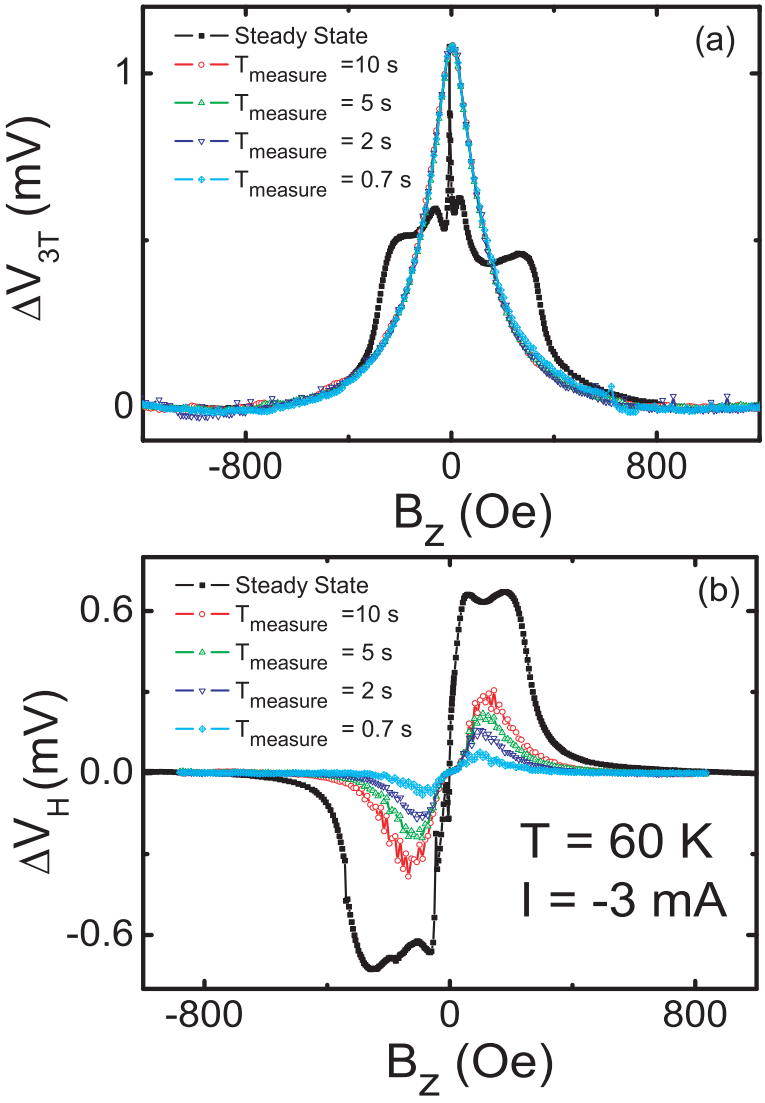

Figure 3.13: (Q62-1) (a) Hanle curves in the three terminal configuration measured at steady state (black closed squares) and with the nuclear field elimination procedure using varying measurement times $T_{measure}$. The injector contact is 5×75 μm^2. $T = 60$ K and the applied bias is -3 mA. (b) Measured odd spin-dependent Hall signal (black closed squares) and with nuclear field elimination procedure with varying $T_{measure}$. The injector contact is the same as that used in (a).

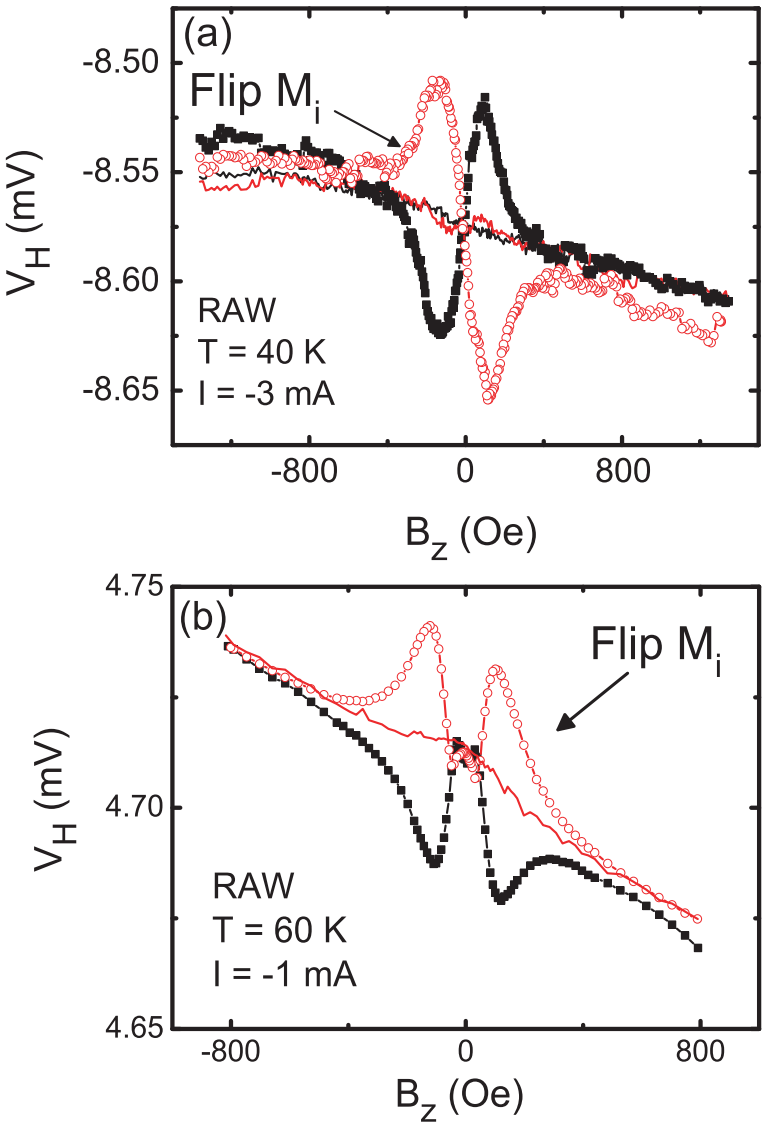

Figure 3.14: (a) (Q13-MC) Hall signal V_H for a device with $P_0 \parallel x$ measured without B_n elimination (scatter plots) and with B_n elimination (solid lines). Note that the linear background has not been subtracted from this data. Data for $M_i \parallel \pm x$ is shown. (b) (Q59-10) Hall signal V_H for a device with $P_0 \parallel y$ measured without B_n elimination (scatter plots) and with B_n elimination (solid line). The B_n-suppressed curve was measured for only one M_i direction. $T_{measure} = 0.5\ s$ for the B_n suppression measurements.

Chapter 2 we discussed how the electron spin dynamics, and thus the measured spin signal using Fe contacts, is affected by the hyperfine field. The hyperfine interaction was incorporated in the calculations of the electron spin dynamics by simply adding B_n to the applied field, such that the total field $B_{tot} = B + B_n$. The measurements using an Fe detector were responsive to changes in the *nuclear* spin polarization only indirectly, viz. through the precession of the electron spins about the hyperfine field. Fig. 3.13(b) demonstrates that the magnitude of the SDH signal is sensitive *directly* to the nuclear spin polarization.

3.4.6 Temperature Dependence of the Spin-Dependent Hall Signal

Fig. 3.15(a) shows the temperature dependence of the odd SDH signal magnitude. The SDH signal initially increases with increasing temperature, peaks at approximately $T = 60\ K$ and then decreases precipitously, disappearing above 120 K. As a comparison, the temperature dependence of the GaAs spin polarization represented by the 3T signal measured on the same device is also shown in Fig. 3.15. The 3T signal decreases with increasing temperature, but persists up to $T = 200$ K. The disappearance of the SDH signal above 120 K, despite the persistence of electron spin polarization, is correlated to the suppression of dynamic nuclear polarization. As discussed in Sec. 2.4, hyperfine effects on electron spin dynamics are no longer observed above 120 K in this sample due to the delocalization of donor electrons. The fact that the SDH signal is not observed above 120 K is consistent with the assertion made in the previous section that the nuclear spin polarization plays an integral part in the SDH signal.

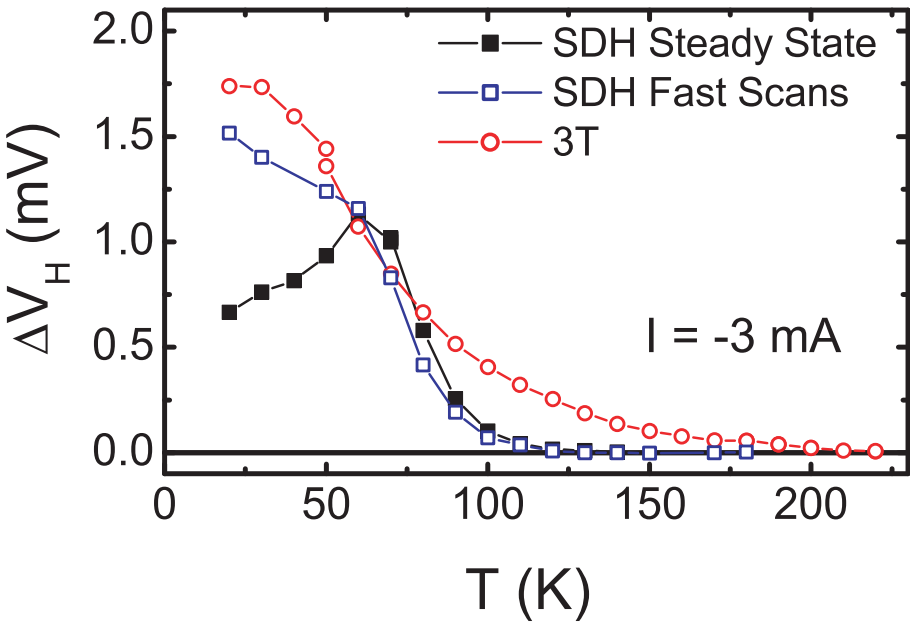

Figure 3.15: (Q62-1) Temperature dependence of the magnitudes of the spin-dependent Hall SDH signal measured in approximate steady state (solid squares) and non steady state conditions (open squares). Temperature dependence of the three terminal 3T signal is also shown (open circles).

Fig. 3.16 shows the odd SDH Hanle curves as a function of temperature. At low temperatures, measurements were performed very slowly ($\approx$ 60 s per data point) in order to approximate steady state conditions. Severe distortion of the SDH Hanle curves (multiple peak structure) occurs at $T \leqslant 60$ K. The distortion is attributable to the large nuclear field at lower temperatures as discussed in Sec. 3.4.3. Note also that the decrease in the steady state SDH signal with decreasing temperature (below 60 K) shown in Fig. 3.15 coincides with the appearance of the multiple peaks. We believe that this decrease in the SDH signal is due to spatial inhomogeneity of the nuclear spin polarization and thus the nuclear field. This results in only partial compensation of the applied magnetic field at the peak positions, which are located at non zero applied fields. The argument is the same

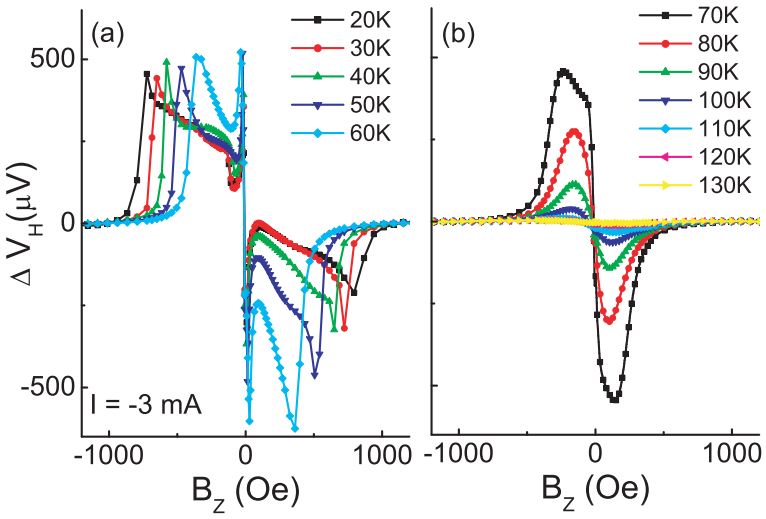

Figure 3.16: (Q62-1) Odd SDH Hanle curves as a function of temperature.

as that used to explain the height of satellite peaks measured in the oblique Hanle configuration in Sec. 2.3 (see Fig. 2.11 and discussion of it). If we measure the SDH signal quickly (in non-steady state conditions), the low field peak increases in magnitude significantly. The SDH signal size for these fast scans continues to increase as the temperature is lowered, as shown by the open squares in Fig. 3.15. We therefore believe that the low temperature decrease in the SDH signal is due to the large spatially inhomogeneous hyperfine field and not to an actual decrease of spin polarization. Note that this spatial inhomogeneity does not effect the zero field peak magnitude of the the 3T and NL Hanle curves because $B_n = 0$ when $B = 0$.

We can show, conclusively, that the measured Hall signal is spin-dependent by performing NMR measurements. Fig. 3.17 shows NMR spectra measured in the SDH configuration. The Hall signal was monitored while the frequency of an AC magnetic field was swept. A constant field of $B_z = 160$ Oe was applied. Clear

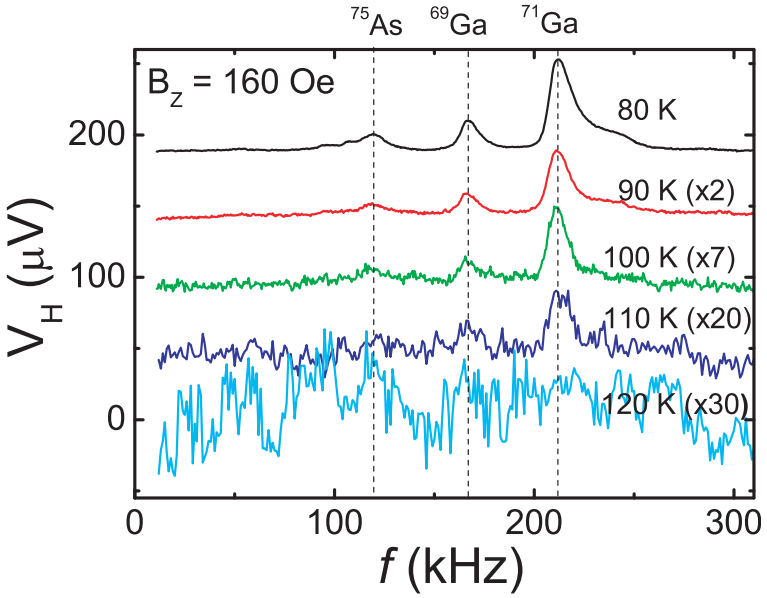

Figure 3.17: (Q62-1) Nuclear magnetic resonance (NMR) spectra of the spin-dependent Hall signal measure for various temperatures.

NMR signatures of GaAs nuclei are observed. This measurement definitively excludes all non-spin-dependent explanations for the data such as 'local' Hall effects, or magneto-resistance of the Fe contact. Note that the NMR signal disappears at $T = 120$ K, consistent with the temperature dependence of the SDH signal.

3.4.7 Phenomenological Expression for the Spin-Dependent Hall Signal

In the previous section, we have demonstrated that the magnitude of the SDH signal is sensitive to the nuclear spin polarization. It is naturally therefore to ask if the *electron* spins play a role beyond polarizing the nuclei through DNP. Additionally, the phenomenological expressions for SO effects written in Eqs. 3.6 and 3.7 do not include a hyperfine term. We would therefore like to determine

the phenomenological form of the SDH effect we measure.

Towards this end, we compare the measured even and odd SDH signals shown in Figs. 3.7 and 3.12 to the electron spin and nuclear spin polarizations. Fig. 3.18 shows the spin polarization $\mathbf{S}$ and nuclear field $\boldsymbol{B}_n$ calculated using the CN method (see Sec. 2.2.1) and the general spin transport equation:

$$\frac{\partial \mathbf{S}}{\partial t} = -v_d \frac{\partial \mathbf{S}}{\partial y} + D\frac{\partial^2 \mathbf{S}}{\partial y^2} - \frac{\mathbf{S}}{\tau_s} - \boldsymbol{\Omega}_L \times \mathbf{S}, \tag{3.31}$$

where v_d, D, and τ_s are the drift velocity, diffusion constant, and spin lifetime; $\Omega_L = g^* \mu_B \mathbf{B}_{tot}/\hbar$ is the Larmor frequency, $g^* = -0.44$ is the electron g-factor in GaAs, μ_B is the Bohr magneton. The total field is the sum of applied and hyperfine fields: $\mathbf{B}_{tot} = \mathbf{B} + \mathbf{B_n}$, where the hyperfine field is

$$\mathbf{B_n} = b_n \frac{(\mathbf{B} + b_e \mathbf{S}) \cdot \mathbf{S}}{(\mathbf{B} + b_e \mathbf{S})^2 + \xi B_L^2} (\mathbf{B} + b_e \mathbf{S}) \tag{3.32}$$

as discussed in Sec. 2.1.3. The parameters used were those for $T = 80$ K determined in Chapters 1 and 2 for heterostructure Q62. For this calculation P_0 is along the $\pm x$ directions, and B is along the z direction (if P_0 is along the y direction instead, one need only switch x and y components in Fig. 3.18).

Although we have demonstrated in Sec. 3.4.5 that the SDH signal is directly dependent on B_n, Fig. 3.18 shows clearly that the form of the measured even SDH signal is not reproduced by any components of $\mathbf{S}$ or $\mathbf{B_n}$. This suggests that the SDH signal is not due to the nuclear spin polarization alone.

The phenomenological expression describing charge transport due to SO coupling in Eq. 3.6 can be written generally as $\boldsymbol{j}_{SH} \propto \boldsymbol{k} \times \boldsymbol{S}$ where $\boldsymbol{k}$ is the wavevector describing the direction of spin polarization flow (either through drift or diffusion) and $\boldsymbol{S} \equiv \boldsymbol{P}/2$. Fig. 3.19 shows the resultant odd(a) and even(b) SDH

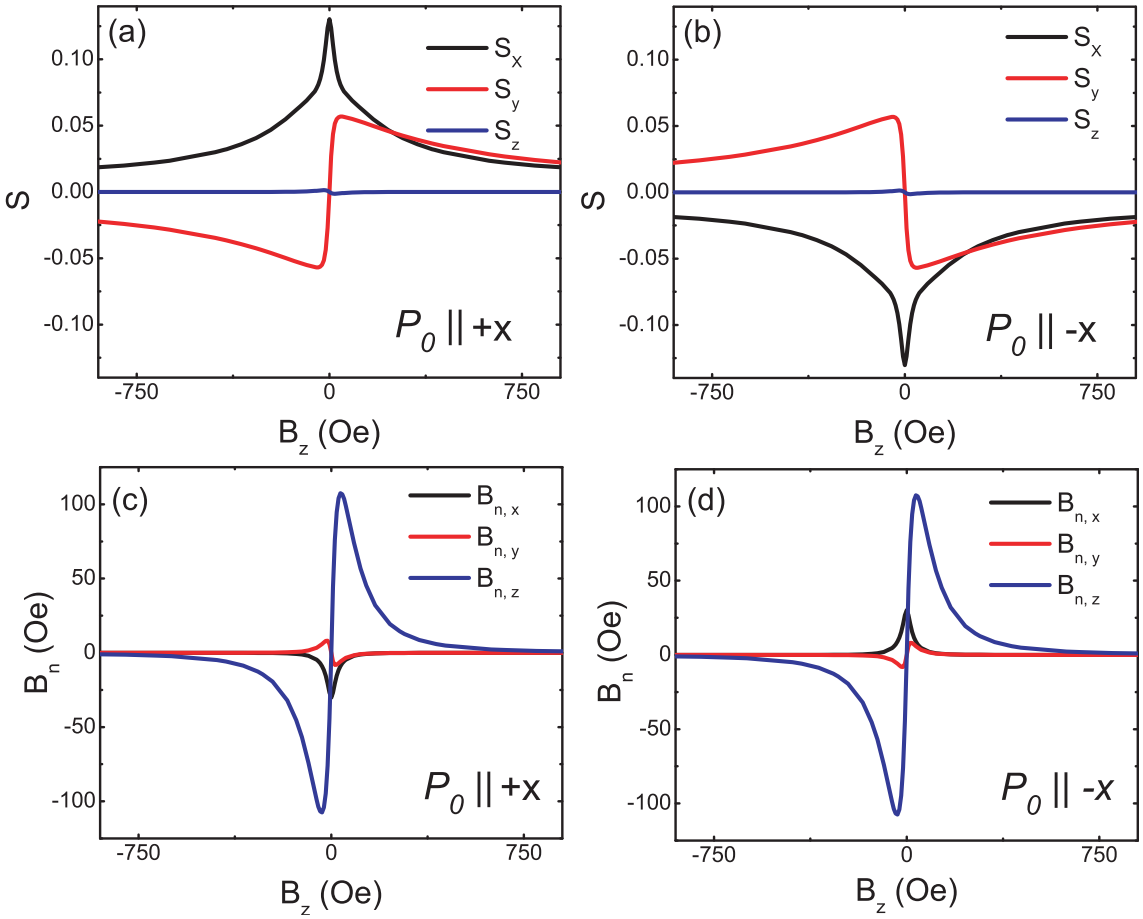

Figure 3.18: Calculation of $\mathbf{S}$ and $\boldsymbol{B}_n$ as a function of B_z for spins injected in the x direction. All three components of $\mathbf{S}$ and $\boldsymbol{B}_n$ are shown for $M_i \parallel +x$ (a), (c) and $M_i \parallel -x$ (b), (d). The parameters used were those for $T = 80\ K$. $b_n = -28$ Oe, $b_e = -35$ Oe, $\sqrt{\xi} B_l = 43$ Oe, $\tau_s = 3.1$ ns, and $D = 10.8\ \mu\text{m}^2/\text{ns}$.

Hanle curves calculated by rewriting $\boldsymbol{j}_{SH} \propto \boldsymbol{k} \times (\boldsymbol{S} \times \boldsymbol{I})$ for the measurement configuration shown in Figs. 3.6(a) and 3.11(a). $\mathbf{I} = \mathbf{B}_n/b_n$ is the mean nuclear spin polarization. Comparing Figs. 3.19(a) and (b) to the measured SDH signals in Figs 3.7 and 3.12, we see that the new phenomenological form reproduces the observed Hanle curves of both the odd and even SDH signals.

3.4.8 Microscopics

Previous theoretical explanations for the SHE are based on the spin-orbit interaction. [96, 97, 100, 110, 112, 113, 120] The SO interaction couples the electron orbital and spin angular momenta. The experimental results discussed in this chapter suggest that the nuclear spin polarization is coupled to the electron angular momentum as well. Relativistically, an electron and nuclear spin are coupled by three terms, one of which is the Fermi contact interaction, which is responsible for DNP discussed in Ch. 2. This interaction is non-zero only for s-states, which have orbital angular momentum $l = 0$. The other two terms are the anisotropic dipole-dipole interaction and orbital hyperfine interaction described by[121]

$$H_{dd} = \frac{\mu_0}{4\pi} g_0 \mu_B \gamma_n \frac{3(\mathbf{n}\cdot\mathbf{S})(\mathbf{n}\cdot\mathbf{I}) - \mathbf{S}\cdot\mathbf{I}}{R^3(1+d/R)}, \tag{3.33}$$

$$H_{oh} = \frac{\mu_0}{4\pi} g_0 \mu_B \gamma_n \frac{\mathbf{L}\cdot\mathbf{I}}{R^3(1+d/R)}, \tag{3.34}$$

respectively. γ_n is the nuclear gyromagnetic ratio, $\mathbf{R}$ is the position of the electron relative to the nucleus, $d \approx Z \times 1.5 \times 10^{15}$ m is the length of the nuclear dimension, Z is the charge of the nucleus, and $\mathbf{n}$ is the unit vector in the direction of $\mathbf{R}$. $\mathbf{L} = \mathbf{R} \times \mathbf{p}$, where $\mathbf{p}$ is the electron linear momentum, is the orbital angular momentum. $\mathbf{S}$ and $\mathbf{I}$ are the electron and nuclear electron spins respectively.

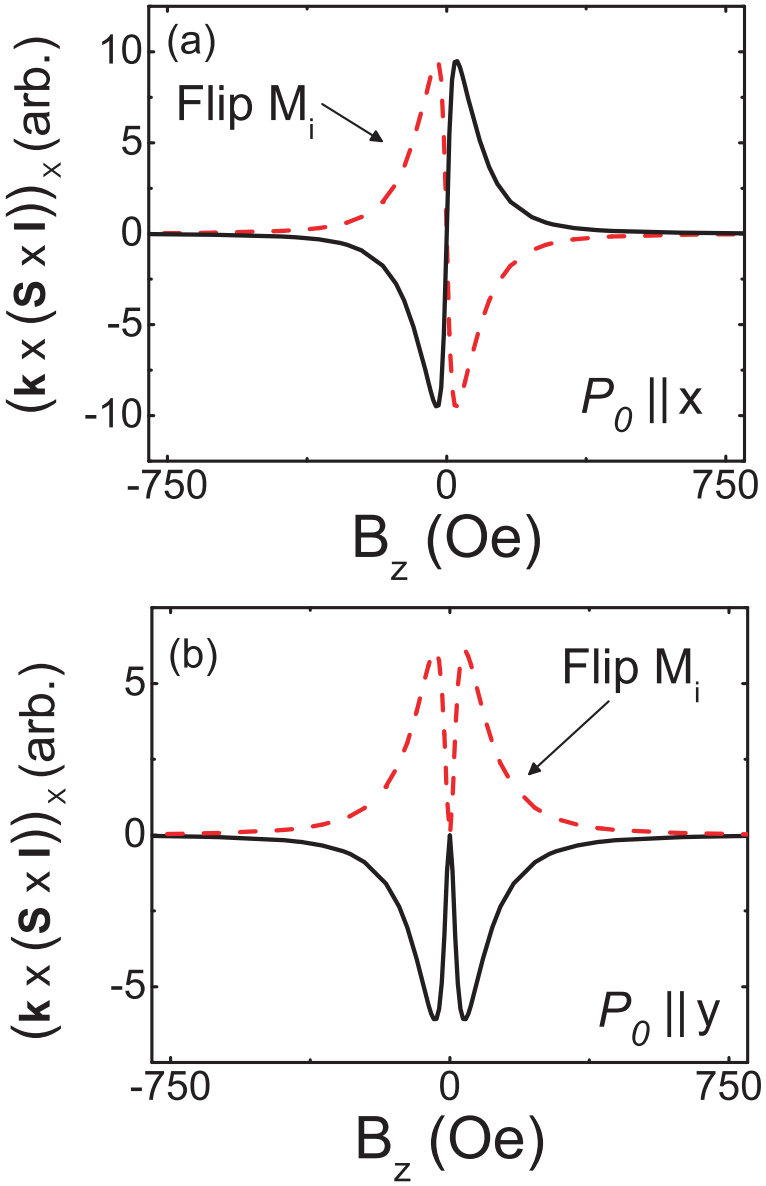

Figure 3.19: Calculated x component of the proposed phenomenological form of the SDH signal as described in the text for $P_0||x$ (a) and $P_0||y$ (b).

The strength of the anisotropic or orbital hyperfine couplings in bulk GaAs were estimated by Fischer *et al.*[122] The hydrogenic $4s$ and $4p$ electrons are given by $\Psi_{400} = X_{40}(R)Y_0^0(\theta,\phi)$ and $\Psi_{41\pm1} = X_{41}(R)Y_1^{\pm1}(\theta,\phi)$. The effective Ga and As screened nuclear charges Z_{eff} were calculated in Ref. [123]. Using the hydrogenic eigenfunctions, Fischer determined that the hyperfine coupling from H_{dd} and H_{ho} from $4p$ electrons is about 10% of the Fermi contact Hamiltonian coupling to $4s$ electrons.[122] As a result, the conduction electron angular orbital momentum should be considered in hyperfine interactions in GaAs. From the s electron hyperfine coupling strength from Refs. [81] and [122], we estimate the p electron hyperfine coupling to be ~ 10 μeV. An estimate of the electron spin-orbit coupling strength in GaAs with Eq. 3.16 and assuming a Coulomb impurity potential and $Z_{eff} = 1/\epsilon = 1/12$ [113] yields a coupling strength of ~ 1 μeV, which is about an order of magnitude smaller than the hyperfine orbital coupling estimated above. The measured SDH signal in our devices is approximately 1 to 2 orders of magnitude larger than that expected for SO coupling and impurity scattering. A detailed calculation is required to determine if the orbital-hyperfine interaction is responsible for the observed SDH signal.

3.5 Conclusion

In this chapter we have introduced the phenomenological charge and spin transport equations which encompass various effects due to the SO interaction. The SHE measured in n-GaAs is attributed to extrinsic skew scattering/side jump mechanisms due to the agreement between measured and calculated spin Hall conductivity. We observe a spin-dependent Hall voltage measured across the

spin-polarized region of a GaAs channel. Application of a transverse magnetic field results in a modulation of the Hall voltage consistent with spin de-phasing. This signal changes sign when the magnetization of the Fe contact is switched, indicating sensitivity to electron spin direction. The observed spin-dependent Hall signal is approximately two orders of magnitude larger than that expected from previous measurements of the spin Hall effect in n-GaAs, which was attributed to spin-orbit coupling and impurity scattering. This suggests that a different mechanism is active in our system. We demonstrate full suppression of the spin-dependent Hall signal by eliminating nuclear polarization through a field cycling procedure. Additionally, while the electron spin accumulation, detected by a spin sensitive Fe contact, persists up to 200 K, the spin-dependent Hall signal is not observed above 120 K, in coincidence with the disappearance of the nuclear spin polarization due to delocalization of donor electrons. We conclude that the observed spin-dependent Hall signal is coupled to the nuclear spin polarization. This is the first observation of a hyperfine induced spin Hall effect.

Bibliography

[1] M. N. Baibich, J. M. Broto, A. Fert, F. Nguyen, F. Petroff, P. Etienne, G. Creuzet, A. Friederich, and J. Chazelas, Phys. Rev. Lett. **61**, 2472 (1988).

[2] J. S. Moodera, L. R. Kinder, T. M. Wong, R. Meservey, Phys. Rev. Lett. **74** 3273 (1995).

[3] S. Datta and B. Das, Appl. Phys. Lett. **56**, 665 (1990).

[4] G. Lampel, Phys. Rev. Lett. **20**, 491 (1968).

[5] R. R. Parsons, Phys. Rev. Lett. **23**, 1132 (1969).

[6] *Optical Orientation*, ed. by F. Meier and B. P. Zakharchenya (North Holland, Amsterdam, 1984).

[7] J. M. Kikkawa and D. D. Awschalom, Phys. Rev. Lett. **80**, 4313 (1998).

[8] D. Awschalom and J. Kikkawa, Nature (London) **397**, 139 (1999).

[9] J. M. Kikkawa and D. D. Awschalom, Science **287**, 473 (2000).

[10] Y. K. Kato, R. C. Myers, A. C. Gossard, D. D. Awschalom, Science **306**, 1910 (2004).

[11] A. G. Aronov, Pis'ma Z. Eksp. Theor. Fiz. **24**, 37 (1976); Sov. Phys. JETP Lett. **24**, 32 (1976).

[12] R. H. Silsbee, Bul. Mag. Res. **2**, 284 (1980).

[13] M. Johnson and R. H. Silsbee, Phys. Rev. Lett. **55**, 1790 (1985).

[14] M. I. Dyakonov, V. I. Perel, in *Optical Orientation*, ed. by F. Meier and B.P. Zakharchenya (North Holland, Amsterdam, 1984).

[15] F. J. Jedema, A. T. Filip, and B. J. van Wees, Nature (London) **410**, 345 (2001).

[16] R. Godfrey and M. Johnson, Phys. Rev. Lett. **96**, 136601 (2006)

[17] S. O. Valenzuela and M. Tinkham, Appl. Phys. Lett. **85** 24 (2004).

[18] F. J. Jedema, H. B. Heersche, A. T. Philip, J. J. A. Baselmans and B. J. van Wees, Nature (London) **416** 713 (2002)

[19] T. Kimura and Y. Otani, Phys. Rev. Lett. **99**, 196604 (2007).

[20] Y. Ji, A. Hoffmann, J. E. Pearson, and S. D. Bader, Appl. Phys. Lett. **88**, 052509 (2006).

[21] F. Casanova, A. Sharoni, M. Erekhinsky, and I. K. Schuller, Phys. Rev. B **79**, 184415 (2009).

[22] H. C. Koo, J. H. Kwon, J. Eom, J. Chang, S. H. Han, and M. Johnson, Science **325**, 1515 (2009).

[23] S. Bandyopadhyay (2010) arXiv 0911.0210v1.

[24] S. P. Dash, S. Sharma, R. S. Patel, M. P. de Jong, and R. Jansen, Nature **462**, 26 (2009).

[25] Y. A. Bychkov and E. I. Rashba, JETP Lett. 39, 78 (1984) [Pisma Zh. Eksp. Teor. Fiz. **39**, 66 (1984)].

[26] P. R. Hammar, B. R. Bennett, M. J. Yang, and Mark Johnson, Phys. Rev. Lett. **83**, 203 (1999).

[27] F. G. Monzon, H. X. Tang, and M. L. Roukes, Comment, Phys. Rev. Lett. **84**, 5022 (2000); B. J. vanWees, Comment, Phys. Rev. Lett. **84**, 5023 (2000);P. R. Hammar, B. R. Bennett, M. J. Yang, and Mark Johnson, Comment, Phys. Rev. Lett. **84**, 5024 (2000).

[28] F. G. Monzon and M. L. Roukes, J. Magn. Magn. Mater. 198, 628 (1999); F. G. Monzon, D. S. Patterson, and M. L. Roukes, J. Magn. Magn. Mater. 195, 19 (1999).

[29] A. T. Hanbicki, B. T. Jonker, G. Itskos, G. Kioseoglou, and A. Petrou, Appl. Phys. Lett. **80**, 1240 (2002).

[30] O. M. J. van't Erve, G. Kioseoglou, A. T. Hanbicki, C. H. Li, B. T. Jonker, R. Mallory, M. Yasar, and A. Petrou, Appl. Phys. Lett. **84** 4334 (2004)

[31] V. F. Motsnyi, P. Van Dorpe, W. Van Roy, E. Goovaerts, V. I. Safarov, G. Borghs, and J. De Boeck, Phys. Rev. B **68**, 245319 (2003).

[32] J. Strand, B. D. Schultz, A. F. Isakovic, C. J. Palmstrøm, and P. A. Crowell, Phys. Rev. Lett. **91**, 036602 (2003).

[33] J. Strand, A. F. Isakovic,X. Lou, B. D. Schultz, C. J. Palmstrøm, and P. A. Crowell, Appl. Phys. Lett. **83**, 3335 (2003).

[34] J. Strand, X. Lou, C. Adelmann, B. D. Schultz, A. F. Isakovic, C. J. Palmstrøm, and P. A. Crowell, Phys. Rev. B **72**, 155308 (2005).

[35] P. C. van Son, H. van Kempen, and P. Wyder, Phys. Rev. Lett. **58**, 2271 (1987).

[36] T. Valet and A. Fert, Phys. Rev. B **48**, 7099 (1993).

[37] S. A. Crooker, M. Furis, X. Lou, C. Adelmann, D. L. Smith, C. J. Palmstrøm, and P. A. Crowell, Science **309**, 2191 (2005).

[38] X. Lou, C. Adelmann, M. Furis, S. A. Crooker, C. J. Palmstrøm, and P. A. Crowell, Phys. Rev. Lett. **96**, 176603 (2006).

[39] X. Lou, C. Adelmann, S. A. Crooker, E .S. Garlid, J. Zhang, K. S. M. Reddy, S. D. Flexner, C. J. Palmstrøm, and P.A. Crowell, Nat. Phys. **3**, 197 (2007).

[40] I. Appelbaum, B. Huang, and D. Monsma, Nature (London) **447**, 295 (2007).

[41] M. Tran, H. Jaffrès, C. Deranlot, J. M. Goerge, A. Fert, A. Miard, and A. Lemaître, Phys. Rev Lett. **102**, 036601 (2009).

[42] C. Awo-Affouda, O. M. J. van 't Erve, G. Kioseoglou, A. T. Hanbicki, M. Holub, C. H. Li, and B. T. Jonker, Appl. Phys. Lett. **94**, 102511 (2009)

[43] M. Ciorga, A. Einwanger, U. Wurstbauer, D. Schuh, W. Wegscheider, and D. Weiss, Phys. Rev. B **79**, 165321 (2009).

[44] G. Salis, A. Fuhrer, and S. F. Alvarado, Phys. Rev. B **80**, 115332(R) (2009).

[45] H. Sanada, S. Matsuzaka, K. Morita, C.Y. Hu, Y. Ohno, and H.Ohno, Phys. Rev. B **68**, 241303(R) (2003).

[89] N. F. Mott, Proc. Toy. Sov. **153**, 699 (1936).

[47] N. F. Mott, Adv. Phys. **13**, 325 (1964).

[48] I. A. Campbell and A. Fert, J. Phys. F **6**, 849 (1976).

[49] Z. G. Yu and M. E. Flatté, Phys. Rev. B **66**, 235302 (2002).

[50] M. Furis, D. L. Smith, S. A. Crooker, J. L. Reno, Appl. Phys. Lett. **89**, 102102 (2006).

[51] D. J. Oliver, Phys. Rev. **127**, 1045 (1962).

[63] M. Johnson and R. H. Silsbee, Phys. Rev. B **35**, 4959 (1987).

[53] G. Schmidt, D. Ferrand, L. W. Molenkamp, A. T. Filip, and B. J. van Wees, Phys. Rev. B **62**, R4790 (2000).

[54] I. E. Rashba, Phys. Rev B, **62**, R16267 (2000).

[55] D. L. Smith and R. N. Silver, Phys. Rev. B **64**, 045323 (2001).

[56] A. Fert and H. Jaffrés, Phys. Rev. B **64**, 188420 (2002).

[57] W. F. Brinkman, R. C. Dynes, and J. M. Rowell, J. Appl. Phys. **41**, 1915 (1970).

[58] W. A. Harrison, Phys. Rev. **123**, 85 (1961).

[59] R. I. Dzhioev, K. V. Kavokin, V. K. Korenev, M. V Lazarev, B. Ya. Meltser, M. N. Stepanova, B. P. Zakharchenya, D. Gammon, and D. S. Karzer, Phys. Rev. B **66**, 245204 (2002).

[60] W. H. Press, S. A. Teukolsky, W. T. Vetterling, and B. P. Flannery *Numerical Reciepes in C, The Art of Scientific Computing* 2^{nd} ed.,(Cambridge University Press, 1992).

[61] R. J. Soulen Jr. *et. al.*, *Science* **282**, 85-88 (1998).

[62] C. Adelmann, X. Lou, J. Strand, C. J. Palmstrom, and P. A. Crowell, Phys. Rev. B **71**,121301 (2005).

[63] M. Johnson and R. H. Silsbee, Phys. Rev. B **35**, 4959 (1987).

[64] V. V. Osipov and A. M. Bratkovsky, Phys. Rev. B **72**, 115322 (2002)

[65] A. G. Petukhov, J. Niggemann, V. N. Smelyanskiy, and V. V. Osipov, J. Phys.:Condens. Matter bf 19, 315205 (2007).

[99] D. L. Smith and R. N. Silver, Phys. Rev. B **64**, 045323 (2001).

[67] S. A. Crooker, E. S. Garlid, A. N. Chantis, D. L. Smith, K. S. M. Reddy, Q. O. Hu, T. Kondo, C. J. Palmstrøm, and P.A. Crowell, Phys. Rev. B **80**, 041305(R) (2009).

[68] J. Crank and P. Nicolson, Adances in Comp. Mathematics **6**, 207 (1996).

[69] H. Dery and L. J. Sham, Phys. Rev. Lett., **98**, 046602 (2007).

[70] D. L. Smith and P. P. Ruden, Phys. Rev. B **78**, 125202, (2008).

[71] A. N. Chantis, K. D. Belashchenko, D. L. Smith, E. Y. Tsymbal, M. van Schilfgaarde, and R. C. Albers, Phys. Rev. Lett. **99**, 196603 (2007).

[72] A. N. Chantis, D. L. Smith, Phys. Rev. B **78**, 235317 (2008).

[73] G. E. Pikus and A. N. Titkov, in *Optical Orientation*, Edited by F. Meier and B. P. Zakharchenya (North-Holland, Amsterdam), p. 109.

[74] G. Dresselhaus, Phys. Rev. **100**, 580 (1955).

[75] M. I. D'yakonov and V. I. Perel', Sov. Phys. Solid State **13**, 3023 (1971).

[76] V. A. Marushchak, M. N. Stepanova, and A. N. Titkov, Sov. Phys. Solid State **25**, 2035 (1983).

[77] A. Abragam, *Principles of Nuclear Magnetism* (Cambridge Univ. Press, London, 1961).

[78] A. Overhauser, Phys. Rev., **92**, 411 (1953).

[79] M. I. D'yakonov and V. I. Perel', Zh. Eksp. Teor. Fiz. **65**, 362 (1973); Sov. Phys. JETP **38**, 177 (1974).

[80] T. R. Carver and C. P. Slichter , Phys. Rev. **92**, 212 (1953).

[81] D. Paget, G. Lampel, B. Sapoval, and V. I. Safarov, Phys. Rev. B **15**, 5780 (1977).

[82] D. Paget, Phys. Rev. B **25**, 4444 (1982).

[83] N. Bloembergen, Physica **15**, 386 (1949).

[84] P. G. DeGennes, J. Phys. Chem. Solids **7**, 345 (1958).

[85] I.J. Lowe and D. Tse, Phys. Rev. **166**, 279 (1968).

[86] J.Strand, Ph.D Thesis, School of Physics and Astronomy, University of Minnesota (2004).

[87] B. P. Zakharchenya, V. K. Kalevich, V. D. Kul'kov, and V. G. Fleĭsher, Fiz. Tverd. Tela (Leningrad) **23**, 1387-1394 (1981).

[88] D. Paget, Phys. Rev. B **23** 7 (1981).

[89] N. E. Mott and H. S. W. Massey, *The Theory of Atomic Collisions* (Clarendon, Oxford, 1965), Chap. 15.

[90] C. Schwartz, Phys. Rev. **124**, 1468 (1961).

[91] D. Gammon, Al. L. Efros, T. A. Kennedy, M. Rosen, D. S. Katzer, D. Park, and S. W. Brown, Phys. Rev. Lett. **86**, 5176 (2001).

[92] V. G. Fleisher and I. A. Merkulov, in *Optical Orientation*, ed. by F. Meier and B.P. Zakharchenya (North Holland, Amsterdam, 1984).

[93] R. L. Mieher, Phys. Rev. **125**, 1537 (1962).

[94] C. Hermann and G. Lampel, Phys. Rev. Lett. **27**, 373 (1971)

[95] V. L. Berkovitz, A. I. Ekimov and V. I. Safarov, Zh. Eksp. Teor. Fiz. **65**, 346 (1973); Sov. Phys. JETP **38**, 159 (1974).

[96] M. I. D'yakonov and V. I. Perel', Pis',a Z. Eksp. Teor. Fiz. **13**, 657 (1971); JETP Lett. **13**, 467 (1971).

[97] M. I. D'yakonov nad V. I. Perel', Phys. Lett. A **35**, 459 (1971).

[98] E. H. Hall, Philos. Mag. **10**, 301 (1880).

[99] A. W. Smith, Phys. Rev. **30**, 1 (1910).

[100] N. Nagaosa, J. Sinova, S. Onoda, A. H. MacDonald, and N. P. Ong, arXiv:0904.4154v1 (2009).

[101] J. N. Chazelviel, and I. Solomon, Phys. Rev. Lett. bf 29, 1676 (1972).

[102] A. A. Bakun, B. P. Zakharchenya, A. A. Rogachev, M. N. Tkachuk, V. G. Fleisher, Z. Eksp. Teor. Fiz. Pis'ma **44**, 47 (1986); Sov. Phys. JETP lett. **44**, 59 (1986).

[103] M. N. Tkachuk, B. P. Zakharchenya, V. G. Fleĭsher, Piz'ma Zh. Eksp. Teor. Fiz. **44**, 1 (1986); JETP Lett. **44**, 1 (1986).

[104] S. O. Valenzuela and M. Tinkham, Nature **42**, 176 (2006).

[105] T. Kimura, Y. Otani, T. Sato, S. Takahashi, and S. Maekawa, Phys. Rev. Lett. **98**, 156602 (2007).

[106] T. Kimura, Y. Otani, and L. Villa, J. of Appl. Phys. **103**, 07F310 (2008).

[107] T. Seki, Y. Hasegawa, S. Mitani, S. takahashi, H. Imamura, S. Maekawa, J. Nitta, and K. Takanashi, Nature Materials bf 7, 2098, (2008).

[108] S. Zhang, J. of Appl. Phys., **89** 11 (2001).

[109] J. E. Hirsch, Phys. Rev. Lett. **83**, 1834 (1999).

[110] L. Berger, Phys. Rev. B **2**, 4559 (1970).

[111] L. Berger, Phys. Rev. B **6**, 1862 (1972).

[112] R. Karplus and J. M. Luttinger, Phys. Rev. **95**, 1154 (1954).

[113] H. Engel, B. I. Halperin, and E. I. Rashba, Phys. Rev. Lett. **95**, 166605 (2005).

[114] J. W. Motz, H. Olsen, and H. W. Koch, Rev. Mod. Phys. **36**, 881 (1964); see Sec. VI and Eqs. (1A-107) and (1A-403).

[115] V. N. Abakumov, I. N. Yassievich, A. Eksp. Teor. Fiz. **61**, 2271 (1971); Sov Phys. JETP **34**, 1375 (1971).

[116] P. Nozie‘res and C. Lewiner, J. Phys. (Paris) **34**, 901 (1973).

[117] Y. Yafet, in *Solid State Physics*, edited by F. Seitz and D Turnbull (Academic, New York, 1963), Vol. 14, p. 1.

[118] E. M. Chudnovsky, Phys. Rev. Lett. **99**, 206601 (2007).

[119] R. Winkler, *Spin-Orbit Coupling Effects in Two-Dimensional Electron and Hole System*, Springer, Berlin (2000).

[120] B. A. Bernevig and S.C. Zhang, arxiv:cond-mat\0412550v1 (2004).

[121] A. M. Stoneham, *Theory of Defects in Solids* (Oxford University Press, New York, 1972), Chap. 3.

[122] J. Fischer, W. A. Coish, D. V. Bulaev, and D. Loss, Phys. Rev. B **78**. 155329 (2008).

[123] E. Clementi and D. L. Raimondi, J. Chem. Phys. **38**, 2686 (1963).